Forschungsbericht 2025-10

Examination of Thermomechanical Fatigue in Panels Representing Rocket Engine Combustion Chamber Geometries

Pascal H. Kringe

Deutsches Zentrum für Luft- und Raumfahrt
Institut für Raumfahrtantriebe
Lampoldshausen

Deutsches Zentrum
DLR für Luft- und Raumfahrt

Forschungsbericht 2025-10

Examination of Thermomechanical Fatigue in Panels Representing Rocket Engine Combustion Chamber Geometries

Pascal H. Kringe

Deutsches Zentrum für Luft- und Raumfahrt
Institut für Raumfahrtantriebe
Lampoldshausen

163 Seiten
54 Bilder
22 Tabellen
163 Literaturstellen

Deutsches Zentrum
DLR für Luft- und Raumfahrt

Herausgeber:

Deutsches Zentrum
für Luft- und Raumfahrt e. V.
Wissenschaftliche Information
Linder Höhe
D-51147 Köln

ISSN 1434-8454
ISRN DLR-FB-2025-10
Erscheinungsjahr 2025
DOI: 10.57676/js82-f364

Thermomechanische Ermüdung, niedrig-zyklische Ermüdung, Raketentriebwerk, Brennkammer, Ermüdungsschädigung

Pascal H. KRINGE
DLR, Institut für Raumfahrtantriebe, Lampoldshausen

Untersuchung der Thermomechanischen Ermüdung in Platten mit Raketenbrennkammergeometrien
RWTH Aachen University

Die vorliegende Arbeit dokumentiert die Ergebnisse einer Ermüdungslebensdaueruntersuchung unter Verwendung von Cu-HCP und CuCrZr als Materialien der inneren Wand in regenerativ gekühlten kryogenen Brennkammern von Raketenmotoren. Der experimentelle Teil der Studie verwendet so genannte Thermomechanische Ermüdungs-Panels (TMF Panel). Ein TMF Panel repräsentiert einen kleinen Ausschnitt einer regenerativ gekühlten Raketenbrennkammer mit typischerweise sieben Kühlkanälen. Diese Panels werden zyklisch bis zum Versagen auf dem TMF Prüfstand am DLR Institut für Raumfahrtantriebe getestet. Als Kühlmittel dient überkritischer Stickstoff, der Wasserstoff oder Methan ersetzt. Der TMF Prüfstand verfügt über einen Hochleistungsdiodenlaser, der zyklisch auf die Oberfläche der TMF-Platte strahlt und mehrere Lastzyklen nachahmt, wie sie insbesondere bei wiederverwendbaren Raketenmotoren auftreten. Diese Anordnung isoliert das reine mechanische Verhalten des Materials von Einflüssen durch Verbrennung oder Chemikalien. Darüber hinaus ermöglicht die genaue Bestimmung von Wärmestromdichte, Oberflächentemperatur und Massenstrom präzise Eingangsdaten für numerische Simulationen und deren Validierung. Insgesamt wurden vier Testkampagnen durchgeführt. Ein Wärmeübertragungstest (HTT) Panel untersucht die Beziehung zwischen Oberflächentemperatur, Massenstrom und Wärmestromdichte für Cu-HCP. Zwei TMF Panel Testkampagnen mit Panels aus Cu-HCP untersuchten den Einfluss der Oberflächentemperatur auf die Lebensdauer bei T_s = 800 K und T_s = 900 K. Die höhere Temperatur führt zu einer Abnahme der Lebensdauer um 12 %. Die verbleibende Testkampagne wurde mit einem CuCrZr TMF Panel mit T_s = 800 K durchgeführt. Dieses Panel zeigt eine Lebensdauer von 427 % im Vergleich zu den gleichen Bedingungen des Cu-HCP TMF Panels. Alle TMF Panel Tests wurden mit einer Wandwärmestromdichte von q_w = 24.25 MW/m2 durchgeführt.

Mit den experimentellen Daten des HTT Panels wurde eine gekoppelte Analyse in ANSYS validiert, wobei die Kopplung eine CFX-Komponente und eine stationäre thermische Komponente in Mechanical verwendet hat. Diese verifizierte Analyse lieferte die Temperaturverteilung innerhalb des Panels, die als entscheidende Eingabe für die folgende Finite-Elemente-Analyse in ANSYS Mechanical diente, um die Spannungs- und Dehnungsentwicklung der verbleibenden drei TMF Panels numerisch zu bestimmen. Drei nichtlineare Materialmodelle wurden verglichen. Zwei Materialmodelle wurden über benutzerprogrammierbare Funktionen (UPF) implementiert, eines für jedes Material. Zusätzlich wurden die TMF Panels unter Verwendung der bereits im ANSYS Softwarepaket eingebetteten Modelle simuliert. Hierzu wurden das kinematische Verfestigungsmodell nach Chaboche, das isotrope Ver- und Entfestigungsmodell nach Voce, das Nortonsche Kriechgesetz und das Modell für Dehnratenabhängigkeit nach Peirce verwendet. Die mechanischen Materialparameter für die bereits eingebetteten Modelle wurden durch eine umfangreiche Testreihe bestimmt, die komplexe zyklische Ermüdungs- (CLCF) und Zugversuche an uniaxialen Proben umfasste und einen Temperaturbereich von T = 77 K bis T = 1000 K abdeckte. Die Materialdaten für die UPFs wurden für Cu-HCP im Rahmen eines Projektes bestimmt bzw. aus der Literatur entnommen. Zur Abschätzung der Ermüdungslebensdauer wurde in MATLAB ein Post-Processing-Tool entwickelt und verwendet, das ein duktiles Schädigungsmodell nach Bonora und ein sprödes Schädigungsmodell nach Lemaitre kombiniert. Dabei wird die nutzbare Lebensdauer eingeführt, welche die Anzahl der Zyklen eines TMF Panels charakterisiert, infolge derer hohe Verformungen und Verformungsraten aufgrund der Bildung von Makrorissen eingeleitet wurden. Dieser Effekt kann in den experimentellen Daten beobachtet werden und wird in den numerischen Ergebnissen durch das Erreichen der kritischen Schädigung am innersten Punkt der wärmebelasteten Wand definiert. Die experimentell und die numerisch ermittelte Anzahl der Zyklen stimmen sehr gut überein.

thermomechanical fatigue, low cycle fatigue, rocket engine, combustion chamber, fatigue damage

(Published in English)

Pascal H. KRINGE
German Aerospace Center (DLR), Institute of Space Propulsion, Lampoldshausen

Examination of Thermomechanical Fatigue in Panels Representing Rocket Engine Combustion Chamber Geometries

RWTH Aachen University

The present thesis details the findings of a fatigue life investigation involving the use of Cu-HCP and CuCrZr as the inner liner material in regeneratively cooled cryogenic rocket engine combustion chambers. The experimental part of the study employs Thermomechanical Fatigue (TMF) panels. A TMF panel represents a small portion of a regeneratively cooled rocket combustion chamber, typically seven cooling channels. These panels undergo cyclic testing until failure at the TMF test bench located at the DLR Institute of Space Propulsion. Supercritical nitrogen serves as the coolant, replacing hydrogen or methane. The TMF test bench features a high-power diode laser that cyclically emits onto the TMF panel surface, mimicking multiple load cycles, as particularly present in reusable rocket engines. This setup isolates the pure mechanical behavior of the material from combustion or chemical influences. Additionally, the accurate determination of heat flux, surface temperature, and mass flow rate provide precise input data for numerical simulation and validation. Overall, four test campaigns were conducted. A heat transfer test (HTT) panel investigates the relation of surface temperature, mass flow rate and heat flux for Cu-HCP. Two TMF panel test campaigns with panels made from Cu-HCP studied the influence of the surface temperature at T_s = 800 K and T_s = 900 K. The higher temperature causes a decrease of 12 % of the fatigue life. The remaining test campaign was dedicated to a CuCrZr TMF panel with T_s = 800 K. This panel yields a fatigue life of 427 % when compared to the same conditions of the Cu-HCP TMF panel. All TMF panel tests were conducted with a wall heat flux of q_w = 24.25 MW/m2.

With the experimental data of the HTT panel a coupled analysis in ANSYS using a CFX component and a steady state thermal component in Mechanical was validated. This verified analysis provided the temperature distribution that served as a key input for the following finite elements analysis in ANSYS Mechanical to numerically determine the stress and strain development of the remaining three TMF panels. Three nonlinear material models were compared. Two material models were implemented by user programmable features (UPF), one for each material. Additionally, the TMF panels were simulated using the models already embedded in the ANSYS software package. Therefore the kinematic hardening model developed by Chaboche, the isotropic hardening and softening model following Voce, Norton's creep law, and the strain rate dependency model according to Peirce were utilized. The mechanical material parameters for the already embedded models are determined through an extensive test series, encompassing complex low cycle fatigue (CLCF) and tensile tests on uniaxial specimens, covering a temperature range from cryogenic conditions at T = 77 K to T = 1000 K. The material data for the UPFs were determined in the framework of a project for Cu-HCP and taken from literature, respectively. To estimate the fatigue life, a post-processing tool is developed and employed in MATLAB combining a ductile damage model according to Bonora and a brittle damage model developed by Lemaitre. The useful fatigue is introduced. It characterizes the number of cycles of a TMF panel after that high deformation and deformation rates are initiated due to the formation of macro cracks. This effect can be observed in the experimental data and is defined in the numerical results by the critical damage being reached at the innermost point of the heat loaded wall. Both, experimentally and numerically obtained number of cycles match very well.

Examination of Thermomechanical Fatigue in Panels Representing Rocket Engine Combustion Chamber Geometries

Von der Fakultät für Bauingenieurwesen der Rheinisch-Westfälischen Technischen Hochschule Aachen zur Erlangung des akademischen Grades eines Doktors der Ingenieurwissenschaften genehmigte Dissertation

vorgelegt von

Pascal Heinrich Kringe

Berichter: Univ.-Prof. Dr.-Ing. Markus Feldmann
Univ.-Prof. Dr.-Ing. Stefanie Reese
Univ.-Prof. Dr. rer. nat. Michael Oschwald

Tag der mündlichen Prüfung: 25. Oktober 2024

Diese Dissertation ist auf den Internetseiten der Universitätsbibliothek online verfügbar.

"Any *useful* idea about the futures should appear to be *ridiculous*."

Second Law of the Futures, Jim Dator

Acknowledgments

This thesis was prepared during my time as a research assistant at the DLR Institute of Space Propulsion in Lampoldshausen.

First and foremost, I would like to express my gratitude to Univ.-Prof. Dr.-Ing. Stefanie Reese for her support, guidance, and advice, especially during the final stages of my research. I also want to thank Prof. Reese and the team at the Institute of Applied Mechanics at RWTH Aachen University for the opportunity to work on-site, their warm welcome, insights into theoretical approaches to material modeling, and fruitful discussions.

I am equally grateful to Univ.-Prof. Dr. rer. nat. Michael Oschwald for giving me the opportunity to conduct this thesis, for his continuous support throughout countless meetings, and for his constructive advice.

Furthermore, I would like to thank Univ.-Prof. Dr.-Ing. Markus Feldmann for chairing the defense committee.

My sincere thanks also go to Dr. Jörg Riccius for leading the Structures Group, his wealth of ideas for improvement, and his ongoing efforts in fighting measurement uncertainty. Special thanks go to Sebastian Kahl, technician at the M51 test bench, for bending pipes, installing sensors, installing even more sensors, keeping the laser running, and always maintaining a good mood! I also appreciate Evgeny Zametaev for all his simulations and expertise in this field. Additionally, I am grateful to Dr. Justin Hardi for always lending an ear and paving the way, as well as the team at the Department of Rocket Propulsion Technology for their support. Furthermore, I would like to thank Chris Bürger for his detailed simulations of the heat transfer test panel during his Master's Thesis project, which provided valuable results for this thesis.

My deep gratitude also goes to Andreas Märklen and Alfred Rohatschek, whose passion for precise design and manufacturing is truly inspiring.

Moreover, I would like to thank all participants of the two-phase-flow experiments. The scientific discussions not only helped solve many problems but also encouraged me and kept me motivated.

I am also particularly grateful to Jan van Schyndel, Kai Dresia, Maxim Kurilov, Sebastian Klein, Sachin Kanarath and Terence Profita for taking on the fatiguing task of proofreading.

Finally, I wish to express my heartfelt thanks to my parents and my brother

for pushing me forward and supporting me in every situation. Above all, I am deeply grateful to my partner Barbara for enduring months of writing, days of procrastination, and hours of complaints — without ever showing fatigue, but instead offering unwavering support.

Abstract

The present thesis details the findings of a fatigue life investigation involving the use of Cu-HCP and CuCrZr as the inner liner material in regeneratively cooled cryogenic rocket engine combustion chambers. The experimental part of the study employs Thermomechanical Fatigue (TMF) panels. A TMF panel represents a small portion of a regeneratively cooled rocket combustion chamber, typically seven cooling channels. These panels undergo cyclic testing until failure at the TMF test bench located at the DLR Institute of Space Propulsion. Supercritical nitrogen serves as the coolant, replacing hydrogen or methane. The TMF test bench features a high-power diode laser that cyclically emits onto the TMF panel surface, mimicking multiple load cycles, as particularly present in reusable rocket engines. This setup isolates the pure mechanical behavior of the material from combustion or chemical influences. Additionally, the accurate determination of heat flux, surface temperature, and mass flow rate provide precise input data for numerical simulation and validation. Overall, four test campaigns were conducted. A heat transfer test (HTT) panel investigates the relation of surface temperature, mass flow rate and heat flux for Cu-HCP. Two TMF panel test campaigns with panels made from Cu-HCP studied the influence of the surface temperature at $T_s = 800$ K and $T_s = 900$ K. The higher temperature causes a decrease of 12 % of the fatigue life. The remaining test campaign was dedicated to a CuCrZr TMF panel with $T_s = 800$ K. This panel yields a fatigue life of 427 % when compared to the same conditions of the Cu-HCP TMF panel. All TMF panel tests were conducted with a wall heat flux of $q_w = 24.25$ MW/m^2.

With the experimental data of the HTT panel a coupled analysis in ANSYS using a CFX component and a steady state thermal component in Mechanical was validated. This verified analysis provided the temperature distribution that served as a key input for the following finite elements analysis in ANSYS Mechanical to numerically determine the stress and strain development of the remaining three TMF panels. Three nonlinear material models were compared. Two material models were implemented by user programmable features (UPF), one for each material. Additionally, the TMF panels were simulated using the models already embedded in the ANSYS software package. Therefore the kinematic hardening model developed by Chaboche, the isotropic harden-

ing and softening model following Voce, Norton's creep law, and the strain rate dependency model according to Peirce were utilized. The mechanical material parameters for the already embedded models are determined through an extensive test series, encompassing complex low cycle fatigue (CLCF) and tensile tests on uni-axial specimens, covering a temperature range from cryogenic conditions at $T = 77$ K to $T = 1000$ K. The material data for the UPFs were determined in the framework of a project for Cu-HCP and taken from literature, respectively. To estimate the fatigue life, a post-processing tool is developed and employed in MATLAB combining a ductile damage model according to Bonora and a brittle damage model developed by Lemaitre. The useful fatigue is introduced. It characterizes the number of cycles of a TMF panel after that high deformation and deformation rates are initiated due to the formation of macro cracks. This effect can be observed in the experimental data and is defined in the numerical results by the critical damage being reached at the innermost point of the heat loaded wall. Both, experimentally and numerically obtained number of cycles match very well.

Kurzfassung

Die vorliegende Arbeit dokumentiert die Ergebnisse einer Ermüdungslebensdaueruntersuchung unter Verwendung von Cu-HCP und CuCrZr als Materialien der inneren Wand in regenerativ gekühlten kryogenen Brennkammern von Raketenmotoren. Der experimentelle Teil der Studie verwendet so genannte Thermomechanische Ermüdungs-Panels (TMF Panel). Ein TMF Panel repräsentiert einen kleinen Ausschnitt einer regenerativ gekühlten Raketenbrennkammer mit typischerweise sieben Kühlkanälen. Diese Panels werden zyklisch bis zum Versagen auf dem TMF Prüfstand am DLR Institut für Raumfahrtantriebe getestet. Als Kühlmittel dient überkritischer Stickstoff, der Wasserstoff oder Methan ersetzt. Der TMF Prüfstand verfügt über einen Hochleistungsdiodenlaser, der zyklisch auf die Oberfläche der TMF-Platte strahlt und mehrere Lastzyklen nachahmt, wie sie insbesondere bei wiederverwendbaren Raketenmotoren auftreten. Diese Anordnung isoliert das reine mechanische Verhalten des Materials von Einflüssen durch Verbrennung oder Chemikalien. Darüber hinaus ermöglicht die genaue Bestimmung von Wärmestromdichte, Oberflächentemperatur und Massenstrom präzise Eingangsdaten für numerische Simulationen und deren Validierung. Insgesamt wurden vier Testkampagnen durchgeführt. Ein Wärmeübertragungstest (HTT) Panel untersucht die Beziehung zwischen Oberflächentemperatur, Massenstrom und Wärmestromdichte für Cu-HCP. Zwei TMF Panel Testkampagnen mit Panels aus Cu-HCP untersuchten den Einfluss der Oberflächentemperatur auf die Lebensdauer bei $T_\mathrm{s} = 800$ K und $T_\mathrm{s} = 900$ K. Die höhere Temperatur führt zu einer Abnahme der Lebensdauer um 12 %. Die verbleibende Testkampagne wurde mit einem CuCrZr TMF Panel mit $T_\mathrm{s} = 800$ K durchgeführt. Dieses Panel zeigt eine Lebensdauer von 427 % im Vergleich zu den gleichen Bedingungen des Cu-HCP TMF Panels. Alle TMF Panel Tests wurden mit einer Wandwärmestromdichte von $q_\mathrm{w} = 24.25$ MW/m^2 durchgeführt.
Mit den experimentellen Daten des HTT Panels wurde eine gekoppelte Analyse in ANSYS validiert, wobei die Kopplung eine CFX-Komponente und eine stationäre thermische Komponente in Mechanical verwendet hat. Diese verifizierte Analyse lieferte die Temperaturverteilung innerhalb des Panels, die als entscheidende Eingabe für die folgende Finite-Elemente-Analyse in ANSYS Mechanical diente, um die Spannungs- und Dehnungsentwicklung der verbleibenden

drei TMF Panels numerisch zu bestimmen. Drei nichtlineare Materialmodelle wurden verglichen. Zwei Materialmodelle wurden über benutzerprogrammierbare Funktionen (UPF) implementiert, eines für jedes Material. Zusätzlich wurden die TMF Panels unter Verwendung der bereits im ANSYS Softwarepaket eingebetteten Modelle simuliert. Hierzu wurden das kinematische Verfestigungsmodell nach Chaboche, das isotrope Ver- und Entfestigungsmodell nach Voce, das Nortonsche Kriechgesetz und das Modell für Dehnratenabhängigkeit nach Peirce verwendet. Die mechanischen Materialparameter für die bereits eingebetteten Modelle wurden durch eine umfangreiche Testreihe bestimmt, die komplexe zyklische Ermüdungs- (CLCF) und Zugversuche an uniaxialen Proben umfasste und einen Temperaturbereich von $T = 77$ K bis $T = 1000$ K abdeckte. Die Materialdaten für die UPFs wurden für Cu-HCP im Rahmen eines Projektes bestimmt bzw. aus der Literatur entnommen. Zur Abschätzung der Ermüdungslebensdauer wurde in MATLAB ein Post-Processing-Tool entwickelt und verwendet, das ein duktiles Schädigungsmodell nach Bonora und ein sprödes Schädigungsmodell nach Lemaitre kombiniert. Dabei wird die nutzbare Lebensdauer eingeführt, welche die Anzahl der Zyklen eines TMF Panels charakterisiert, infolge derer hohe Verformungen und Verformungsraten aufgrund der Bildung von Makrorissen eingeleitet wurden. Dieser Effekt kann in den experimentellen Daten beobachtet werden und wird in den numerischen Ergebnissen durch das Erreichen der kritischen Schädigung am innersten Punkt der wärmebelasteten Wand definiert. Die experimentell und die numerisch ermittelte Anzahl der Zyklen stimmen sehr gut überein.

Contents

List of Figures

List of Tables

List of Symbols

	Symbols	
$\dot{m}$	Mass Flow Rate	kg s^{-1}
$\dot{p}$	Plastic Strain Rate	s^{-1}
A	Area	m^2
b	Isotropic Hardening Parameter	–
Bi	Biot Number	–
C	Isotropic Elasticity Tensor	N mm^{-2}
C_{1-3}	Norton Creep Parameters	–
C_i	Kinematic Hardening Constant	N mm^{-2}
c_p	Specific Heat Capacity	J kg^{-1} K^{-1}
D	Damage Variable	–
d	Distance	mm
E	Young's Modulus	N mm^{-2}
f	Frequency	Hz
G	Total Irradiation	W m^{-2}
H	Enthalpy	kg m^2 s^{-2}
h	Heat Transfer Coefficient	W m^{-2} K^{-1}
h_s	Equivalent Sand Grain Roughness	m
I	Current	A
I	Intensity	MW m^{-2}
K	Viscous Material Parameter	–
l	Length	m
L_E	Entry Length	m
m	Strain Rate Dependend Hardening Parameter	–
n	Mol Number	mol
n	Viscous material Parameter	–
P	Power	W
p	Pressure	–
Pr	Prandtl Number	
Q	Activation Energy	J mol^{-1}
q	Heat Flux	W m^{-2}
r	Radius	mm
$R_0,\ R_\infty$	Isotropic Hardening Parameter	N m^{-2}

R_a	Average Roughness	μm
R_z	Maximum Roughness	μm
R_ν	Geometric Parameter	–
Re	Reynolds number	mm
S	Entropy	J K^{-1}
s	Thickness of Layer	mm
$S_{1,2}$	Fatigue Damage Parameters	–
T	Temperature	K
t	Thickness	mm
t	Time	s
U	Voltage	V
u	Displacement	mm
u	Velocity	m s^{-1}
V	Volume	m^3
w	Width	mm

Greek Symbols

α	Absorptivity	–
α	Backstress	N m^{-2}
α	Damage Exponent	–
α	Thermal Diffusivity	m^2 s^{-1}
α_k	Stress Concentration Factor	–
$\bar{\alpha}$	Thermal Expansion coefficient	10^{-6} K^{-1}
β	Angular Separation of Cooling Channels	–
β	Relative Stress	N m^{-2}
η	Dynamic Viscosity	kg s^{-1} m^{-1}
γ	Viscosity Parameter	–
γ_i	Kinematic Hardening Constant	–
λ	Heat Conductivity	W m^{-1} K^{-1}
λ	Wavelength	nm
ν	Kinematic Viscosity	m^2 s^{-1}
ν	Poisson's Ratio	–
Ψ	Helmholtz Free Energy	kg m^2 s^{-2}
ρ	Density	kg m^{-3}
ρ	Reflectivity	–
σ	Stress	MPa
σ'	Stress Deviator	MPa
τ	Transmissivity	–
θ	Angle	–
ε	Emissivity	–

ε	Strain	–
φ	Angle	–
φ^*	Geometry Function	–

Subscripts

∞	Environmental Condition
*	
0	Initial Condition
b	Bulk Conditions
cc	Cooling Channel
cr	Critical
ctrl	Control
du	Ductile
eq	Equivalent
f	Fatigue
h	Hydraulic
m	Hydrostatic
m	Melting Point
ref	Reference
s	Surface
sat	Saturation Conditions
th	Threshold
tot	Total
w	Wall

Superscripts

cr	Creep
e	Elastic
pl	Plastic
th	Thermal
vp	Viscoplastic

Abbreviations

BoE	Balance of energy
CFD	Computational Fluid Dynamics
CLCF	Complex Low Cycle Fatigue
CP	Central Point
DIC	Digital Image Correlation
DLR	German Aerospace Center
DSC	Differential Scanning Calorimeter
EDM	Electric Discharge Machining

FEA	Finite Element Analysis
FRP	Flight Recovery Programme
FS	Full Scale
GCH4	Gaseous Methane
GOX	Gaseous Oxygen
HARCC	High Aspect Ratio Cooling Channel
HCP	High Conductivity Phosphorus Deoxidized Copper
HTT	Heat Transfer Test Panel
IR	Infrared
ITT	Interupted Tensile Test
IWM	Fraunhofer Institute for Mechanics of Materials
IWS	Fraunhofer Institute for Material and Beam Technology
LCF	Low Cycle Fatigue
LFA	Laser Flash Analysis
LH2	Liquid Hydrogen
LOX	Liquid Oxygen
LRE	Liquid Rocket Engine
MV	Material Variation
NASA	National Aeronautics and Space Administration
NETD	Noise Equivalent Temperature Difference
NI	National Instruments Corporation
NIST	National Institute of Standards and Technology
NTR	Newton Trust Region
OFHC	Oxygen Free High Conductivity
PVD	Physical Vapour Deposition
RANS	Reynolds Averaged Navier-Stokes
RGP	Real Gas Properties
RMS	Root Mean Square
SAM	Standard ANSYS Mechanical
SLM	Selective Laser Melting
SSME	Space Shuttle Main Engine
SST	Shear-Stress Transport
SSTR	Steady-State Thermoreflectance
TMA	Thermomechanical Analyzer
TMF	Thermomechanical Fatigue
TUM	Technical University of Munich
TV	Temperature Variation
UPF	User Programmable Feature

	Constants	
σ	Stefan-Boltzman Constant	5.670×10^{-8} W m^{-2} K^{-4}
R	Universal Gas Constant	8.314 J mol^{-1} K^{-1}
	Other	
∇	Nabla Operator	

1 Introduction

1.1 Motivation

Regeneratively cooled liquid rocket engines (LRE) remain to be crucial elements in numerous space transportation systems. However, Preclik [1] states that approximately 60 % of launch vehicle failures can be traced back to the propulsion system (as of 2010). Among its components, the combustion chamber of the engine stands out as one of the most vital, facing the challenge of enduring intense hot and cold temperatures, extreme temperature gradients, high pressures and high pressure differences. Typically, an expandable rocket engine is designed for 4 (RD-120) to 20 (Vulcain I & II) cycles [1]. Assuming a safety factor of 2-3 and including engine acceptance testing and at least one launch abort, the margins of the engine fatigue life become very small.
The Space Shuttle Main Engine (SSME) was the first reusable high thrust rocket engine developed from 1971 onward by Rocketdyne Division, Rockwell. It was designed for 55 flights with a total burn time of 27,000 s [2]. However, on average a single SSME was only used for 8 flights. Though, Harris [2] mentions that at least one unit of the SSME has been tested for the full design life. Currently the Merlin 1D engine developed by SpaceX for the Falcon 9 and Falcon Heavy launch vehicles is the state of the art reusable liquid rocket engine. Though, at the time of this writing, little information is available on the designed life span and actual number of reuses. Generally, reusability of first stage boosters is the current trend in modern rocket development. Companies like Rocket Lab USA, maiaspace, Orbex and others plan to eventually reuse their rockets. Reusability introduces cyclic loading and unloading of the components of the engine, increasing the risk of failure. In particular, the combustion chamber can experience thermomechanical fatigue (TMF) after very few cycles. Hence, TMF in liquid rocket engines is counted among low cycle fatigue (LCF). The thermomechanical fatigue is induced by the accumulation of plastic strains within each cycle, creep of the material and ratcheting. Due to these mechanisms the combustion chamber wall between the cooling channels and the hot gas side gradually deteriorates and thins until the wall ultimately ruptures. This failure mode is commonly known as the "doghouse-effect" [3]. A recent example of the effects of a ruptured combustion chamber wall (though

through a different root cause) was the failure of Astra's Rocket 3.3 on June 12^{th}, 2022. Due to the failure of the wall, the coolant was dumped directly into the combustion chamber, increasing the fuel consumption until the launch vehicle ran out of fuel without reaching orbit [4]. Additionally, chemical reactions, blanching, hydrogen embrittlement, combustion instabilities as well as pressure and heat flux variations further decrease the life time of a combustion chamber. Consequently, the choice of the material is of high importance. For high thrust liquid rocket engines copper alloys are the standard material chosen as inner liner of the combustion chamber jacketed with a stiffer material such as Nickel [5]. Copper is chosen due to its very high thermal conductivity while Nickel serves as the thrust frame.
Today, new liquid rocket engines are mainly developed using numerical simulation tools such as Finite Element Analysis (FEA) and Computational Fluid Dynamics (CFD). Hence, there is a high demand for validated simulations and procedures. But full scale test campaigns over the full designed life of a liquid rocket engine like previously mentioned for the SSME are very expensive, time consuming and dangerous [6]. Particularly, in early stages of development and design, when it comes to material selection and heat transfer characteristics, full scale tests are simply not available. At the German Aerospace Center (DLR) Institute of Space Propulsion the thermomechanical fatigue panel test bench [7–10] was developed to generate data closely resembling real-world conditions for validating numerical models in computational fluid dynamics, thermal and structural analysis, and material performance. This is achieved through the use of miniature TMF panels, which are representations of the inner liner of an actual liquid rocket engine's combustion chamber. Typically featuring 5-7 cooling channels, these panels undergo cyclic thermal loading provided by a laser to emulate the heating from hot gas, simulating the doghouse effect and typical failure mechanisms in liquid rocket engines. This approach helps minimize the necessity for small scale and full-scale tests involving actual combustion. Also accounting for safety and cost-effectiveness, the TMF panel is cooled using supercritical nitrogen. With TMF panel tests, the purely mechanical performance of the material, without the influence of combustion phenomena like fluctuations of pressure and heat flux, abrasion, blanching [11] and hydrogen embrittlement, can be evaluated. Additionally, the boundary conditions, particularly heat flux, temperature, pressure and mass flow rate are precisely controlled.
In the framework of this thesis four TMF panel tests were executed to examine the influence of the surface temperature and different material performance. Three test campaigns were performed with the TMF panel made from Cu-

HCP (High Conductivity Phosphorus Deoxidized Copper), one utilized a Cu-CrZr (Copper-Chromium-Zirconium) alloy as TMF panel material. The first test campaign was solely dedicated to the heat transfer characteristics of the Cu-HCP material, the remaining test campaigns were actual thermomechanical fatigue tests. The Cu-HCP test campaigns focused on the influence of the panel's surface temperature on the fatigue life. The last test campaign demonstrated the variation of the fatigue life for Cu-HCP and CuCrZr. The tests were executed at highly similar boundary conditions, hence, a unique comparison of the individual factors, temperature and material is feasible. Furthermore, a novel approach has been developed using the results of the TMF panel tests for the estimation of their fatigue life performance and eventually the application to a LRE segment. This approach consists of a fluid-thermal simulation in ANSYS that was validated by comparison to measurements of temperature distribution, pressure loss in the cooling channel and coolant outlet temperature in order to achieve an accurate thermal field. The thermal field obtained in the cross section of maximum temperature is then fed into a quasi 2-dimensional static structural simulation in ANSYS Mechanical. This yields the stress and strain distribution of the cross section for the initial 5 cycles. In the numerical analysis in ANSYS Mechanical three different material models are used and compared. Finally, a damage based post-processing tool is developed to calculate the evolution of damage in the hot gas wall on several points of interest in the cross section. The procedure provides a validated estimation of the so-called "useful fatigue life" of the TMF panels. The useful fatigue life determines the number of cycles for a TMF panel before macro-crack initiation leads to a rapid accumulation of damage followed by complete failure. It aims for a fast estimation of the combustion chamber fatigue life that can be used in early stages of rocket engine design without the need for large and time consuming computational resources.

1.2 State of the Art

The first experimental setup related to TMF panels was presented by Carden in 1966 [12]. It was designed to investigate the low cycle thermal fatigue in cryogenically cooled nozzles of nuclear rockets for interplanetary missions. The actual TMF panel consisted of six thin-walled circular tubes made of the nickel base alloy *Hastelloy X*. The tubes were brazed to each other and onto a planar base plate also made of *Hastelloy X*. It was instrumented with numerous thermocouples to collect detailed information on temperature distribution. A quartz lamp radiant furnace provided a measured heat flux of $q \approx 1.1$ MW/m^2.

Liquid nitrogen (LN_2) at a temperature of $T_{LN_2} = -200$ °F (144.3 K) was used as a coolant. The cycle hold time was either $t_{on} = 15$ s or $t_{on} = 5$ min with a maximum surface temperature during a cycle of $T_s = 1900$ °F (1310.9 K). As conclusions Carden stated that thermal fatigue can be a serious problem for regeneratively cooled rocket nozzles. The simplified method of using a TMF panel seemed appropriate for modeling the low cycle fatigue life characteristics and the loading time can shorten the fatigue life significantly. After the work of Carden the development of the Space Shuttle Main Engine (SSME) triggered a wealth of publications on thermomechanical fatigue of liquid rocket engines on both, experimental and numerical investigations, available on NASA's Technical Reports Server (NTRS) [13]. However, only cylindrical sub-scale combustion chambers were used and tested until failure. Notably, Miller [14] described the experimental results and modeling of a Cu-OFHC combustion chamber. Further investigations into cylindrical thrust chambers have also been used in the work of Kasper [15] and Hannum [16]. A different combustion chamber type, called Plug Nozzle Thrust Chamber, was used by Quentmeyer [3] in 1977. He used 22 cylindrical test sections of thrust chambers made from *Amzirc*, *NARloy-Z* and *Cu-OFHC* of which 21 were tested until failure. Armstrong performed numerical simulations on the combustion chamber setup with limited number of elements in 1979. Further development of the model was conducted by Baslani [17]. The same test setup was used by Pavli [18] and Jankovsky [19]. Cook et. al. [20] prepared an extensive report on the investigations for the development of the SSME in 1983. Arya still used Quentmeyer's results for an improved viscoplastic [21] and nonlinear [22] analysis as computational resources had improved.
The failure of Ariane 5 flight V517 in 2002 was traced back to the nozzle of the Vulcain 2 engine nozzle losing its mechanical integrity [23, 24]. The subsequent Ariane 5 Flight Recovery Programme (FRP) triggered the development of a thermoshock test bench at Fraunhofer IWS [25] utilizing TMF panels again for rapid but close-to-reality experiments. A Nd-YAG solid-state laser was used with a maximum power of $P = 4.4$ kW. The maximum heat flux was limited to $q = 5$ MW/m^2 and the panel was cooled with liquid nitrogen. Based on the results and experience gained during the FRP, the TMF panel test bench was developed at DLR Lampoldshausen focusing on the requirements of future propulsion. In 2007 Riccius presented the concept for an improved TMF panel test bench [7] that was established subsequently by Gernoth [26]. Consequently, Gernoth presented the first results of nozzle-type TMF panel tests [27, 28]. In 2013 he used this data to validate fluid dynamical models, notably the pressure loss, with the experimentally identified sand grain rough-

ness [8]. However, in 2009 Riccius [29] suggested to shift the research focus to combustion chamber-type TMF panels demanding an increased heat flux. This was realized by means of new focusing optics yielding an enhancement from $q = 8$ MW/m^2 to $q = 25$ MW/m^2 (laser intensity $I = 28$ MW/m^2). The results of the High Aspect Ratio Cooling Channel (HARCC) [30] geometry and first generation (1G) combustion chamber-type TMF panels with five cooling channels were published in 2012 [31] and afterwards compared with a corresponding FE fatigue life analysis [32]. Based on this experimental data Thiede could validate progressive stages of development of his damage parameter based FEA [33–35]. Additional combustion chamber-type TMF panel tests were conducted and evaluated by Schwarz for validation of his model of fatigue life analysis [36]. For the tests of the second generation (2G) of combustion chamber type TMF panels the test bench was upgraded from five to seven cooling channels in which the mass flow rate can be individually controlled. Thiede conducted the 2G-experiments with TMF panels made from CuCrZr in 2018 and subsequently used these results for validation of his final damage parameter based FEA [9], an extension of the work performed by Tini [37]. In parallel Thiede developed the third (3G) generation of TMF panels with an increased maximum strain. Subsequently, the fourth (4G) generation TMF panel was developed incorporating a similar setup regarding the cooling channel design but with additional features for manufacturing with Selective Laser Melting (SLM). Results of the first test campaign of a 3G TMF panel made of CuCrZr were presented by Kringe [10]. Following that, a test series of three 3G TMF panel tests made of Cu-HCP was conducted [38–40]. The results of this test campaign and an additional TMF panel test again made from CuCrZr are presented in this thesis. At the same time Hötte conducted TMF panel tests with a different setup [41, 42] in the framework of the *Sonderforschungsbereich (SFB) Transregio (TRR) 40* [43]. A modular combustor with gaseous oxygen (GOX) and gaseous methane (GCH_4) was used. Fassin used the experimental results to validate his simulations [44].

2 Theoretical Background

This chapter gives an overview on the theoretical background of the work executed within this thesis. It describes the general equations used for modeling in Standard ANSYS Mechanical (SAM), the User Programmable Features (UPF) applied, damage calculations and physical background on heat transport phenomena as an integral part of the temperature distribution in the TMF panel. Note that generally true stresses and strains denoted as σ and ε are used throughout this thesis if not noted otherwise. The true stress σ_{true} is obtained from the engineering stress σ_{eng} by

$$\sigma_{\text{true}} = \sigma_{\text{eng}} \left(1 + \varepsilon_{\text{eng}}\right) \tag{2.1}$$

and the true strain $\varepsilon_{\text{true}}$ is obtained from the engineering strain ε_{eng} by

$$\varepsilon_{\text{true}} = \ln \left(1 + \varepsilon_{\text{eng}}\right). \tag{2.2}$$

2.1 Model in Standard ANSYS Mechanical

Generally, the state of a material is defined by its observable variables [45]. These are elastic strain, temperature, temperature gradient and internal state variables. The Helmholtz free energy is chosen as the thermodynamic state potential. The potential can be split into its elastic and plastic part

$$\Psi = \Psi \left(\varepsilon^{\text{e}}, r, \alpha, T\right) = \Psi^{\text{e}} \left(\varepsilon^{\text{e}}\right) + \Psi^{\text{pl}} \left(\alpha, r\right) \tag{2.3}$$

To simulate the material behavior in ANSYS Mechanical the chosen non-linear model comprises four different particular models [46] each one describing a different aspect of the observed material performance:

- Non-linear kinematic hardening according to Chaboche [47, 48]
- Non-linear isotropic hardening and softening according to Voce [49]
- Strain rate dependency of the stress according to Peirce [50]
- The secondary creep model according to Norton [51]

The different models are described in this section. ANSYS Mechanical employs the nonlinear kinematic hardening model, proposed by CHABOCHE [48, 52]. The original rate-independent version is used [53]. The CHABOCHE model is a constitutive model commonly used in materials science and engineering to describe the cyclic plastic behavior of materials under varying loading conditions. From a mathematical perspective, the model characterizes a function that relies on the equivalent plastic strain rate $\dot{\varepsilon}^{\mathrm{pl}}_{\mathrm{eq}}$, thereby inducing a shift in the origin of the yield surface within the stress space [47]. The shift is known as the "backstress", conventionally referred to as α. The backstress describes the additional stresses that remain after unloading. It accounts for the history-dependent nature of plastic deformation and is capable of modeling ratcheting. It uses the VON MISES yield criterion

$$f\left(\sigma, \sigma_{\mathrm{y}}\right) = \sigma_{\mathrm{e}} - \sigma_{\mathrm{y}} = 0 \tag{2.4}$$

with σ_{e} being the VON MISES effective stress and σ_{y} is the yield strength corresponding to the yield in uniaxial loading. The uniaxial yield stress is the sum of the initial yield stress σ_0 and the backstress component α

$$\sigma_{\mathrm{y}} = \sigma_0 + \alpha \tag{2.5}$$

The backstress is given by the superposition of several components defined by

$$\alpha = \sum_{i=1}^{n} \alpha_{\mathrm{i}} \tag{2.6}$$

The ANSYS Manual [54] recommends $i = 3$. A kinematic hardening rule according to ARMSTRONG AND FREDERICK [55] describes the individual backstress components α_{i}

$$\dot{\alpha}_{\mathrm{i}} = \frac{2}{3} C_{\mathrm{i}} \dot{\varepsilon}^{\mathrm{pl}}_{\mathrm{eq}} - \gamma_{\mathrm{i}} \dot{\bar{\varepsilon}}^{\mathrm{pl}}_{\mathrm{eq}} \alpha \tag{2.7}$$

where C_{i} and γ_{i} are the material kinematic hardening constants and $\dot{\bar{\varepsilon}}^{\mathrm{pl}}_{\mathrm{eq}}$ is the magnitude of the plastic strain rate. In Equation (2.7) the first term is the hardening modulus, the second term is called "recall-term" introducing the nonlinearity. The CHABOCHE kinematic hardening model is frequently integrated with the VOCE nonlinear isotropic hardening model, as indicated by PETRY [56]. The latter was initially formulated by VOCE [49]. Mathematically, isotropic hardening or softening characterizes the expansion or contraction of the yield surface within the stress space, contingent upon the equivalent plastic

strain $\varepsilon_{\mathrm{eq}}^{\mathrm{pl}}$. This behavior is encapsulated by the isotropic hardening σ_{y}, which is determined by

$$\sigma_{\mathrm{y}} = \sigma_0 + R_0 \hat{\varepsilon}_{\mathrm{eq}}^{\mathrm{pl}} + R_\infty \left(1 - \exp\left(-b \hat{\varepsilon}_{\mathrm{eq}}^{\mathrm{pl}}\right)\right) \tag{2.8}$$

where $\hat{\varepsilon}_{\mathrm{eq}}^{\mathrm{pl}}$ is the equivalent plastic strain and R_0, R_∞, b are the isotropic hardening material parameters. Since the previous formulations only cover rate-independent plasticity, the model developed by Peirce [50] is chosen to cover the rate dependent plasticity of the material. Still, the von Mises criterion of Equation (2.4) applies. Hence, when exceeding the yield stress, higher plastic deformation rates cause higher stress in the material. Following, Peirce introduced the model

$$\sigma(\dot{\varepsilon}) = \left(1 + \frac{\dot{\varepsilon}}{\gamma}\right)^{\mathrm{m}} \sigma_0. \tag{2.9}$$

Herein $\sigma(\dot{\varepsilon})$ describes the strain rate dependent yield stress, γ describes the viscosity parameter and m is the strain rate dependent hardening parameter. A common method to cover creep and stress relaxation of a material during constant elevated temperatures is by using creep models. In the TMF panel this is necessary to model the material performance during extended heating time (laser-on). The Norton creep model is commonly used to model secondary creep but also usefully covers stress relaxation. It is described by

$$\dot{\varepsilon}^{\mathrm{cr}} = C_1 \sigma^{C_2} \exp\left(\frac{-C_3}{T}\right) \tag{2.10}$$

where C_1, C_2, C_3 represent the creep parameters and $\dot{\varepsilon}^{\mathrm{cr}}$ is the creep strain rate. The determination of the respective parameters for the material model in Standard ANSYS Mechanical is presented in Section 4.1.

2.2 Custom Material Model UPF

This section briefly describes the Custom Material Models for Cu-HCP and CuCrZ that were implemented by a User Programmable Feature in ANSYS [57].

2.2.1 UPF for Cu-HCP

The custom material model for Cu-HCP has been developed by Seifert at Offenburg University of Applied Sciences [58–63]. In the context of this work it

is used as a model for comparison since it uses established algorithms that have successfully proven the modeling of thermomechanical fatigue, for example in exhaust manifolds of turbochargers and aerospace applications. It does not contain any damage modeling so far. The time and temperature dependent plasticity model is based on the CHABOCHE model [47, 64]. The stresses σ are computed from the strains ε

$$\sigma = C\left(\varepsilon - \varepsilon^{\mathrm{th}} - \varepsilon^{\mathrm{vp}}\right) \tag{2.11}$$

with C being the isotropic elasticity tensor that contains the temperature dependent Young's modulus E as well as the Poisson's ratio ν, ε denotes the total strain, $\varepsilon^{\mathrm{th}}$ the thermal strain calculated according to Equation (2.12) and $\varepsilon^{\mathrm{vp}}$ is the viscoplastic strain calculated by Equation (2.13). The thermal strains are computed by

$$\varepsilon^{\mathrm{th}} = \bar{\alpha}\Delta T \tag{2.12}$$

where $\bar{\alpha}$ is the thermal expansion coefficient and $\Delta T = T - T_{\mathrm{ref}}$ with $T_{\mathrm{ref}} = 293$ K. The viscoplastic strain rate $\dot{\varepsilon}^{\mathrm{vp}}$ is calculated by

$$\dot{\varepsilon}^{\mathrm{vp}} = \frac{3}{2}\dot{p}\frac{\beta}{\beta_{\mathrm{eq}}} \tag{2.13}$$

where $\beta = \sigma' - \alpha$ denotes the relative stress calculated by the difference of the deviator of the stress tensor $\sigma' = \sigma - 1/3\ \sigma_{\mathrm{kk}}$ and the backstress tensor α. In contrast to the formulation in Equation (2.7), the rate formulation of the backstress tensor is extended by a static recovery contribution

$$\dot{\alpha}_{\mathrm{i}} = C_{\mathrm{i}}\dot{\varepsilon}^{\mathrm{vp}} - \gamma_{\mathrm{i}}\dot{p}\alpha_{\mathrm{i}} - R_{\mathrm{i}}\alpha_{\mathrm{i}} + \frac{\partial C_{\mathrm{i}}}{\partial T}\frac{1}{C_{\mathrm{i}}}\alpha_{\mathrm{i}}\dot{T} \tag{2.14}$$

β_{eq} is the VON MISES equivalent stress and $\dot{p}$ describes the equivalent viscoplastic strain rate obtained from the power law function

$$\dot{p} = \left\langle \frac{\beta_{\mathrm{eq}} - R_{\mathrm{p}}}{K} \right\rangle^{\mathrm{n}} \tag{2.15}$$

with K, n denoting the temperature dependent viscous material behaviour and $\langle x \rangle = 0.5\,(x + |x|)$. R_{p} is the isotropic hardening according to Equation (2.8).

2.2.2 UPF for CuCrZr

The custom material model for CuCrZr has been developed by MASUOKA AND RICCIUS [65] specifically to model a TMF panel test of the second generation

also made from CuCrZr. It is a combined model using viscoplasticity according to Chaboche [47] and continuum damage mechanics (CDM) relying on the effective stress concept of Lemaitre [66, 67]. Hence, the basic equations of the model are comparable to the two models described before. The insertion of the isotropic damage variable D into the governing equations is different and therefore emphasized here. The stress increment is calculated by

$$\dot{\sigma} = (1 - D)\, C\dot{\varepsilon}^{\mathrm{e}} - \dot{D}\tilde{\sigma} \tag{2.16}$$

combining Hooke's law, where C is the elastic constant matrix, and the effective stress tensor $\tilde{\sigma}$ calculated by Equation (2.21). Again, the total strain is composed of elastic (ε^{e}), viscoplastic ($\varepsilon^{\mathrm{vp}}$) and thermal ($\varepsilon^{\mathrm{th}}$) part. The viscoplastic fraction is calculated by Equation (2.13) and the thermal fraction by Equation (2.12). The damage variable is also introduced into the kinematic hardening

$$\dot{\alpha} = C_{\mathrm{i}}\,(1 - D)\,\dot{p} - \gamma \dot{r} \alpha \tag{2.17}$$

and isotropic hardening

$$R_{\mathrm{p}} = R_{\infty}\left(1 - \exp\left(-b\hat{\varepsilon}^{\mathrm{pl}}\right)\right) + R_0 r \tag{2.18}$$

where the factor r is

$$r = (1 - D)\,\dot{p} \tag{2.19}$$

The calculation of the damage variable is shown in the following section.

2.3 Damage - Postprocessing

The process of structural transformation within a material, involving the creation, enlargement, and integration of tiny flaws, is termed as damage. In its ultimate phase, this process culminates in the complete disintegration of bonds, resulting in the material separating and giving rise to a visible, large-scale crack. Material damage is categorized into different types based on the leading observable phenomenon: brittle damage, ductile damage, creep damage, and fatigue damage [68]. Brittle damage is primarily characterized by the origination and expansion of tiny cracks. Examples of this behavior can be seen in ceramics, geomaterials, and concrete. In contrast, the mechanisms driving ductile damage and creep damage in metals are primarily associated with the growth, merging, but also self-repair of minuscule cavities. In the context of fatigue damage, micro cracks initially form around areas of stress concentration due to repeated elasto-plastic loading. These cracks then propagate and

combine over time until the material fails. According to Lemaitre [69] the effects of damage are the decrease of material properties like Young's modulus, yield stress in combination with work hardening, hardness and density. From the experimental results and measurements conducted it is postulated that the thermal conductivity also decreases (see Section 5.5). In 1958 Kachanov [70] introduced a scalar damage variable

$$D = \frac{\delta S_{\mathrm{D}}}{\delta S} \tag{2.20}$$

for isotropic damage. It describes the ratio of the area of the microvoids S_{D} to the initial cross section S in a reference plane [69] so that the remaining undamaged area is $\tilde{S} = S - S_{\mathrm{D}} = S\,(1 - D)$. Following the concept of effective stress according to Rabotnov [71]

$$\tilde{\sigma} = \frac{\sigma}{1 - D} \tag{2.21}$$

and applying the principle of strain equivalence according to Lemaitre and Chaboche [69] as well as $\sigma = E\varepsilon^{\mathrm{e}}$ and $\tilde{\sigma} = \tilde{E}\varepsilon^{\mathrm{e}}$ yields [72]

$$\tilde{\sigma} = \frac{E}{\tilde{E}}\sigma = \frac{\sigma}{1 - D} \quad \rightarrow \quad D = 1 - \left(\frac{\tilde{E}}{E_0}\right). \tag{2.22}$$

Hence, damage describes the loss of stiffness and can be obtained by measuring i.e. the reduction of the Young's Modulus in uniaxial tensile and low cycle fatigue tests as presented later in Section 4.1.1. From previous equations it is obvious that $D = 0$ corresponds to the virgin material and $D = 1$ to complete failure. However, experimental results show that real materials exhibit failure at $0.2 \lessapprox D \lessapprox 0.8$ [66]. In case of an LRE and also the TMF panel the damage propagation is a combination of ductile damage characterized by the ratcheting effect [73, 74] and fatigue damage induced by cyclic loading and unloading. The combination of both phenomenon was proposed by Schwarz [36]. Masuoka [65] then postulated the particular combination (Eqn. (2.23)) of the ductile damage model according to Bonora [75] and the fatigue damage model after Lemaitre and Desmorat [69] leading to the damage evolution law

$$\dot{D} = \dot{D}_{\mathrm{f}} + \dot{D}_{\mathrm{du}}. \tag{2.23}$$

Herein, D_{f} is the fatigue damage and D_{du} denoting the ductile damage contribution. Masuoka calculated the fatigue damage rate used in Equation (2.23)

according to Lemaitre and Desmorat [69] by

$$\dot{D}_{\mathrm{f}} = \left(\frac{Y}{S_1}\right)^{S_2} \dot{p} \tag{2.24}$$

with $S_{1,2}$ being the fatigue damage parameters, and $\dot{p}$ is the rate of accumulation of plastic strain calculated by

$$\dot{p} = \sqrt{\frac{2}{3}\dot{\varepsilon}^{\mathrm{p}}_{\mathrm{ij}}\dot{\varepsilon}^{\mathrm{p}}_{\mathrm{ij}}}. \tag{2.25}$$

Y represents the strain energy density release rate given by

$$Y = \frac{\sigma^2_{\mathrm{eq}} R_\nu}{2E_0\left(1-D\right)^2} \tag{2.26}$$

E_0 is the initial Young's modulus in the undamaged state and R_ν is a geometric parameter taking into account the triaxiality of stress (see Equation (2.29)). It is obtained by introducing the scalar damage variable D into the state potential in equation (2.3)

$$\Psi = \Psi\left(\varepsilon^{\mathrm{e}}, r, \alpha, T, D\right) = \Psi^{\mathrm{e}}\left(\varepsilon^{\mathrm{e}}, D\right) + \Psi^{\mathrm{pl}}\left(\alpha, r\right) \tag{2.27}$$

and subsequently deviate the potential with respect to damage

$$Y = -\frac{\partial \Psi}{\partial D} = \frac{1}{2}\varepsilon_{\mathrm{e}} : C[\varepsilon_{\mathrm{e}}]. \tag{2.28}$$

Hence, the strain energy release rate drives the damage progression [76]. Note that damage only affects the elastic part of the potential [75]. R_ν is calculated by

$$R_\nu = \frac{2}{3}\left(1+\nu\right) + 3\left(1-2\nu\right)\left(\frac{\sigma_{\mathrm{m}}}{\sigma_{\mathrm{eq}}}\right)^2 \tag{2.29}$$

where ν describes the Poisson's ratio, σ_{m} is the hydrostatic stress calculated by

$$\sigma_{\mathrm{m}} = \frac{1}{3} tr\left(\sigma\right) \tag{2.30}$$

and σ_{eq} is the VON MISES equivalent stress. The ratio $\sigma_{\mathrm{m}}/\sigma_{\mathrm{eq}}$ is the so-called stress triaxiality factor. For uniaxial loading $R_\nu = 1$ [69].
Referring back to equation (2.23), the ductile damage D_{du} is calculated by

$$D_{\mathrm{du}} = D_0 + \left(D_{\mathrm{cr}} - D_0\right)\left\{1 - \left[1 - \frac{\ln(\frac{p}{p_{\mathrm{th}}})}{\ln(\frac{p_{\mathrm{cr}}}{\varepsilon_{\mathrm{th}}})} f\left(\frac{\sigma_{\mathrm{m}}}{\sigma_{\mathrm{eq}}}\right)\right]^{\alpha}\right\} \tag{2.31}$$

with D_0 denoting the initial damage that is commonly set to $D_0 = 0$ and D_{cr} is the critical damage value at rupture. $f\left(\frac{\sigma_{\mathrm{m}}}{\sigma_{\mathrm{eq}}}\right)$ is the triaxiality function similar to R_ν. Furthermore, p_{cr} is the strain value at rupture, $\varepsilon_{\mathrm{th}}$ and p_{th} are the strain and accumulated plastic strain threshold. α denotes the damage exponent. According to Thomson and Hancock [77], Bonora [78] states that $\varepsilon_{\mathrm{th}}$ is scarcely affected by stress triaxiality, hence

$$\frac{p_{\mathrm{cr}}}{p_{\mathrm{th}}} = \frac{\varepsilon_{\mathrm{cr}}}{\varepsilon_{\mathrm{th}}}. \tag{2.32}$$

However, Bonora [79] also states that the critical strain $p_{\mathrm{cr}} \neq \varepsilon_{\mathrm{cr}}$. Hence he proposes an evolution law for the critical strain

$$p_{\mathrm{cr}} = \varepsilon_{\mathrm{th}} \left(\frac{\varepsilon_{\mathrm{cr}}}{\varepsilon_{\mathrm{th}}}\right)^{1/f(\sigma_{\mathrm{m}}/\sigma_{\mathrm{eq}})}. \tag{2.33}$$

This becomes important as the damage parameters are determined from uniaxial interrupted tensile tests (ITT) as will be shown later in Section 4.1.1. For the parameter determination in the uniaxial case equation (2.31) reduces to

$$D_{\mathrm{du}} = D_{\mathrm{cr}} \left\{1 - \left[1 - \frac{\ln(\frac{\varepsilon}{\varepsilon_{\mathrm{th}}})}{\ln(\frac{\varepsilon_{\mathrm{cr}}}{\varepsilon_{\mathrm{th}}})}\right]^{\alpha}\right\}. \tag{2.34}$$

The calculation of damage is a nonlinear process that is often coupled with nonlinear phenomenon in materials such as creep or visco-plasticity. Hence, for accurate modeling a fully coupled analysis of the whole structure is necessary. However, a post-processing of damage evolution is also possible as suggested by Lemaitre and Desmorat [69]. A post-processing approach decouples the structural analysis from the damage analysis. Therefore a nonlinear structural analysis can be performed with a subsequent time integration of the damage evolution laws. This approach is used in the present work to evaluate the fatigue life analysis of the TMF panels. The post-processing of the damage evolution law generally yields an upper bound for the fatigue life.

2.4 Heat Transfer and Thermal Field

Heat transfer can be divided into three mechanisms: conduction, convection and radiation. All three of them have a major impact in regeneratively cooled liquid rocket engines and also in the TMF panel investigations. In a LRE the heat flux is applied onto the inner liner by both, radiation and convection of

the hot combustion gases. In contrast to that in the TMF panel experiment only radiation provided by the laser is applied (see Section 3.2.1). Inside the hot gas wall heat conduction is the governing mechanism of heat transfer in both considered cases, the LRE and TMF panel. The same applies for the forced convection between the structure of the inner liner and the coolant flow in the cooling channel. According to that the three heat transfer mechanisms are described in this section in the frame of their relevance.

2.4.1 Conduction

Conduction describes the transfer of energy caused by the interactions of neighboring molecules or atoms. The kinetic energy of molecules rises if temperature rises, leading to intensified random motions [80]. In order to calculate the conductive heat flux $\vec{q}$, the temperature field in the observed medium has to be determined first. This can be derived by solving the heat diffusion equation which in its general formulation is

$$\frac{\partial}{\partial x}\left(\lambda\frac{\partial T}{\partial x}\right)+\frac{\partial}{\partial y}\left(\lambda\frac{\partial T}{\partial y}\right)+\frac{\partial}{\partial z}\left(\lambda\frac{\partial T}{\partial z}\right)+\dot{q}=\rho c_p\left(\frac{\partial T}{\partial t}\right) \tag{2.35}$$

where λ denotes the thermal conductivity, ρ the density, c_p the heat capacity and $\dot{q}$ is the rate of energy generation per unit volume of the medium. The detailed derivation can for example be found in the work of Incropera [80]. In the cases of a LRE and TMF panel considered here $\dot{q}=0$ as no heat is generated inside the combustion chamber wall. Note that for steady-state conditions also $\rho c_\mathrm{p}\dot{T}=0$. This is representing the amount of stored energy. The exact knowledge of the temperature field is also imperative for the fatigue life analysis as it is used to calculate the thermal stresses, expansions and hence displacements. The material parameters λ, ρ and c_p are commonly summarized by

$$\alpha=\frac{\lambda}{\rho c_\mathrm{p}} \tag{2.36}$$

where α is the thermal diffusivity [81]. Note that the notation here and throughout this thesis implies that all of these parameters are temperature dependent (e.g. $\alpha=\alpha\left(T\right)$). The heat flux can be calculated at any point in the medium by Fourier's Law [82]. For isotropic materials in 3-dimensional space it is defined as

$$\boldsymbol{q}=-\lambda\left(T\right)\nabla T \tag{2.37}$$

where ∇ is the Nabla Operator. The minus sign indicates that heat is always conducted from higher to lower temperatures.

2.4.2 Convection

Commonly, convection describes the heat exchange between a fluid and a solid body. The process of convection can be split in natural convection that is not driven by external forces but rather a difference in density of the fluid, and forced convection. Forced convection itself is further divided in combination with laminar flow or turbulent flow [83]. The heat exchanged is governed by the temperature difference of the participants and the local heat transfer coefficient h, hence [81] for the simplified one dimensional case

$$q = (T_\mathrm{w} - T_\mathrm{b}) \int_{A_\mathrm{s}} h dA_\mathrm{s} \tag{2.38}$$

where T_w is the wall temperature of the solid and T_b is the bulk temperature of the fluid. According to Herwig [81] T_b can be approximated as

$$T_\mathrm{b} = \frac{\Delta \dot{Q}}{\Delta \dot{S}_{\Delta \dot{\mathrm{Q}}}} = \frac{\dot{H}_\mathrm{out} - \dot{H}_\mathrm{in}}{\dot{S}_\mathrm{out} - \dot{S}_\mathrm{in}} \tag{2.39}$$

where $\dot{H}$ is the enthalpy flow rate and $\dot{S}$ is the entropy flow rate that is transported by $\Delta \dot{Q}$. The heat transfer coefficient h itself depends on the position and is integrated over the respective surface, but also depends on a variety of parameters. For example, it incorporates the properties of the boundary layer of the fluid and the heat transfer properties. The problem of convective heat transfer in LRE cooling channels has been covered in literature with special interest and a wealth of publications is available (see Gernoth [8], Haemisch [84], Kringe [38], Perakis [85], Torres [86]). Therefore, it shall not be covered here in detail. The numerical approach for the simulation of the heat transfer in ANSYS CFX is presented in Section 4.2.

2.4.3 Radiation

In the case of TMF panel tests heat transfer by radiation becomes important for absorption of the laser heating and to a very small extend to the emission of heat from the laser loaded surface. The total irradiation G onto a surface is the rate at which the radiation per surface unit area and from all directions and wavelengths occurs. According to Incropera [80]

$$G = \int_0^\infty \int_0^{2\pi} \int_0^{\pi/2} I_{\lambda,\mathrm{i}}\left(\lambda, \theta, \phi\right) \cos\theta \sin\theta \; d\theta \; d\phi \; d\lambda. \tag{2.40}$$

In case of the laser radiation with a constant wavelength and assuming irradiation on a planar surface with $\theta = 90°$ the equation greatly simplifies to

$$G = \frac{P}{A_{\text{focal}}} \tag{2.41}$$

where P is the laser power and A_{focal} is the area of the focal plane. To determine the incident heat flux for a real surface the absorbtivity α and reflectivity ρ has to be taken into account. For an opaque material without transmissivity ($\tau = 0$) they are linked by

$$\alpha + \rho = 1 \tag{2.42}$$

and

$$\alpha = \frac{G_\alpha}{G} \tag{2.43}$$

where G_α is the absorbed total irradiation. Note that KIRCHHOFF's law is also applied which states $\varepsilon = \alpha$ [80] for steady state conditions and the following notation in this thesis will use ε. The amount of heat transferred by radiation from the TMF panel itself to the surroundings and vice versa can roughly be estimated using the STEFAN-BOLTZMAN law according to KREITH [87]

$$\dot{Q} = \varepsilon \sigma A \left(T^4 - T_\infty^4\right) \tag{2.44}$$

where ε is the local emissivity (different for the laser heated surface and rest of TMF panel surface), σ is the Stefan-Boltzmann constant and T_∞ is the temperature of the environment.

2.4.4 Heat Flow Rate

The inward rate of heat flow is directly connected to the laser output power P_{out} and the emissivity $\varepsilon_{940\ \text{nm}}$ of the TMF panel surface at the wavelength of the laser. Note that the surface of the TMF panel is coated to increase the emissivity. Generally, the emissivity also varies with the coating's temperature. However, for the specific wavelength of $\lambda = 940$ nm measurements show (see Section 3.1.3) that $\varepsilon_{940\ \text{nm}}$ remains unaffected by temperature variations. Consequently, the inward rate of heat flow is represented by

$$\dot{Q}_{\text{in}} = P_{\text{out}} \varepsilon_{940\ \text{nm}} \tag{2.45}$$

where P_{out} is calculated using Equations (3.4) and (3.5). The outward rate of heat flow is calorically determined by the cumulative differences of enthalpy

$\Delta\dot{H}_\mathrm{i}$ of the N_2 coolant between the inlet and outlet of each cooling channel

$$\dot{Q}_\mathrm{out} = \sum_{i=1}^{7} \dot{m}_\mathrm{cc,i} \left(h_\mathrm{out,i} - h_\mathrm{in,i}\right). \tag{2.46}$$

2.4.5 Balance of Energy

The balance of Energy (BoE) consists of the summation of all net heat flows, encompassing conduction into the fluid supply system, convective and radiative exchanges with the environment, as illustrated by Equation (2.47). Here the relevant heat flows are convective heat transfer into the coolant $\dot{Q}_\mathrm{h}$, radiation from the laser $\dot{Q}_\varepsilon$, and conduction into the fluid supply system $\dot{Q}_\lambda$

$$\sum \dot{Q}_\lambda + \sum \dot{Q}_\varepsilon + \sum \dot{Q}_\mathrm{h} = 0 \tag{2.47}$$

This energy balance applies specifically to the TMF panel test, where convective and radiative interactions with the environment can be disregarded as their magnitude is very small. Note that $\sum \dot{Q}_\lambda$ could not be determined by a direct measurement but is calculated from Equation (2.47) as $\sum \dot{Q}_\mathrm{h} = \sum \dot{Q}_\mathrm{out}$ and $\dot{Q}_\varepsilon$ can be measured.

2.4.6 Fluid Flow

The three dimensional fluid flow is characterized by the Navier-Stokes-Equations [88–91] that are based on the conservation equations. In particular these are the conservation of mass calculated by

$$\int_\tau \frac{\partial \rho}{\partial t}\, \mathrm{d}\tau + \oint_\mathrm{A} [\rho \vec{v}] \cdot \vec{n}\, \mathrm{d}A = 0 \tag{2.48}$$

the conservation of momentum

$$\int_\tau \frac{\partial \rho \vec{v}}{\partial t}\, \mathrm{d}\tau + \oint_\mathrm{A} [\rho \vec{v}\vec{v} + \bar{\sigma}] \cdot \vec{n}\, \mathrm{d}A = \int_\tau \vec{f}_\mathrm{vol}\, \mathrm{d}\tau \tag{2.49}$$

and the conservation of energy obtained by

$$\int_\tau \frac{\partial \rho E}{\partial t}\, \mathrm{d}\tau + \oint_\mathrm{A} [\rho E \vec{v} + \bar{\bar{\sigma}}\vec{v} + \vec{q}] \cdot \vec{n}\, \mathrm{d}A = \int_\tau \vec{f}_\mathrm{vol} \cdot \vec{v}\, \mathrm{d}\tau \tag{2.50}$$

These equations need to be solved for every time step and every node in the model in ANSYS CFX. Additionally, the real gas equation

$$\left(p + \frac{an^2}{V^2}\right)(V - nb) = nRT \tag{2.51}$$

where a, b are parameters and n is the Mol-number, is used [92] as the nitrogen is in supercritical condition while it runs through the cooling channel. Parameters a, b are defined by

$$a = \frac{27R^2T_{\mathrm{cr}}^2}{64p_{\mathrm{cr}}} \qquad b = \frac{RT_{\mathrm{cr}}}{8p_{\mathrm{cr}}} \tag{2.52}$$

with the index $()_{\mathrm{cr}}$ indicating the critical conditions. Furthermore, to quantify the fluid flow in the cooling channels, the Reynolds number Re is used. The advantage is that it provides a handy method to compare fluid conditions at different temperatures, pressures, velocities and densities. Hence, in case of the TMF panel test, the experimental margins at the start of the laser can be comprised in the Reynolds number. In the context of this thesis the effective Reynolds number is of particular advantage for evaluation of the HTT panel test. The concept of the effective Reynolds Number Re_{eff} was originally proposed by Jones [93] for cooling channels with a rectangular cross-section. It is used throughout this thesis. It is denoted as Re. The effective Reynolds number is calculated by

$$Re_{\mathrm{eff}}^* = \frac{\rho u D_{\mathrm{h}}^*}{\eta}. \tag{2.53}$$

where u is the fluid velocity that is calculated according to the simplified one-dimensional continuity equation

$$\dot{m} = \rho A_{\mathrm{cc}} u. \tag{2.54}$$

D_{h}^* is the effective hydraulic diameter introduced by Jones for rectangular cross sections with

$$D_{\mathrm{h}}^* = \phi^* D_{\mathrm{h}} \tag{2.55}$$

with

$$D_{\mathrm{h}} = \frac{4A_{\mathrm{cc}}}{P_{\mathrm{cc}}} = \frac{2lw}{l+w} \tag{2.56}$$

where A_{cc} is the cross section, P_{cc} the perimeter and l and w denote the height and width of the cooling channel, respectively. ϕ^* is a geometry function defined by

$$\phi^* = \frac{2}{3}\left(1+\frac{w}{l}\right)^2 \left(1 - \frac{192w}{\pi^5 l}\sum_{n=0}^{\infty}\frac{\tanh\left(\frac{(2n+1)\pi l}{2w}\right)}{(2n+1)^5}\right). \tag{2.57}$$

For further details on the evaluation of the fluid flow regarding the TMF panel in particular the reader shall be referred to the work of Gernoth [8]. For the fluid flow in the cooling channels of rocket combustion chamber the work by Haemisch [84] shall be considered.

3 Experimental Setup

The experimental setup presents the methods and materials used in the TMF panel test campaigns. It describes the TMF panel itself, particularly the materials and geometry, and the TMF panel test bench at DLR Institute of Space Propulsion in Lampoldshausen with its components laser system, fluid system and measurement and control system. At the end, an overview of the specific properties of the four test campaigns is given.

3.1 TMF Panel Properties

This section describes the properties of the TMF panel in detail. Particular emphasis is given to the design, the manufacturing process and coating as well as to the chemical composition of the Cu-HCP material.

3.1.1 Geometry

The 3G TMF panel (see Fig. 3.1 and Fig. 3.2) serves as a scaled representation of the inner liner of the combustion chamber wall of a regeneratively cooled liquid rocket engine. It is predominantly crafted from a monolithic copper block, within which seven cooling channels are milled. Of these, the innermost five channels (numbered 2 - 6) represent the geometrical layout of regeneratively cooled rocket engines as detailed by Kuhl [94]. In contrast, the two outer cooling channels (numbered 1 & 7) possess a slightly larger cross-sectional area and are rotated by an angle of 90°. The actual cross section of a TMF panel is shown in Figure 3.2. Differing from a traditional LRE design, the outer nickel jacket is omitted, largely attributed to delamination issues identified in prior tests, and the potential for significant reductions in production costs. However, this omission leads to the absence of the hoop stress induced by the nickel jacket in the LRE cooling channels. To counterbalance this omission, cooling channels 1 and 7 are rotated and positioned outward, effectively cooling the massive outer edges. These modifications contribute to generating a tensile stress in the central cooling channel during the cooldown phase, ultimately leading to the targeted doghouse failure. It is noteworthy that although cooling channels 2 - 6 share the same geometry as the cooling channels in a LRE, but only

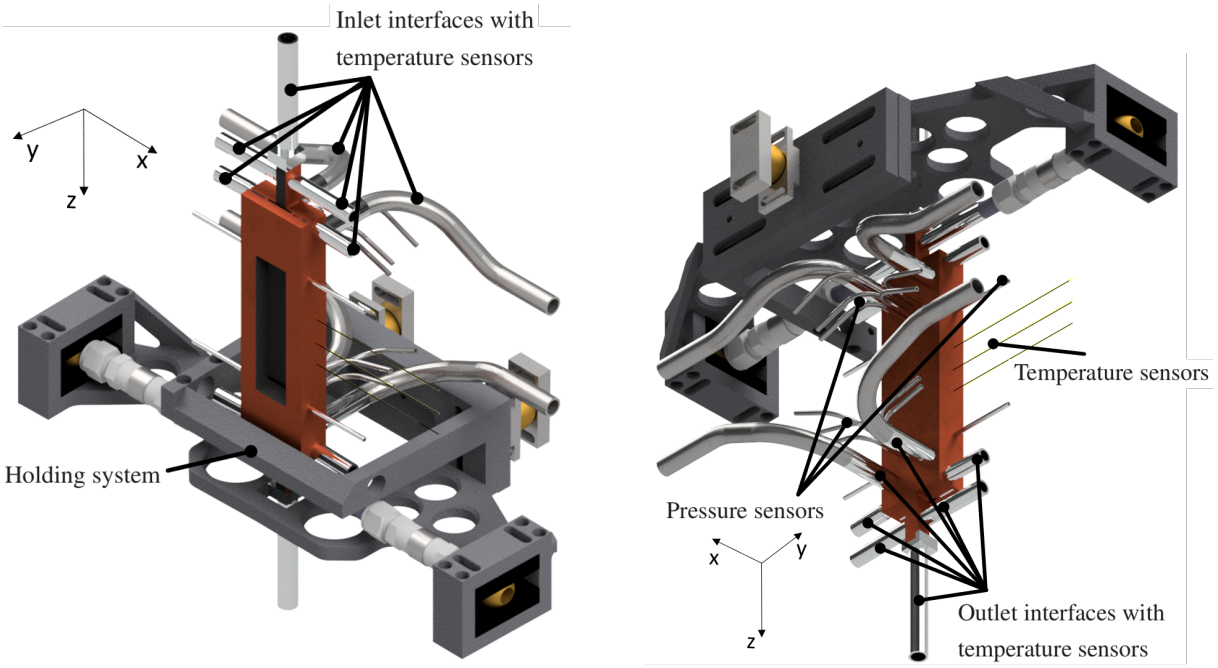

(a) Isometric view of the front of the 3G TMF panel

(b) Isometric view of the back of the 3G TMF panel

Figure 3.1: Isometric view of the TMF panel. Note that half of the holding system is suppressed for better visibility.

the central cooling channel is considered being representative to the stress and strain fields akin to the actual cooling channel in a LRE. Thus, it serves as the mechanically representative cooling channel. The other cooling channels (2, 3, 5, 6) are introduced to effectively attenuate the heat flux in a direction perpendicular to the flow (tangential or x direction). The pertinent dimensions of the TMF panel and cooling channels are enumerated in Table 3.1. The curvature of the laser loaded surface representing the combustion chamber wall takes on a cylindrical form with the rotational axis parallel to the flow direction, possessing a radius of $r = 130$ mm. With a consistent thickness of the laser-loaded wall segment, denoted as $d = 1$ mm, this configuration yields an angular separation of the cooling channels, quantified as $\beta = 1°$. This results in a fillet width, $w_\mathrm{f} = 1$ mm, at the interface with the laser-loaded wall. Figure 3.1 represents the comprehensive view of the TMF panel. The interfaces between the monolithic copper block and the test bench are made of MONEL400. They serve two primary purposes: firstly, they facilitate the connection of adapters to the fluid system (see Section 3.1.2), and secondly, they extend the flow path to ensure an uninterrupted flow within the laser-loaded area. The length L_E required for a non-disturbed turbulent flow is determined through the empirical

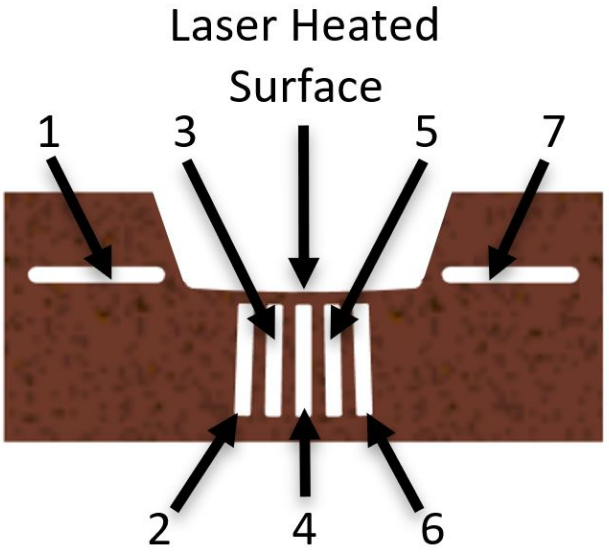

Figure 3.2: Cross section of the TMF panel

equation

$$\frac{L_{\mathrm{E}}}{D} = 1.6Re^{\frac{1}{4}} \tag{3.1}$$

according to White [95]. D is the diameter of the pipe. In this design configuration of the 3G TMF panel, the maximum strain at the peak surface temperature of $T_{\mathrm{s}} = 1000$ K is computed to be $\hat{\varepsilon} = 2\%$ within the central cooling channel.

3.1.2 Manufacturing

Ensuring the integrity of the material's micro-structure and surface during the manufacturing of the TMF panels is a paramount requirement to prevent potential impacts on both structural and thermal behavior, as well as heat transfer properties. To fulfill this demand, Electric Discharge Machining (EDM) is primarily employed. The distinct advantage of EDM is its capacity to exert negligible forces on the material while delivering highly localized heat input, thereby preserving the micro-structure of the cut surface. This dual attribute ensures consistent and reproducible quality in the produced TMF panels. Consequently, EDM is employed for the initial bore hole drilling of the cooling channels and the laser loaded area. Subsequent shaping involves wire-cutting of both regions into their final form. The frustum-shaped portion above the laser loaded surface is milled, followed by drilling holes for interfacing with the fluid system (as detailed in Section 3.2.2) and embedding pressure sensors (as

Total size	$48 \times 230 \times 20$ mm
Number of cooling channels	$5 + 2$
Laser heated wall thickness	1 mm
Cooling channel width	1.3 mm
Height of cooling channels 2 - 6	9 mm
Height of cooling channels 1 & 7	11 mm
Radius of cooling channel edge	0.24 mm
Angular separation of cooling channels	1°
Fillet width	1 mm
Shape of laser loaded surface	cylindrical, $r = 130$ mm

Table 3.1: Relevant design dimensions of the 3G TMF panel

described in Section 3.2.3). The connection pipes to the fluid system, composed of MONEL400, are laser-welded with Nickel welding wire to the copper TMF panel. Due to the diameter of the cutting wire, the cooling channels do not exhibit perfectly rectangular shapes. Instead, each corner has an average radius of $r_{\mathrm{cc}} = 0.239 \pm 0.006$mm. This radius significantly influences stress concentration in channel corners. In general, sharper edges correlate with higher stress peaks [96]. The stress concentration factor α_{k} is defined by

$$\alpha_{\mathrm{k}} = \frac{\sigma_{\mathrm{max}}}{\sigma_{\mathrm{n}}} \tag{3.2}$$

where α_{k} depends on r following

$$\lim_{r \to 0} (\alpha_{\mathrm{k}} \sigma_{\mathrm{n}}) = \infty. \tag{3.3}$$

behavior of a sharp-edged corner. Notably, THIEDE also utilized sharp-edged cooling channels for structural analysis, noting "the main damage initiation point is on the upper left corner of the adjacent cooling channel" ([9], p. 85). Given that real regeneratively cooled liquid rocket engines exhibit slight curvature in their cooling channel edges due to imperfect manufacturing, an accurate stress modeling in this region of the LRE is essential. A comparison of the TMF panel geometry with sharp and round edges within the framework of this thesis lead to about 10 % lower fatigue life for the sharp-edged corners. Table 3.2 illustrates the precision achieved in manufacturing the TMF panel, particularly with respect to the cooling channels and laser loaded wall. Evaluation with a KEYENCE VHX-5000 microscope is performed at a magnification of 200×.

[mm]	Height	Width	Radius	Wall
∅	9.031	1.334	0.239	0.968
Δ	0.031	0.034	N/A	-0.032
min	9.022	1.315	0.233	0.943
max	9.039	1.359	0.245	0.991

Table 3.2: Average accuracy of the dimensions of the cooling channels (2 - 6) and laser loaded wall of the TMF panel determined with a KEYENCE VHX-5000 with a magnification of 200× and deviation to the design dimensions

Note that there is no variation in dimensions between the two materials Cu-HCP and CuCrZr as manufacturing processes were identical. Surface roughness within the cooling channels is another critical aspect of manufacturing. It significantly affects turbulence, thereby influencing convective heat transfer and pressure drop along the channels [8]. Optical measurements were performed with the KEYENCE VHX-5000 microscope at several locations and in different directions with a magnification of 3000x and evaluated with the DIGITAL SURF MOUNTAINSMAP 8 software. The average roughness across the Cu-HCP and CuCrZr TMF panels is presented in Table 3.3. An exemplary measurement is listed in Appendix C.

[μm]	Cu-HCP		CuCrZr	
	Ra	Rz	Ra	Rz
∅	0.4614	3.0445	0.4184	2.0311
min	0.2187	1.3770	0.1741	0.9735
max	1.2300	7.0380	0.5620	3.1220

Table 3.3: Average roughness of the walls of the cooling channels and laser loaded surface of the TMF panel

3.1.3 Coating

The reflectivity ρ of copper at the wavelength of the laser (see Section 3.2.1) and an angle of incidence of 5° is in the range of $\rho_{940\ \mathrm{nm}} = 0.910 \ldots 0.993$ according to WERNER [97] and BABAR [98]. According to Equation (2.42) where the transmissivity τ can be set to zero, the absorptivity α (equal to the emissivity ε as stated in KIRCHHOFF's Law) is unsuitably small to provide high heat flux

rates into the TMF panel by the laser heat source. To counteract these circumstances a high emissivity layer is applied to the laser loaded surface of the TMF panel. This high emissivity layer has been developed at Fraunhofer Institute for Material and Beam Technology (IWS) for decorative aspects but serves also as a state of the art technology for the specific purpose as a high emissivity coating for the particular TMF panel test. It consists of three different layers which are applied by physical vapor deposition (PVD). The first layer is an undercoating made of Titanium (Ti) with a thickness of $s_{\mathrm{Ti}} \approx 0.25$ μm. The second layer is an oxygen barrier made of Nickel/Chromium (Ni/Cr). It has a thickness of $s_{\mathrm{Ni/Cr}} \approx 2.0$ μm. The outermost layer is the actual high emissivity coating. It is made of AlTiON and has a thickness of $s_{\mathrm{AlTiON}} \approx 3.0$ μm. The overall thickness of the coating has been determined by measurements with the Keyence VHX-5000 and a Keyence VHX 7000N. For all panels the thickness of the coating is identical in the range of $s_{\mathrm{tot}} = 4 \ldots 6$ μm. The emissivity of the coating has been determined in a study at University Duisburg-Essen, Chair of Use of Energy. Generally, the emissivity of the coating depends on the wavelength, temperature and also holding time, thus $\varepsilon(\lambda, T, t)$. For the TMF panel tests two wavelengths, $\lambda_{\mathrm{laser}} = 0.94$ μm and $\lambda_{\mathrm{IR}} = 3.99$ μm (see Section 3.2.3), at surface temperature levels of $T_{\mathrm{s}} = 600 \ldots 1000$ K (see Section 3.3) are of special interest. Time effects of the emissivity are well beyond the measurement uncertainty and not taken into account here. According to Figure

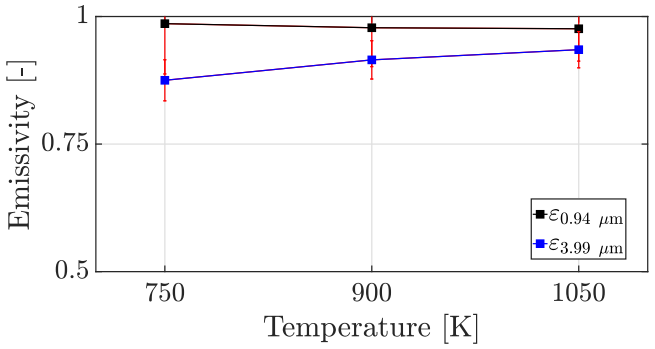

Figure 3.3: Emissivity of the applied coating for relevant wavelengths and temperature range as determined by University Duisburg-Essen, Chair of Use of Energy

3.3 the emissivity at the wavelength of the laser can be assumed to be constant for all relevant temperatures at $\varepsilon_{0.94\ \mu\mathrm{m}} = 0.98$ with small fluctuations much smaller than the measurement uncertainty. For $\lambda = 3.99$ μm the emissivity decreases slightly when the temperature decreases. The emissivity for $T < 750$ K is linearly extrapolated. The measurement uncertainty is, depending

on wavelength and temperature, between ±10.0% ($\lambda = 0.94$ μm, $T = 750$ K) to ±3.8% ($\lambda = 3.99$ μm, $T = 1050$ K). Onto the coating, a random pattern, called speckle marks, have to be applied to support the determination of the displacement with the stereo camera system (see Section 3.2.3). The speckle marks are made of aluminum oxide (Al_2O_3). They are sprayed onto the coating while the Al_2O_3 is dissolved in Ethanol (C_2H_6O). The speckle marks reduce the emissivity of the coating for both relevant wavelengths by an absolute value of $\Delta\varepsilon_{Al_2O_3} = -0.02$.

3.1.4 Material

Regeneratively cooled liquid rocket engines employ copper or copper alloys as the state-of-the-art materials of choice in the inner liner [5]. With special emphasis to their exceptional heat conductivity, these materials effectively transfer the heat generated during the combustion process to the fuel flowing through cooling channels. This maintains the temperature of the hot gas wall at relatively moderate levels below the melting point of the material. Prominent examples of commonly used alloys include *NARloy-Z* (CuAgZr), employed in American RS-68 and RS-25 engines [99] and the European Vulcain and Vulcain 2 [100]. CuCrZr is used in Japanese rocket engines [101], the Russian RD-0120 engine [102] among various research combustion chambers developed and tested at DLR Lampoldshausen [10, 103]. For upper stage engines like the European HM-7/HM-7B, Cu-OFHC is the material of choice [104]. For the fatigue life studies within this thesis Cu-HCP (CW021A) and CuCrZr were chosen.

Cu-HCP

While the available literature on the properties of Cu-HCP is limited, it is described as having excellent electrical and heat conductivity, impressive characteristics for both hot and cold formability, robust resistance against corrosion, and reliable welding and hard-soldering capabilities [105]. Cu-HCP exhibits diamagnetic properties and solidifies in a face-centered cubic lattice. Its common applications extend to electronics and electrical engineering. Also, it has been utilized in the investigation of GOX/GCH4 combustion chamber processes at the Technical University of Munich (TUM) [106]. From a range of potential materials, Cu-HCP was selected as a more cost-effective alternative to Cu-OFHC. It boasts good market availability and moderate production complexity. Furthermore, Cu-HCP displays minimal affinity for inclusions and cavities. However, its mechanical properties are notably influenced by the pro-

duction process and deformation history. Nonetheless, Cu-HCP stands as an enticing choice for the inner liners of forthcoming European rocket combustion chambers. The standardization of Cu-HCP is outlined in the norm DIN CEN/TS 13388:2020-09 [107]. The detailed composition of the material, as provided by the supplier Zollern, is presented in Table 3.4.

	Cu		**P**	**Bi**	**Pb**	**O_2**	**Other elements**
%	99.98	ppm	25.6	0.5	1.0	5.0	42.5

Table 3.4: Alloying elements of Cu-HCP according to test report and additional information provided by the supplier (see Appendix A). Other alloying elements include Ag, S, Ni, Fe, Zn, Mn, Sn, Sb, Te, Se, As, Cd in descending amount of portion.

The initial material underwent a process of hot forging through repeated compression and stretching. The source material had a diameter of $d = 410$ mm. Although the final material block sent to DLR measured $340 \times 340 \times 610$ mm, the individual stages of hot forging were not documented, preventing precise determination of the extent of deformation. Based on the polished micrograph section provided in the supplier's test report (see Appendix A), the processed material displayed a median grain size of $\bar{d}_\mathrm{g} = 190$ μm. Its hardness, measured on the Brinell scale [108], was 63 HBW 10/1000. The melting temperature of Cu-HCP stands at $T_\mathrm{m} = 1356$ K. In the production of both, the specimens used for material parameter determination and the TMF panels, three sections were cut from the delivered raw material block. Each slice had a thickness of approximately $t \approx 30$ mm. Ensuring consistent material parameters in terms of deformation, the slices were taken from three distinct outer surfaces of the block. Furthermore, care was taken to maintain a uniform orientation of the plates for all specimen and panels.

CuCrZr

The high-conductivity alloy CuCrZr (Copper-Chromium-Zirconium) possesses a moderate level of strength and is obtained as a cold-worked plate through rolling, known as *Elbrodur N*. It was supplied by KME. This particular copper alloy is typically utilized as an electrode material for welding purposes [109]. It is considered a cost-effective alternative when compared to other copper-based alloys, like *NARloy-Z*, previously utilized for inner liner materials in the SSME and Vulcain engines, as well as the Copper-Chromium-Niobium (CuCrNb) al-

loy *GRCop-84* chosen for application in the NASA Reusable Launch Vehicle program [110]. The chemical composition is denoted in Table 3.5. The CuCrZr

	Cu	**Cr**		**Zr**	**Ag**	**Fe**	**Al**	**Other elements**
%	99.425	0.5	ppm	540	50	30	10	121

Table 3.5: Alloying elements of CuCrZr according to Thiede [9]

alloy is furthermore extensively described by Thiede [9, 35] regarding the solubility of alloying elements and the respective microstructure. Therefore, readers shall be referred to the respective literature at this point for further reading.

3.2 TMF Panel Test Bench

The TMF panel test bench located at the DLR Institute of Space Propulsion in Lampoldshausen can be categorized into four distinct subsystems: the Diode Laser heating system, the fluid system, the measurement and control system, and the TMF panel test chamber, which serves as the central convergence point for all these subsystems. This section provides comprehensive descriptions of each of these subsystems. Figure 3.4 provides an overview of both the test room and the control room, highlighting the key components.

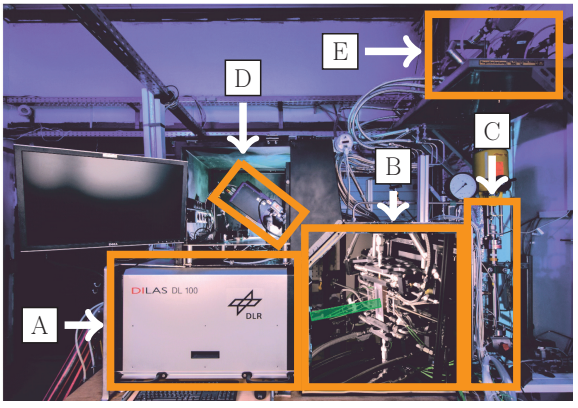

(a) View inside the TMF Test Room. A: Laser head, B: Test chamber, C: p, T-Sensors, D: IR camera, E: Coriolis flowmeter

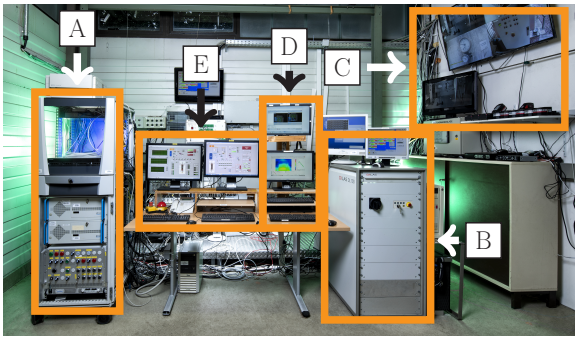

(b) View inside the TMF Control Room. A: Test bench control unit, B: Laser control rack, C: Camera surveillance screens, D: IR and stereo camera control, E: Measurement and control computer,

Figure 3.4: Display of the main infrastructure of the TMF panel test facility

3.2.1 Diode Laser DL100

The diode laser DILAS DL100 is the key component of the TMF panel test bench. This prototype system comprises three primary subsystems: the laser head, the control unit, and the cooling unit. The maximum optical power output is $P_{\text{out}} = 11$ kW at a wavelength of $\lambda = 940 \pm 10$ nm. The laser head is composed of five diode stacks, each containing 400 diodes, resulting in a total of 2000 diodes. To achieve precision, the focusing optics homogenize the laser beam into a top hat configuration with an accuracy level of ±5 % at the focal plane [111] (see Figure 3.6). Within the focal plane the top hat intensity reaches up to $\hat{I} = 28$ MW/m^2. The half width of the laser profile where the normalized intensity remains $I > 0.5$ can be determined to an area of $A_{\text{focal}} = 11.2$ mm $\times$ 32.2 mm. During operation the laser optics are continuously purged with gaseous nitrogen. The technical specifications of the laser system are summarized in Table 3.6. The laser output power exhibits a linear

Parameter	**Symbol**	
Laser wavelength	λ	940 ± 10 nm
Optical power output	P	11 kW
Focal plane size	A	11.2 mm $\times$ 32.2 mm
Focal distance	l	399 mm
Homogeneity		$< \pm 5\%$
Maximum intensity	$\hat{I}$	28 MW/m^2

Table 3.6: Technical data of DILAS diode laser

relationship with the diode supply current (I), which is itself remotely regulated through the control program by means of an output control voltage (U_{ctrl}). For simplification the function was set to $I \sim 10 \cdot U_{\text{ctrl}}$ for $U_{\text{ctrl}} = 1.1$ ... 6.0 V during initial programming of the measurement and control software in LABVIEW. Prior to the test campaigns a thorough assessment of the laser system was conducted. To ascertain crucial laser properties like focal distance, output power, and intensity distribution with respect to the variable U_{ctrl}, a PRIMES PowerMonitor PM DIODE (accuracy ±2%, reproducibility ±1%) and a PRIMES BeamMonitor BM100 (accuracy ±5%) were used. During the measurements the PRIMES BeamMonitor has been tilted by 5° mirroring the TMF panel tilt by 5° to prevent direct reflection of unabsorbed laser radiation from the panel back into the laser head. The determination of the distance of the focal plane from the laser beam exit plane involved measuring the intensity distribution at

various distances from the laser head (as shown in Fig. 3.5) while maintaining a control voltage of $U_{\text{ctrl}} = 5.6$ V. Subsequently the data was evaluated for the

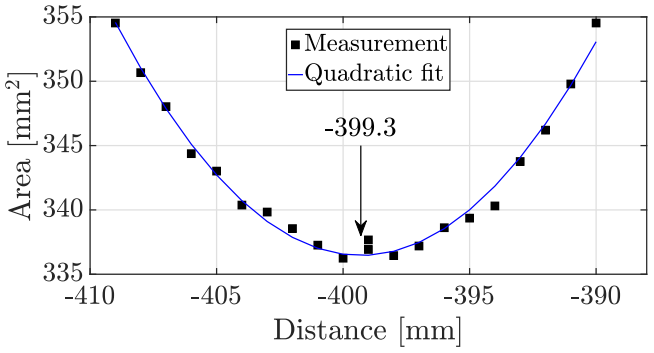

Figure 3.5: Area in which $1 - 1/e^2$ (86%) of the laser output power is included as a function of the distance to the laser head exit. The focus is determined at the smallest area including 86% of the laser output power at a control voltage of $U_{\text{ctrl}} = 5.6$ V.

least area in which $1 - 1/e^2$ ($\approx 86\%$) of the laser power is comprised defining it as the distance with the highest power density. According to the results presented in Figure 3.5 the focal distance is determined to $l_{\text{focus}} = 399.3$ mm. At this newly established focal distance, the optical output power was measured while varying U_{ctrl}. The resulting relationship, described by Equations (3.4) and (3.5), demonstrates a linear trend

$$P_{\text{out}} = 2198.58 \frac{\text{W}}{\text{V}} \, U_{\text{ctrl}} - 2698.83\text{W} \tag{3.4}$$

$$P_{\text{out}} = 2120.40 \frac{\text{W}}{\text{V}} \, U_{\text{ctrl}} - 2438.60\text{W} \tag{3.5}$$

for the relevant range of $U_{\text{ctrl}} = 1.1 \ldots 6.0$ V. It is important to note that between the first test campaign including the Heat Transfer Test (HTT) panel and the remaining test campaigns the laser system underwent major repair. As a consequence the relation $P(U_{\text{ctrl}})$ changed from Equation (3.4) to Equation (3.5). However, the focal distance and intensity distribution was not affected. For the fatigue life time analysis only the resulting average heat flux of the top hat into the TMF panel is of special interest. It can be determined by taking into account the optical power incident to the relevant top hat area with the emissivity coefficient ($\varepsilon_{940\ \text{nm}}$) of the TMF panel coating for the laser wavelength (see Section 3.1.3). The following equations show the resulting functions for the HTT panel test campaign (Equation (3.6)) and after repair (Equation (3.7)).

$$q = 5.80 U_{\text{ctrl}} - 6.54 \tag{3.6}$$

$$q = 5.45U_{\text{ctrl}} - 6.83 \tag{3.7}$$

A detailed distribution of the laser intensity for $U_{\text{ctrl}} = 5.7$ V is presented in Figure 3.6. It can be seen that the intensity of the laser is at its highest on the lower half of the profile (downstream) and slightly decreasing further upstream the axial direction (Z). (Fig. 3.6b). The homogeneity in tangential direction (Fig. 3.6c) is less varying.

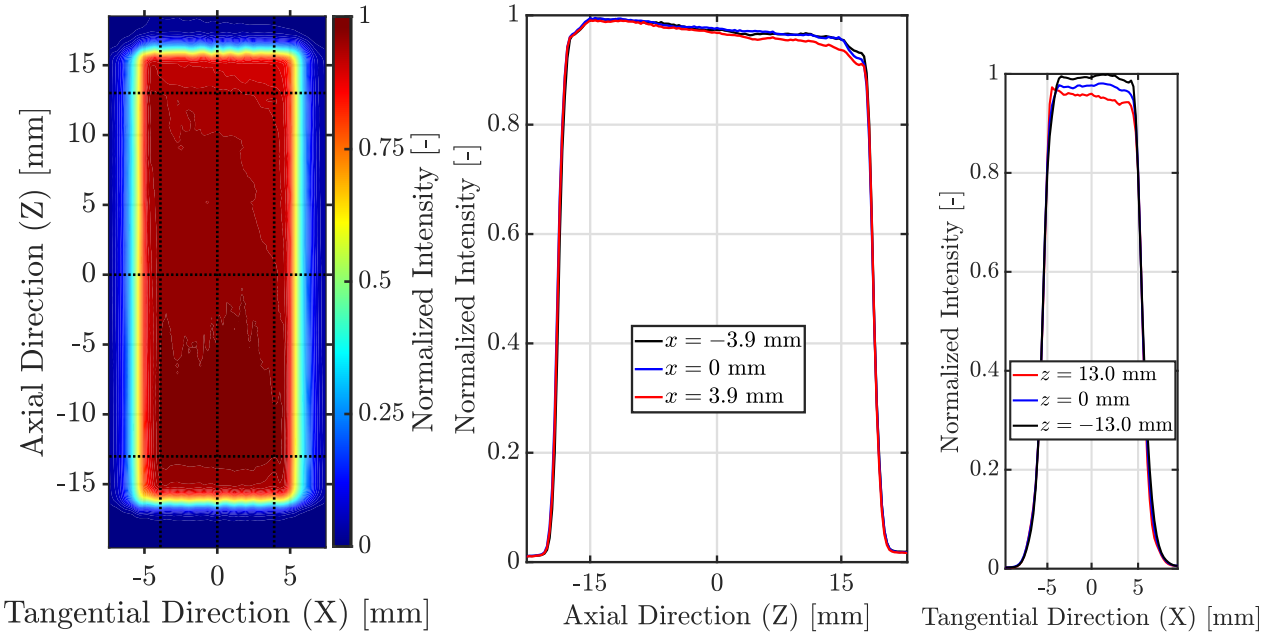

(a) Normalized laser top hat intensity at focal plane

(b) Cross section of the laser top hat in axial direction (Z) in three representative planes marked in Figure 3.6a

(c) Cross section of the laser top hat in tangential direction (X) in three representative planes marked in Figure 3.6a

Figure 3.6: Laser profile for $U_{\text{ctrl}} = 5.7$ V

3.2.2 Fluid System

The fluid system within the test bench serves as the source of essential nitrogen coolant for the TMF panel. This system is constructed using SWAGELOK pipes of various diameters. The coolant itself is a mixture of liquid nitrogen (LN_2, $p = 5$ bar $T = 94$ K) and gaseous nitrogen (GN_2, $p = 180$ bar, $T \approx 288$ K). Liquid nitrogen is stored in an external tank with a volume of $V_{LN_2} = 21$ m^3 and is delivered into the fluid system via a KRYTEM cryogenic reciprocating pump

[112]. To prevent oscillations in mass flow rates caused by the pump, it employs two vacuum-insulated piston pump heads. Additionally, significant pressure drops are implemented in the feed lines. The pump operates at a nominal pressure of $\hat{p} = 250$ bar with a stroke speed ranging from $f = 20 \ldots 300 \ \frac{1}{\text{min}^{-1}}$, resulting in a nominal capacity spanning $\dot{V} = 1.5 \ldots 21$ l/min or a mass flow rate between $\dot{m} = 0.020 \ldots 0.280$ kg/s. The gaseous nitrogen is sourced from the central supply at the DLR Institute of Space Propulsion. It is buffered by two tanks, each with a capacity of $V = 1$ m^3, to reduce pressure fluctuations in the central supply system. A dome pressure reducer is used to regulate the overall system pressure, and an electric control valve adjusts the GN_2 mass flow rate. Both components of the coolant, i.e. LN_2 and GN_2, are mixed before the supercritical fluid is split into the seven individual feed lines, each designated to a specific cooling channel. The mass flow rate for each cooling channel is independently regulated using a combination of a manual valve for coarse adjustments and an electronically controlled FLOWSERVE Kämmer Valve for remote fine-tuning. With this setup, the mass flow rate per cooling channel can be controlled with a deviation of only $\Delta\dot{m}_{\text{cc}} = \pm 0.2$ g/s from the desired value. The precise mass flow rate is subsequently measured using a Coriolis flow meter (see Section 3.2.3). The nitrogen coolant flows through both, the manual and control valves, at sonic speed conditions to decouple the mass flow rate from the pressure inside the TMF panel and further damp potential oscillations induced by the pump. The maximum achievable mass flow rate per cooling channel is $\hat{\dot{m}}_{\text{cc}} = 50$ g/s, the minimum mass flow rate is $\dot{m}_{\text{cc}} = 8$ g/s. Beyond the TMF panel, the coolant merges into a collector, facilitating effective control of the pressure across all cooling channels simultaneously using a single control valve at the outlet, based on the principle of communicating pipes. The nitrogen coolant is then dumped into the environment. For purging the TMF test chamber, gaseous nitrogen is sourced from a secondary feed line connected to the central supply. This nitrogen replaces the air, particularly oxygen and water, within the test cell to prevent high-temperature oxidation of the copper and coating, as well as the formation of ice on the TMF panel's surface. The fluid system is also equipped with several thermocouples and pressure sensors to monitor thermal and pressure conditions before entering the TMF panel. However, these details are of minor relevance to the test results and are therefore not described in detail here. Additionally, the system includes multiple mechanical release safety valves with a release pressure of $\hat{p} = 100$ bar and automated safety devices (red-lines), such as the automatic shutdown of the LN_2 pump, to ensure safe operation.

3.2.3 Measurement and Control System

Within this section the most important aspects of the measurement and control system regarding the experimental results are described. These are the infrared camera, stereocamera system, temperature, pressure and mass flow rate measurement as well as amplifiers and data acquisition devices.

Infrared camera

The surface temperature of the laser loaded section on the TMF panel is measured with a FLIR SC7600 infrared (IR) camera [113] equipped with an Indium-Antimony (InSb) detector with an F/3 aperture. The Noise Equivalent Temperature Difference (NETD) of the detector is specified < 25 mK. The full frame resolution is 640×512 pixels with a pixel pitch of 15 μm. The camera is equipped with a lens featuring a focal length of 100 mm and an F/2 aperture. At full frame resolution, a maximum frame rate of $\hat{f}_{\mathrm{IR}} = 100$ Hz can be achieved. In order to increase the dynamic range in the areas with high temperature gradients on the TMF panels surface the camera is capable of a "superframing" mode. In superframing mode up to 4 subframes with different integration times are composed into one measurement frame. However this reduces the temporal resolution by a factor of 4 so that $f_{\mathrm{IR,eff}} = 25$ Hz. For the present test setup a frame rate of $f_{\mathrm{IR}} = 4$ Hz (in superframing mode) is considered sufficient. The spectral range of the InSb detector covers wavelengths of $\lambda_{\mathrm{IR}} = 1.5$ ... 5.1 μm. Additionally the IR camera has an internal filter wheel allowing up to four filter settings. However, only one of the filter positions has an actual filter mounted which is used for measurements of $T = 573$ ... 1773 K. Wavelengths of $\lambda = 3.97$ ... 4.01 μm can pass this narrow band pass high temperature filter. Measurements in the temperature range of $T = 253$ ... 573 K do not use an internal filter. To prevent the directly reflected laser light irradiating from the TMF panel into the camera lens, influencing the accuracy of the temperature measurement, a high pass filter made of Germanium glass is mounted between the panel and the IR camera. It blocks all radiation below $\lambda_{\mathrm{hp}} < 2.5$ μm. The calibration of the camera is executed including the Germanium glass filter. The measurement accuracy of the IR camera is ± 1 K in the range $T = 278$ ... 373 K and ± 1 % for $T > 373$ K for black body radiation with $\varepsilon = 1.0$. For recording and evaluation of the measurement the software FLIR RESEARCH IR Version 4.40 is used.

Stereo-Camera-System

In order to obtain the deformation and derived from this the strain on the TMF panel laser heated surface area during a cycle as well as during the overall course of the test campaign, a LIMESS Q-400-2D [114] stereo camera system with digital image correlation (DIC) is available. The system uses two ALLIED VISION Prosilica GE 4900 [115] cameras mounted with an angular separation of about 90° and a distance of around 300 mm in front of the TMF panel. During the calibration process the exact relative position of the cameras with respect to each other is determined (extrinsic parameters) as well as the imaging parameters (intrinsic parameters), respectively. The cameras are equipped with a ON Semiconductor KAI-16000 CCD sensor. The sensors have a resolution of 4872×3248 px. The maximum frame rate at full resolution is $\hat{f}_{\text{LIMESS}} = 3$ Hz with an image bit depth of 12 bit in a monochrome pixel format. The acquisition rate during the TMF panel test was set to $f_{\text{LIMESS}} = 2$ Hz. Both cameras are equipped with a NIKON object lens with a magnification of 2.8x. To protect the sensors of the cameras from reflected laser light three SCHNEIDER-KREUZNACH B+W Infrared Cut Filter 489 are serially mounted in front of each lens. In combination with the digital image correlation software ISTRA 4D, Version 4.6 [116] together with the previously mentioned speckle marks (see Section 3.1.3), the three displacement components u_{x}, u_{y}, u_{z} on the 2-dimensional surface can be determined. The precision of the LIMESS measurement system relies on various factors, including the quality of calibration and the dimensions of speckle patterns. As a result, it cannot be universally quantified. It's worth noting that the Digital Image Correlation (DIC) method computes displacements and strains with respect to a reference plane.

Temperature measurement

The TMF panel is equipped with 23 thermocouples to adequately determine the temperature of the coolant fluid as well as on dedicated spots on the surface of the TMF panel. The inlet and outlet temperature of the fluid is measured for each cooling channel. Note that the temperature measurement takes place upstream and downstream of the TMF panel itself in the fluid line for constructive reasons. For example, the temperature sensors in the central cooling channel are separated with a distance of $d = 405$ mm from each other outside the actual TMF panel at the interface to the fluid supply system (see Fig. 3.1). Thermocouples of Type K (Class 1) made by ELECTRONIC SENSOR are used. The sensors are mounted with fittings to the SWAGELOK piping system to ensure that the core temperature in the center streamline of the fluid is measured

[117]. The tolerance of the Type K thermocouples is specified with ±1.5 K for $T = 233$ ... 375 K and ±0.4% of the measured value for $T = 375$ ... 1273 K. However, there is no tolerance for Type K thermocouples specified for the temperature range of the supercritical nitrogen coolant used here. Therefore a batch calibration was executed at Electronic Sensor with liquid nitrogen at its boiling point in ambient pressure ($T_B = 77.2$ K). The resulting deviation is $\Delta T = 1.35$ K. The surface temperature of the TMF panel is measured at 9 different spots as indicated in Figure 3.1. The sensors used here are Omega TJC2 Type K (Class 1) thermocouples [118]. The specifications are therefore similar to the sensors used for fluid measurement. The diameter of the thermocouples is $d = 0.50$ mm. The temperature sensors for the inlet fluid temperature of cooling channels 1-3 and 5-7 are connected to a NI DAQ system as they have been installed later. All remaining thermocouples are connected to an Isotech TRUrac Model 847 Thermocouple Reference Unit [119] with a specified stability of ±0.03 K around $T = 273.15$ K. By this means, the errors introduced by thermocouple loading are removed by adjusting the controller offset.

Pressure measurement

To determine the pressure inside the cooling channels of the TMF panel eight absolute and seven differential pressure sensors are available. The access holes for pressure measurement are located on the back side of the TMF panel (see Fig. 3.1). For constructive reasons the distance between the upstream (inlet) and downstream (outlet) access holes for cooling channels 2, 4 and 6 is $d_{2,4,6} = 105.26$ mm while for the remaining channels the distance is $d_{1,3,5,7} = 88.18$ mm. The absolute pressure is measured at the inlet of the central cooling channel and at the outlet of each cooling channel. Schaevitz P913-0003 sensors with a measurement range of $p = 0$ ... 100 bar are used. Their accuracy is specified with ±0.1% of the full scale (FS) [120]. For measurement of the differential pressure Honeywell KZ sensors are installed in cooling channels 1 and 3 - 6. Honeywell HL-Z sensors are used in cooling channels 2 and 7. The model Honeywell KZ has a measurement range up to $\Delta p = 2$ bar and is specified with an accuracy of ±0.25% FS. The Honeywell HL-Z sensors have a measurement range of $\Delta p = 10$ bar also with a specified accuracy of ±0.25% FS [121].

Mass Flow Measurement

For the accurate determination of the mass flow rate in the cooling channels, the TMF panel test bench is equipped with seven EMERSON Micro Motion CMF025H Coriolis flow meter [122], one for each cooling channel. The CMF025H is limited to a maximum mass flow rate (liquid) of $\hat{\dot{m}} = 605$ g/s with a specified accuracy of ±0.10% of the measured value.

Amplifier and Data Acquisition Devices

For the amplification of the signals generated by the thermocouples and the pressure sensors three different types of amplifiers are in use. For the first test campaign six pressure sensors (herein the inlet, outlet and differential pressure sensor of the central cooling channel) are each connected to a DEWETRON DAQP-STG [123] amplifier, all remaining sensors are connected to AS4 amplifiers [124] which were developed in-house at the DLR Institute of Space Propulsion. During all other test campaigns, all sensors were shifted to the DEWETRON DAQP-STG system increasing the accuracy. Additionally, the NI DAQ system was introduced. The specified accuracy of the measurements with this system is highly depending on the measured temperatures. For cryogenic temperatures of interest between $T = 160$ ... 273 K the measurement error exponentially decreases from ±2 K to ±1 K. Between $T = 273$ ... 350 K the measurement error is constant at ±1 K. The accuracy for the DEWETRON amplifiers is specified with ±0.05% while the accuracy of the AS4 amplifiers is $^{+0.2}_{-0.5}$% FS. The AS4 and DEWTRON amplifiers are connected to NATIONAL INSTRUMENTS (NI) data acquisition devices in two separate computers, whereof one is solely used for data recording and the other one serves as the test bench control unit (see Fig. 3.4b). The measurement PC is equipped with two NI 6031E and a NI 6733 data acquisition devices while the control PC uses three NI 6259 and a NI 6221 device. The NI devices have an accuracy between ±0.01% (NI 6031E [125]) and ±0.03% (NI 6221 [126]) also depending on the nominal input range of 0 ... 10 V.

3.3 Test Series Overview

For the experimental part of the research within this thesis 4 TMF panel test campaigns were conducted. While three tests were specifically dedicated to the fatigue life, the first test was intended to examine the heat transfer characteristics of the TMF panel made from Cu-HCP. The fatigue life tests comprised a

central point, a temperature variation and a material variation. An overview of the test conditions is given in Table 3.7. Furthermore, a comparison between

	Variation	$\boldsymbol{T}$ [K]	$\boldsymbol{q_w}$ [MW/m^2]	$\boldsymbol{t_{on}}$ [s]	**Material**
1	heat transfer	648 ... 1000	12.0 ... 24.6	200	Cu-HCP
2	central point	800	24.25	200	Cu-HCP
3	temperature	900	24.25	200	Cu-HCP
4	material	800	24.25	200	CuCrZr

Table 3.7: Overview of the test conditions

Condition	**LOX/LH2 engine**	**TMF panel**
Surface temperature of heat loaded wall	800 ... 1000 K	800 & 900K
Heat flux through heat loaded wall	40 MW/m^2	24.25 MW/m^2
Coolant	LH_2	LN_2
Temperature of coolant	21 K	160 K
Pressure of coolant	160 bar	55 ... 65 bar
Pressure in combustion chamber/ ambient pressure	100 bar	1 bar
Pressure difference heated wall $\leftrightarrow$ cooling channel	60 bar	54 ... 64 bar

Table 3.8: Comparison of conditions in a lowly loaded LOX/LH2 combustion chamber and TMF panels

the conditions of a LRE and the TMF panel tests is given in Table 3.8. Each TMF panel test campaign is defined by the following parameters:

- N_2 outlet pressure p_{out}
- N_2 inlet temperature T_{in}
- Maximum temperature of the laser loaded surface T_{s}
- Heat flux into the TMF panel q_{w}
- Laser-on time t_{on} (constant power, see Fig. 3.8)
- Mass flow rate per cooling channel $\dot{m}_{\text{cc}}$

To reduce the amount of variable parameters and make the individual TMF panel tests more comparable the outlet pressure of the N_2-coolant is always fixed and set to $p_{out} = 55 \pm 0.5$ bar at the start of a cycle but eventually rises to $p_{out} \approx 65$ bar at steady state conditions during heating. Hence, the resulting pressure difference between laser loaded surface and cooling channel is very close to the pressure difference between the hot gas and the coolant in a real LRE. The same applies to the coolant inlet temperature. It is always set to $T_{in} = 160 \pm 2$ K at the start of a cycle. Thus, the coolant fluid is at supercritical conditions (see Fig. 3.7). The inlet temperature and outlet pressure are chosen in order to have a significant "distance" to the Widom line as can be seen in Figure 3.7. This prevents any unintended rapid changes in the fluid properties

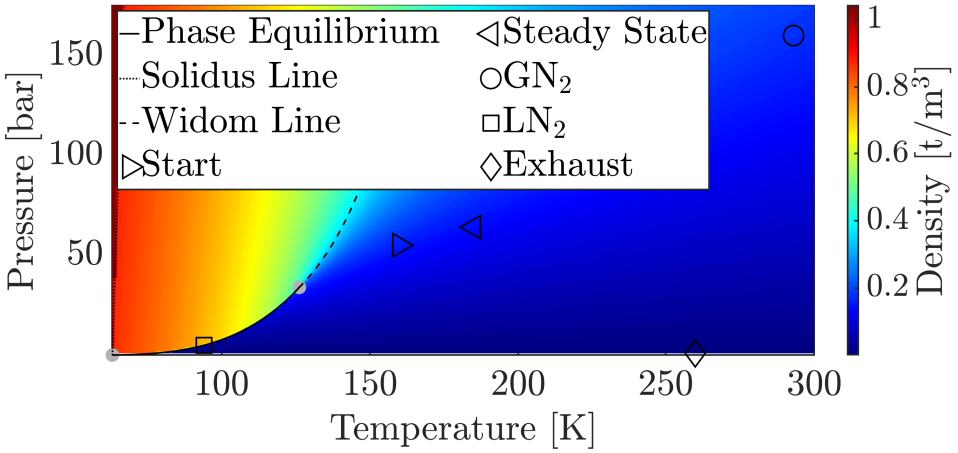

Figure 3.7: Phase diagram of N_2 including the fluid conditions at significant stages in the test procedure.

which occur around the critical point [127]. The Widom line in Figure 3.7 is calculated according to Banuti [128]. The heat flux into the TMF panel is also kept constant at $q_w = 24.25$ MW/m^2. The value is chosen due to limitations of the laser system (see Section 3.2.1). Furthermore, the laser sequence is similar for each test campaign within the framework of this thesis. This mainly arises from heritage of previous test campaigns that were intended to simulate the burn time of liquid rocket engine core stages or booster stages [7, 29, 35]. The laser sequence is on display in Figure 3.8. The time of constant laser power and hence constant heat flux is $t_{on} = 200$ s framed by a ramp up of $t_{up} = 30$ s and a ramp down of also $t_{down} = 30$ s. This leaves the surface temperature T_s as the sole variable parameter. However, since p_{out} and T_{in} are fixed, the remaining parameters T_s, q_w and $\dot{m}$ highly depend on each other to achieve the desired test conditions. In order to identify their dependencies, i.e. the dependency of

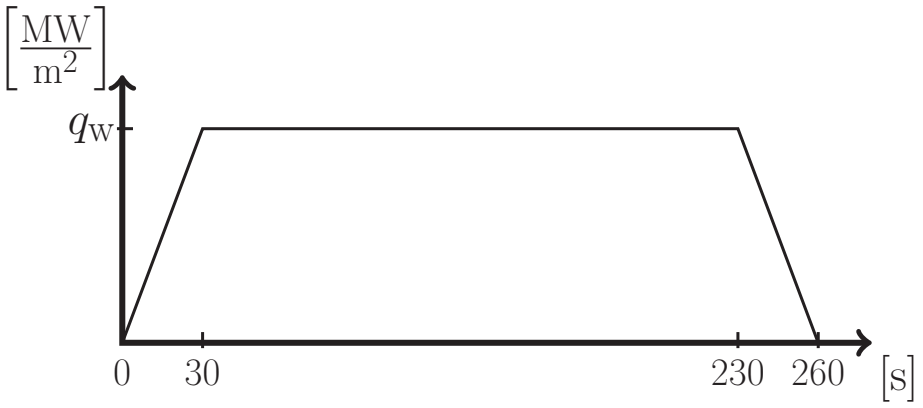

Figure 3.8: Qualitative profile of the laser-on cycle consisting of linear ramp-up over 30 s, constant power and resulting constant heat flux rate for $t_{on} = 200$ s and linear ramp-down over 30 s

the surface temperature on coolant mass flow rate and heat flux [38], the Heat Transfer Test (HTT) panel experiment was conducted.

3.3.1 HTT Panel Test

As described by Thiede [9] and Kringe [10] the mass flow rate per cooling channel is typically determined experimentally by an iterative approach within the first 4 - 6 cycles at the beginning of each TMF panel test. This causes the surface temperature and heat flux to be lower than intended as a conservative approach is chosen to not overheat the panel locally. The objective of the HTT panel was to generate a reliable database for the dependency of the three parameters T_s, q_w and $\dot{m}$ and afterwards validating a numerical simulation for the fluid flow, heat transfer characteristics and temperature distribution of the TMF panels made of Cu-HCP (see Section 5.1). The test setup used the same panel geometry as described in Section 3.1.1. For the single cycles in the test campaign four different surface temperatures between $T_s = [648,\ 763,\ 886,\ 1000]$ K were investigated. Accordingly, the heat flux was varied between $q_w = 12.0$ ... 24.6 MW/m^2.

3.3.2 Central Point

In the central point (CP) TMF panel test campaign the test conditions were chosen close to the operational point of a lowly loaded upper stage engine. It also serves as a reference for the conditions of the following test campaigns. The maximum surface temperature was set to $T_s = 800$ K. From the results

of the HTT panel test campaign the initial mass flow rate per cooling channel was interpolated to $\dot{m}_{\mathrm{cc}} = 40.4$ g/s (see Fig. 5.1a).

3.3.3 Temperature Variation

For the temperature variation (TV) test campaign the maximum surface temperature was increased by $\Delta T_{\mathrm{s}} = 100$ K to $T_{\mathrm{s}} = 900$ K while all other parameters except the mass flow rate were kept constant. The intention of this variation was to determine the influence of a higher temperature on the fatigue life of the TMF panel. From LCF tests it could be seen, that the ductility of the material increases significantly at $T = 900$ K. From the results of the HTT panel test campaign the initial mass flow rate per cooling channel was interpolated to $\dot{m}_{\mathrm{cc}} = 31.1$ g/s (see Fig. 5.1a).

3.3.4 Material Variation

In the material variation (MV) test campaign similar conditions as in the central point were applied. However, as the material was changed to CuCrZr, the mass flow rate had to be adjusted. For CuCrZr no data similar to HTT panel test campaign was available. Hence, the mass flow rate had to be determined iteratively with some initial values obtained from the results of a previous test campaign conducted by Kringe [10] for $T_{\mathrm{s}} = 1000$ K as well as the conditions calculated by Thiede [9].

4 Numerical Setup

In this chapter the Numerical Setup is described in detail. This includes the parameter identification for the simulations in ANSYS Mechanical as well as for the damage post-processing in MATLAB. Furthermore, the setup of the simulations in ANSYS CFX and Mechanical is described including the boundary conditions and analysis options.

4.1 Material Parameter Identification

This section presents the identification of mechanical and thermophysical material parameters. In the frame of this thesis a material parameter identification was executed for Cu-HCP for the use with the default material models available in ANSYS Mechanical ("Standard ANSYS Mechanical"). The material parameters for Cu-HCP in combination with the UPF where provided in the framework of the respective project. They were all developed from the same uniaxial data set by Prof. Thomas SEIFERT [58, 62, 63]. The material parameters for CuCrZr in combination with the default material models in ANSYS Mechanical were determined by RICCIUS ET AL. [11] from the same data set used by THIEDE [34] and MASUOKA [65]. The material parameter set used with the UPF for CuCrZr was published by MASUOKA [65]. The thermophysical parameters used were measured by FRAUNHOFER IWM for Cu-HCP and CuCrZr.

4.1.1 Mechanical Parameters

The material models incorporate temperature-dependent material properties, which are established through empirical algorithms. Typically, uniaxial tests are employed, conducted under service-relevant loading conditions encompassing factors like strain amplitudes, strain rates, and temperature levels. For deriving material properties for plasticity models complex low-cycle fatigue (CLCF) tests are preferred. These tests are well-suited because they involve a loading history that activates all phenomena describable by plasticity models, including hardening, relaxation, ratcheting, and time dependency. Also, the determination of material parameters is presented for Cu-HCP.

Material Test Overview and Setup

This section gives an overview of the uniaxial test data available for the identification of material parameters. Table 4.1 displays an overview of all tests conducted and shows the specific temperatures and strain rates. The uniaxial tests featuring $T > 273$ K have been performed at Fraunhofer IWM, the material tests for cryogenic temperatures were conducted at Testia GmbH.

A graphical impression of the tensile tests is given in Figure 4.1b including

Table 4.1: Overview of uniaxial tests conducted for material parameter identification

	LCF				**Tensile**	
	Strain Amplitude [%]					
T [K]	**0.5**	**1**	**2**	**other.**		**ITT**
77	x	x				x
300	x	x		2.5, 3	x	x
500	x		x	1.75		x
700	x	x	x		x	x
800	x	x	x			x
900	x	x				x
1000	x	x	x		x	x

interrupted tensile tests (ITT) and normal tensile tests for comparison. The CLCF tests included a complex pre-program that is shown in Figure 4.1a. The stress response of the complex strain loading program is displayed for a maximum strain amplitude of $\varepsilon = 0.5$ % for all available temperatures. For all tests, the strain ratio is $R_\varepsilon = -1$. Clearly a rapid decrease of the stress can be observed at $T > 500$ K. The complex pre-program consists of three dwell sections with a holding time of $t_{\text{hold}} = 1000$ s, followed by a series of strain rate variation between $\dot{\varepsilon} = 0.1$ ... 0.001 $\frac{\%}{\text{s}}$. After the pre-program, each specimen was cyclically test to failure with a strain rate of $\dot{\varepsilon} = 0.1$ %.

Chaboche and Voce

The Chaboche and Voce parameters were estimated from the first to 10^{th} cycles subsequent to the complex pre-program of the CLCF tests. The open-source tool *RESSPyLab* [129] was used for optimization of the manually obtained starting values. *RESSPyLab* was developed by de Castro e Sousa [130] in Python. To minimize the error a Newton trust region (NTR) is utilized. The NTR is defined by the accumulated true strain and the true stress.

This approach for solving the inverse problem is notably more robust compared to generic algorithms and particle swarm optimization methods [130]. This approach has successfully been implemented for the determination of the combined CHABOCHE and VOCE model parameters for various types of structural steel [130], for low cycle fatigue conditions of a base material and the heat-affected zone of welded S690 QL high-strength steel [131]. The starting values for the CHABOCHE parameters [132] that are fed into *RESSPyLab* were determined following the approaches described by IMAOKA [133], ASRAFF [134] and SRNEC NOVAK [135]. This approach calculates a backstress component α_i (Equation 2.6) for each significant segment of the cyclic test i.e. three components with the parameters C_{1-3} and γ_{1-3} are determined. The parameters are obtained from the relation between $\varepsilon^{\mathrm{pl}}_{\mathrm{true}}$ and σ_{true} (see Equations (2.1),(2.2)). The plastic strain is calculated by

$$\varepsilon^{\mathrm{pl}} = \varepsilon - \frac{\sigma}{E}. \tag{4.1}$$

These significant segments refer firstly to the initial phase of the yielding characterized by a strong increase of stress α_1, secondly the rapid decrease of the slope of stress α_2, and thirdly the low linear increase of stress at the end of the hysteresis loop α_3 (see Figure 4.2). γ_3 is set to $\gamma_3 = 0$, therefore C_3 can be determined as the slope of the linear part of the hysteresis loop. Accordingly, the parameters C_1 and C_2 are the slopes of their respective segments of the hysteresis loop. As IMAOKA [133] states, a value for the relation C_1/γ_1 is represented by the asymptote when plotting $\Delta\sigma/2 - \sigma_0$ over $\Delta\varepsilon^{\mathrm{pl}}/2$. With C_1 already obtained, γ_1 can be determined. This leaves γ_2 as the only unknown parameter. It is calculated by solving Equation (2.5). Generally, $C_1 > C_2 > C_3$ and $\gamma_1 > \gamma_2 > \gamma_3$ should be respected [133]. There is no necessity to estimate start values for the VOCE parameters as this did not affect the results obtained by *RESSPyLab*.

Creep (Norton)

Creep is a form of material non-linearity characterized by its rate-dependent behavior, where the material continues to deform under a constant load. It is associated with $T > 0.5\,T_{\mathrm{m}}$. Conversely, when a displacement is applied, the reaction force (and stresses) decrease with time, a phenomenon known as stress relaxation. In the present model, creep modeling is used to cover creep and stress relaxation during the time of constant laser load. In the material model options of ANSYS Mechanical NORTON's original creep model [51] for

the creep strain rate $\dot{\varepsilon}^{\mathrm{cr}}$ is extended by an ARRHENIUS-type equation to cover the temperature dependency of creep.

$$\dot{\varepsilon}^{\mathrm{cr}} = A\sigma^n \qquad \xrightarrow[f(T)=\exp(-Q/RT)]{\text{ARRHENIUS}} \qquad \dot{\varepsilon}^{\mathrm{cr}} = C_1\sigma^{C_2}e^{-C_3/T} \tag{4.2}$$

The constants C_{1-3} are the creep constants. C_2 is the creep exponent and C_3 summarizes the activation energy Q and the ideal gas constant R. The creep constants were determined from the three dwell sections of the CLCF tests. From Figure 4.1a it can be seen, that the available test data had to be chosen carefully, as some nonphysical behavior like increase of stress during constant loading is observed. Hence, the creep constants could only be determined for $T \in [700, 800, 900]$ K. The test data yields a time-dependent progress of stress that follows the power law

$$\sigma = ht^k. \tag{4.3}$$

The general composition of strain

$$\varepsilon_{\mathrm{tot}} = \varepsilon^{\mathrm{el}} + \varepsilon^{\mathrm{pl}} + \varepsilon^{\mathrm{cr}} \tag{4.4}$$

including total strain $\varepsilon_{\mathrm{tot}}$, elastic strain $\varepsilon^{\mathrm{el}}$, plastic strain $\varepsilon^{\mathrm{pl}}$ and the creep strain $\varepsilon^{\mathrm{cr}}$ can be derived assuming that $\varepsilon_{\mathrm{tot}}$ and $\varepsilon^{\mathrm{pl}}$ are constant. This yields $-\dot{\varepsilon}^{el} = \dot{\varepsilon}^{cr}$. Inserting the derivative of Hook's Law and the derivative of Equation (4.3) into the logarithm of Equation (4.2)

$$\ln\left(-\frac{\partial\sigma/\partial t}{E}\right) = \ln\left(C_1^*\right) + C_2\ln\left(\sigma\right) \tag{4.5}$$

is obtained where $C_1^* = C_1 e^{-C_3/T}$. The constant C_2 is the slope of the straight line when Equation (4.5) is plotted in the $\ln(\sigma) - \ln(\dot{\varepsilon})$ −space. The same procedure is repeated for determination of C_1^*. Eventually, a creep surface can be determined in the $\ln(\sigma) - \ln(T) - \ln\left(\dot{\varepsilon^{\mathrm{cr}}}\right)$ −space as shown in Figure 4.3. Note that the experimental data is of limited extend. All extrapolated values outside the boundaries of the uniaxial CLCF tests have to be treated carefully. The orders of magnitude of the extrapolated creep strain rate values shown in Figure 4.3 are within reasonable range and therefore suitable for future usage.

Strain-Rate Dependency (Peirce)

To cover the rate-dependent plasticity the TMF panel experiences during different stages of a cycle, the PEIRCE [50] option is chosen. It shows better

convergence then the PERZYNA option [53, 136]. Rearranging Equation (4.6), the strain rate dependency after PEIRCE is calculated by

$$\dot{\varepsilon}^{\mathrm{pl}} = \gamma \left[\left(\frac{\sigma}{\sigma_0} \right)^{1/m} - 1 \right] \tag{4.6}$$

where σ is the strain rate dependent yield stress, $\dot{\varepsilon}^{\mathrm{pl}}$ is the equivalent plastic strain rate, γ denotes the viscosity parameter, m is the strain rate dependent hardening parameter and σ_0 the static yield stress. The PEIRCE model includes a yield surface and therefore is only present when the yield limit is exceeded. The experimental data for the determination of the parameters follows the dwell section in the uniaxial CLCF tests. It covers strain rates of $\dot{\varepsilon} \in [0.1, 0.01, 0.001]\ \frac{\%}{\mathrm{s}}$. Again, the experimental data has to be checked carefully to avoid nonphysical performance in the data set. Only two tensile loading branches per strain rate are usable. For parameter estimation calculating the quotient of two different strain rates at the same temperature eliminates the static yield stress. The resulting equations (two per temperature) can then be solved for the parameters γ and m.

Ductile Damage (Bonora)

The ductile damage parameters for the model introduced by BONORA [75] (see Equation (2.31)) are obtained from the interrupted tensile tests (see Figure 4.1b). Recalling Equation (2.22), the progress of the Young's Modulus can be determined in the elastic interruptions and yields the damage variable D. The damage variable is displayed in Figure 4.4a. It is obvious that the data includes a high scatter for all temperatures except $T = 77$ K. Additionally, in Figure 4.1b it can be seen that for example for the curve of $T = 300$ K the interruptions stop around $\varepsilon_{\mathrm{eng}} \approx 0.3$. For $T = 500$ K and $T = 77$ K the experimental data suddenly stops, so that the progress of the test is unknown. Therefore the available data had to be extrapolated with caution. The detailed process of parameter identification is described precisely by BONORA [75, 78, 137]. Following these instructions, the critical damage D_{cr} and the critical strain $\varepsilon_{\mathrm{cr}}$ can partially be extracted from Figure 4.4a. Alternatively, the critical damage was determined by measuring the remaining cross section of the tested specimen with the KEYENCE VHX5000 and applying the relation

$$D_{\mathrm{cr}} = 1 - \frac{A_{\mathrm{cr}}}{A_0} \tag{4.7}$$

with A_0 being the initial cross section area. Note that this approach does not cover the reduced cross section caused by voids laying inside the remaining cross section. The critical strain can also be obtained by detailed measurement of the length of the ruptured specimen and the definition of critical strain

$$\varepsilon_{\mathrm{cr,eng}} = \frac{l_{\mathrm{cr}} - l_0}{l_0} \tag{4.8}$$

with l_0 being the initial length of the tensile specimen. Note that Equation (2.2) was applied as well. After D_{cr} and $\varepsilon_{\mathrm{cr}}$ have been estimated, the damage exponent α could be determined by rearranging Equation (2.31) to

$$\ln\left(\frac{D_{\mathrm{cr}} - D}{D_{\mathrm{cr}} - D_0}\right) = \alpha \ln\left[\ln\left(\frac{\varepsilon_{\mathrm{cr}}}{\varepsilon}\right)\right] - C \tag{4.9}$$

where C is

$$C = \alpha \ln\left[\ln\left(\frac{\varepsilon_{\mathrm{cr}}}{\varepsilon_{\mathrm{th}}}\right)\right]. \tag{4.10}$$

α is defined as the slope of the experimental damage variable. For this purpose a linear best-fit line was calculated. The parameter C is obtained by the intersection of the best-fit line with the ordinate axis. Subsequently, $\varepsilon_{\mathrm{th}}$ is estimated by

$$\varepsilon_{\mathrm{th}} = \varepsilon_{\mathrm{cr}} \exp\left[-\exp\left(\frac{C}{\alpha}\right)\right] \tag{4.11}$$

The full set of parameters is given in Table 4.2.

Brittle Damage (Lemaitre)

The fatigue damage parameters are determined from the damage variable obtained in the CLCF tests [66, 69]. For every available cycle the Young's Modulus is determined. The progress of the damage variable is shown in Figure 4.4b. Unfortunately, the available data set for the CLCF tests for $T > 273$ K was filtered in order to reduce the amount of data. A logarithmic filter with respect to time was applied so that all cycles at the beginning of a test are available but the number of usable cycles decreases with the progress of time (see Appendix B). Due to the missing data, the plots in Figure 4.4b show several kinks and jumps with varying slopes. Additionally, a rapid decrease of the Young's Modulus at the end of each CLCF test could only be observed for $T = 77$ K (see Appendix B). However, as the results will demonstrate (see Chapter 5), the damage progress in the TMF panel is dominated by the ductile

damage and therefore only the portion of the damage variable shown in Figure 4.4b is of interest. This relevant section can be described by a linear function, so that Equation (2.24) can be reduced to

$$\dot{D}_{\mathrm{f}} = -\frac{Y}{S_1}\dot{p} \tag{4.12}$$

as $S_2 = 1$. Subsequently, the strain energy release rate Y can be determined using the CLCF test data. Note that for the uniaxial test $\sigma_{\mathrm{m}} = \sigma_{\mathrm{eq}}$. Equation (4.12) can then be solved for S_1. The results are listed in Table 4.2.

	Ductile				**Brittle**
$\boldsymbol{T}$ **[K]**	$\boldsymbol{\varepsilon_{\mathrm{cr}}}$	$\boldsymbol{D_{\mathrm{cr}}}$	$\boldsymbol{\alpha}$	$\boldsymbol{\varepsilon_{\mathrm{th}}}$	$\boldsymbol{S_1}$
77	0.5264	0.8386	0.3118	0.4320	197.5219
300	0.4506	0.8500	0.2769	0.3696	54.1110
500	0.4000	0.8000	0.2487	0.3395	18.6498
700	0.3802	0.7550	0.1857	0.3454	1.9283
800	0.3559	0.7530	0.2806	0.2303	0.6387
900	0.3500	0.7000	0.3755	0.2530	0.2934
1000	0.3200	0.6890	0.3755	0.1803	0.0846

Table 4.2: Damage Parameters

4.1.2 Thermophysical Parameters

The material of the inner liner of a combustion chamber experiences wide ranges of temperatures, typically between $T = 35$ K and $T = 1000$ K when fueled with liquid hydrogen. Because of the supercritical nitrogen coolant of the TMF panel the temperature range for the material is $T = 160$ ... 900 K. Within this extent of temperature the relevant thermophysical properties (specific heat capacity c_{p}, coefficient of linear thermal expansion $\bar{\alpha}$, density ρ, heat conductivity λ) of Cu-HCP and CuCrZr cannot be considered as constant any more. They show an intense dependency on the temperature. Particularly for low temperatures strong variations are observable. Therefore the thermophysical properties of Cu-HCP in the range of $T = 293$ ... 1273 K were experimentally determined by the Fraunhofer Institute for Mechanics of Materials (IWM). Two specimens were used and the arithmetic mean value was calculated. In particular, the specific heat capacity c_{p}, thermal expansion $\Delta l/l_0$, and thermal diffusivity α have been measured. In the extent of $T = 160$ ... 293 K the thermophysical

properties of Cu-HCP have been adapted from the work of Oschwald [138], Johnson [139], Simon [140] and Hust [141]. The thermophysical properties of CuCrZr have been published by Thiede [9] and are taken from this reference. These parameters also have been determined by the Fraunhofer Institute for Mechanics of Materials (IWM) using the same equipment. Tables 4.3 and 4.4 as well as Figures 4.5a and 4.5b provide the respective results. The individual thermophysical properties and the experimental and theoretical methods used for their determination are described in the following sections.

Specific Heat Capacity

The specific heat capacity c_p (at constant pressure) represents the amount of energy stored in a medium and solids. The energy is stored by the excitation of lattice vibrations. At low temperatures modes which require a high excitation energy can not be excited by the available thermal energy, whereas all lattice vibration modes are excited at sufficiently high temperatures. A detailed explanation of the underlying fundamental quantum mechanics can be found in Kittel [142] and Ashcroft [143]. The specific heat capacity was determined experimentally using a Netzsch DSC 404 F1 Pegasus [144] differential scanning calorimeter (DSC) applying the standard DIN 51007 [145]. For the application of this method a sample and a reference object are exposed to a controlled temperature program. The temperature of the sample and the difference in temperature between the reference object and sample are measured. Therewith the heat flow and hence heat capacity can be determined.
For the cryogenic temperature range the value for the specific heat capacity has been adapted from the work of Oschwald [138] using the Debye-Method [143]. It has been compared with the data available from Simon [140], Incropera [80] and NIST [146] showing a good congruence.

Thermal Expansion

The thermal expansion of a metal is a result of the anharmonic interaction potential between lattice atoms, i.e. the oscillation of the atoms around their equilibrium position is asymmetrical [143]. By using thermo-dilatometry in the thermomechanical analyzer (TMA) Netzsch TMA 402 F3 Hyperion [147] the temperature dependent length variation $\Delta l/l_0$ and thereof the coefficient of linear thermal expansion $\bar{\alpha}$ can be determined. According to DIN 51045 [148]

the technical (mean) thermal expansion coefficient is defined as

$$\bar{\alpha}\,(T) = \frac{1}{l_0}\frac{l(T) - l(T_0)}{T - T_0} = \frac{\Delta l}{l_0 \Delta T} \tag{4.13}$$

The mean (average) coefficient of linear thermal expansion is defined as the slope of a secant through two points of the curve of thermal expansion. It is the main driver of thermal strains within the TMF panel. The laser loaded surface experiences a large thermal expansion due to high temperatures. The temperature decreases closer to the cooling channel (negative y-direction), hence experiencing smaller thermal expansion or even contraction.
The reference temperature for the thermal expansion coefficient was set to $T_{\mathrm{ref}} = 293$ K. Thus a comparison with data from the literature could not be performed. Additionally, the thermal expansion coefficient for $T = 160$ K had to be extrapolated. This was done numerically in MATLAB with a 4^{th}-order *polyfit*. The density ρ is also calculated by using the measured data for $\Delta l / l_0$ according to

$$\rho(T) = \rho_0 \left(1 + \frac{\Delta l(T)}{l_0}\right)^{-3} \tag{4.14}$$

where $\rho_0 = 8.890$ kg m^3 is the density at reference temperature. The density for $T = 160$ K was also extrapolated using a 3^{rd}-order *polyfit* in MATLAB. Note that the density is of minor interest for the numerical calculations since $\bar{\alpha}$ is known, though noted here for the sake of completeness.

Thermal Diffusivity

The thermal diffusivity is a composition of thermophysical parameters which appears in the heat equation (see Equations (2.35) and (2.36)). It represents the ratio of thermal conductivity to the potential of heat storage of a solid material [81]. The thermal diffusivity was measured by laser flash analysis (LFA) with a NETZSCH LFA 427 [149] according to ASTM E1461 [150]. In this technique a thin sample is heated to a predetermined temperature. Then a pulsed laser beam is applied on one side of the sample, inducing a homogeneous heating. The temperature rise on the rear surface is measured and the thermal diffusivity can be determined by

$$\alpha = 0.1388 \frac{l^2}{t_{0.5}} \tag{4.15}$$

with l^2 being the thickness of the sample and $t_{0.5}$ the time at a temperature increase of 50%. The thermal diffusivity is not directly relevant for the analysis

of the TMF panel thus not listed in Table 4.3 but the thermal conductivity is derived from it as noted in the following section.

Thermal Conductivity

Since the heat capacity c_p, the density ρ and the thermal diffusivity α were experimentally determined, the thermal conductivity λ was calculated using Equation (2.36). For cryogenic temperatures a wealth of reference data is available in the literature. The value for λ at $T = 160$ K in Table 4.3 is comprised of the work from Oschwald [138], Incropera [80] and Hust [141].

T [K]	$\boldsymbol{c_p}$ $\left[\frac{\text{kJ}}{\text{kgK}}\right]$	$\boldsymbol{\bar{\alpha}}$ $\left[\frac{10^{-6}}{\text{K}}\right]$	$\boldsymbol{\rho}$ $\left[\frac{\text{t}}{\text{m}^3}\right]$	$\boldsymbol{\lambda}$ $\left[\frac{\text{W}}{\text{mK}}\right]$
160	0.332	-4.2	8.93	415.0
293	0.419	7.1	8.89	397.7
373	0.429	11.3	8.87	388.1
473	0.445	14.5	8.82	390.6
573	0.451	15.7	8.78	378.5
673	0.457	16.5	8.73	371.6
773	0.460	17.2	8.68	361.8
873	0.461	17.8	8.62	351.0
973	0.468	18.5	8.56	342.0
1073	0.477	19.0	8.51	335.5
1173	0.487	19.4	8.45	338.4
1273	0.499	19.8	8.39	363.1

Table 4.3: Thermophysical properties of Cu-HCP. Black: Determined by Fraunhofer IWM. Red: extrapolated Data. Blue: taken from Literature.

As seen in Figure 4.5, CuCrZr exhibits an approximately 20% lower heat conductivity λ that additionally rapidly decreases for $T > 700$ K. The coefficient of thermal expansion $\bar{\alpha}$ is slightly higher by about 5% at a temperature of $T = 800$ K for CuCrZr. Notably, when examining Cu-HCP, there is a substantial decrease in the coefficient of thermal expansion at lower temperatures, whereas it remains relatively constant for CuCrZr. This distinction is a crucial factor differentiating the fatigue life behavior of these two materials as Cu-HCP is subject to a higher gradient of thermal expansion in the heat-up or cool-down phase of the TMF panel test.

$\mathbf{T}$ [K]	$\boldsymbol{c_p}$ $\left[\frac{\mathrm{kJ}}{\mathrm{kgK}}\right]$	$\bar{\boldsymbol{\alpha}}$ $\left[\frac{10^{-6}}{\mathrm{K}}\right]$	$\boldsymbol{\rho}$ $\left[\frac{\mathrm{t}}{\mathrm{m}^3}\right]$	$\boldsymbol{\lambda}$ $\left[\frac{\mathrm{W}}{\mathrm{mK}}\right]$
0	0.432	16.7	8.94	302.24
160	0.428	16.8	8.87	302.24
300	0.424	16.8	8.81	300.96
500	0.419	17.1	8.72	301.34
600	0.416	17.4	8.67	299.71
700	0.413	17.7	8.63	295.16
800	0.411	18.0	8.58	286.44
900	0.408	18.3	8.53	272.26
1000	0.405	18.7	8.47	251.37
1300	0.397	19.5	8.31	135.64

Table 4.4: Thermophysical properties of CuCrZr as published by Thiede [9]

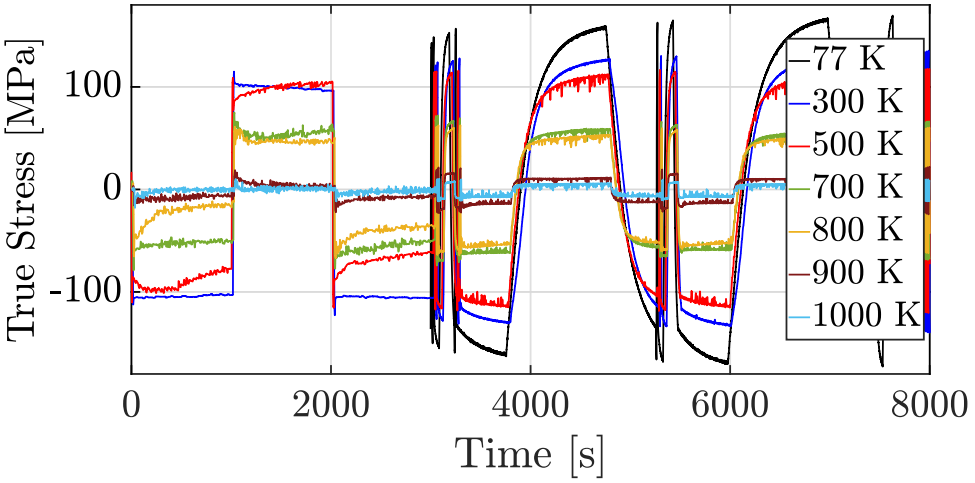

(a) Overview of the complex pre-program exemplary with $\varepsilon = 0.5\%$ for the determination of material parameters of Cu-HCP

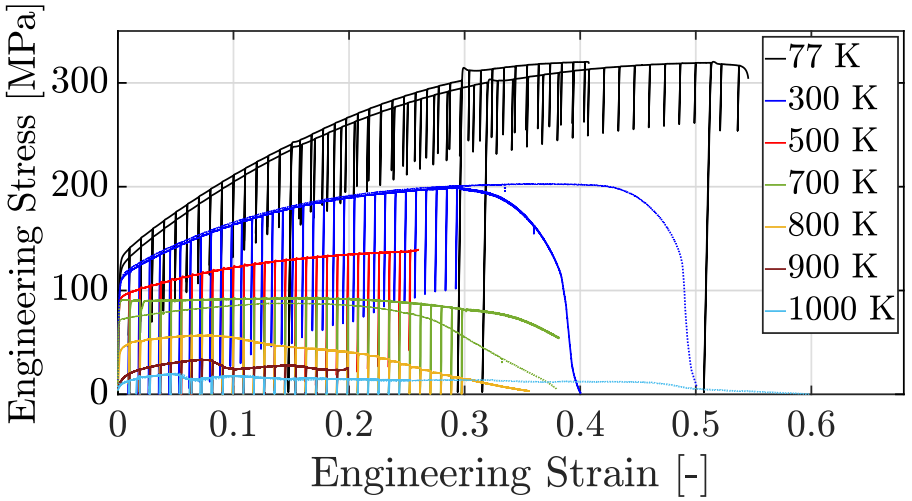

(b) Overview of all tensile tests performed for ductile damage parameter evaluation

Figure 4.1: Overview of all tests performed for material parameter determination

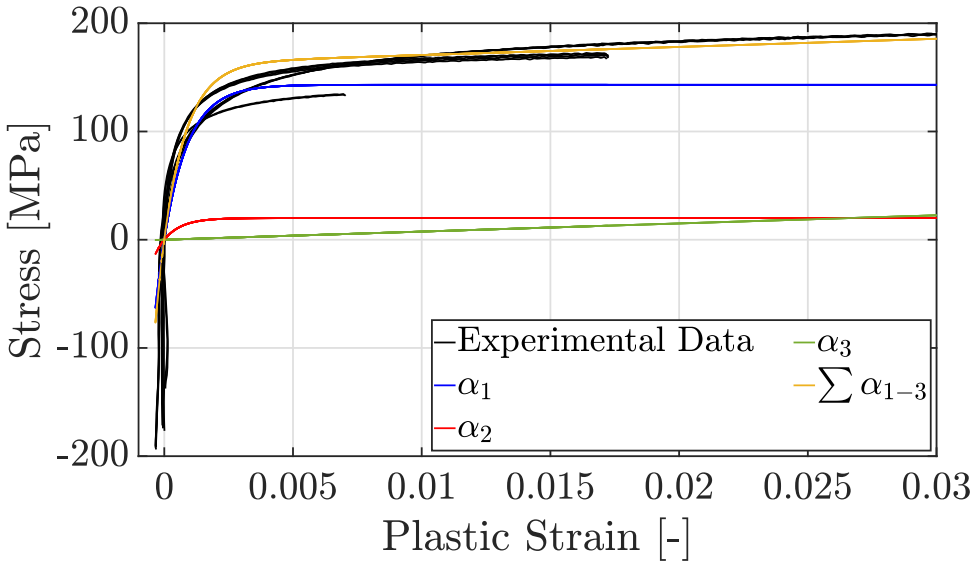

Figure 4.2: Determination of starting values for *RESSPyLab* obtained from CLCF tests, exemplary for $T = 300$ K

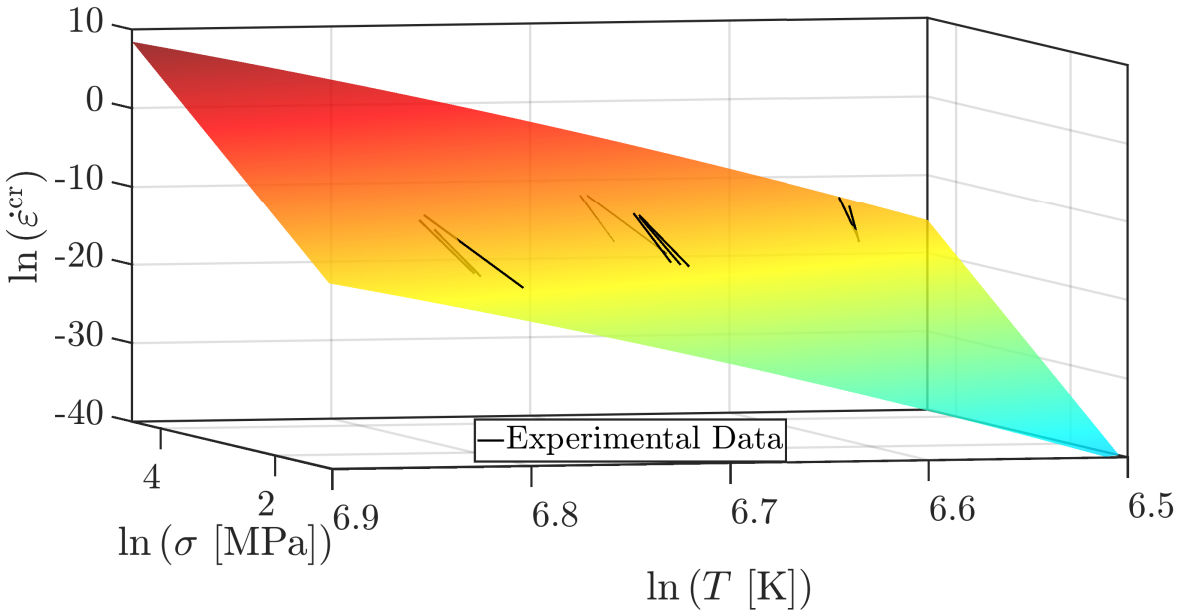

Figure 4.3: Creep surface of Cu-HCP

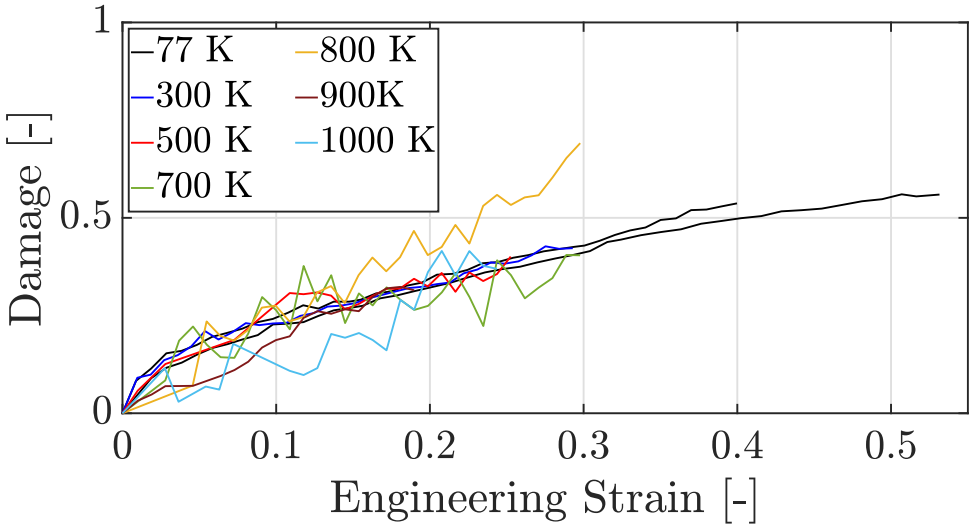

(a) Evolution of the Damage variable in the interrupted tensile tests (Figure 4.1b)

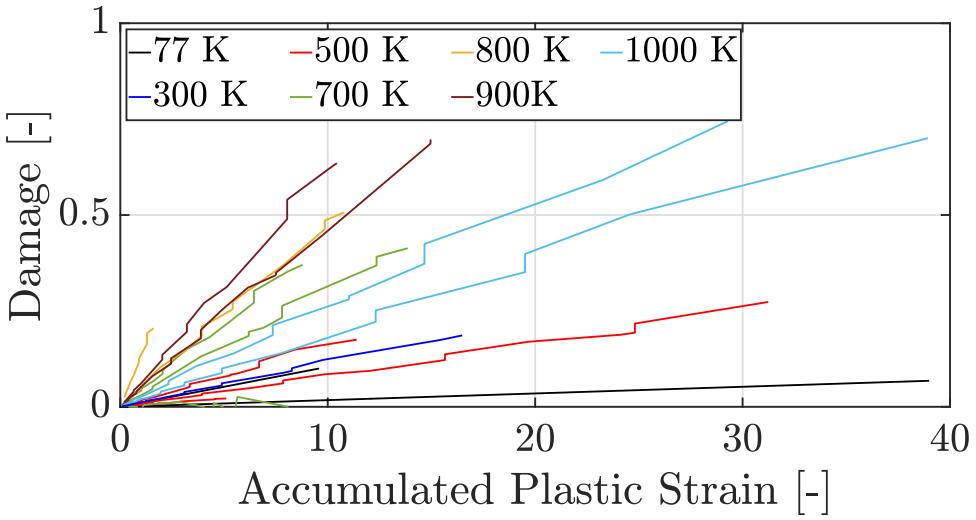

(b) Evolution of the Damage variable in the complex LCF tests (Figure 4.1a)

Figure 4.4: Overview of the Damage variable obtained from tensile and CLCF tests

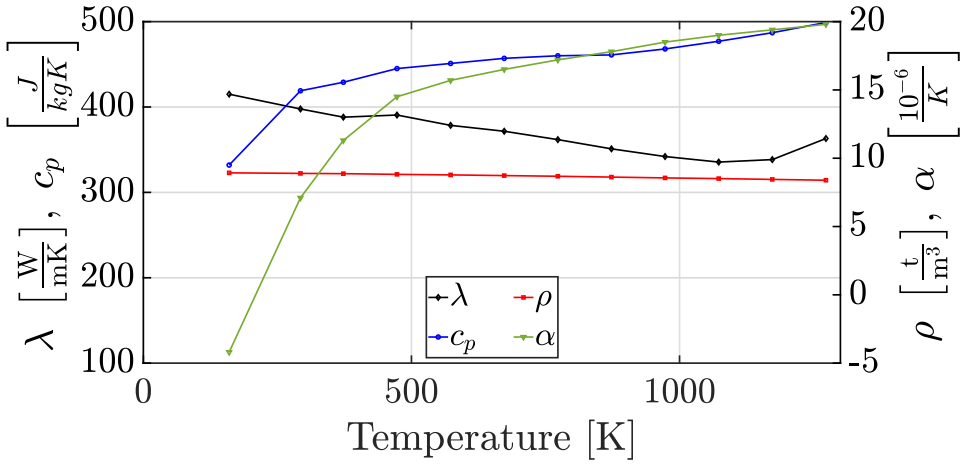

(a) Thermophysical parameters of Cu-HCP

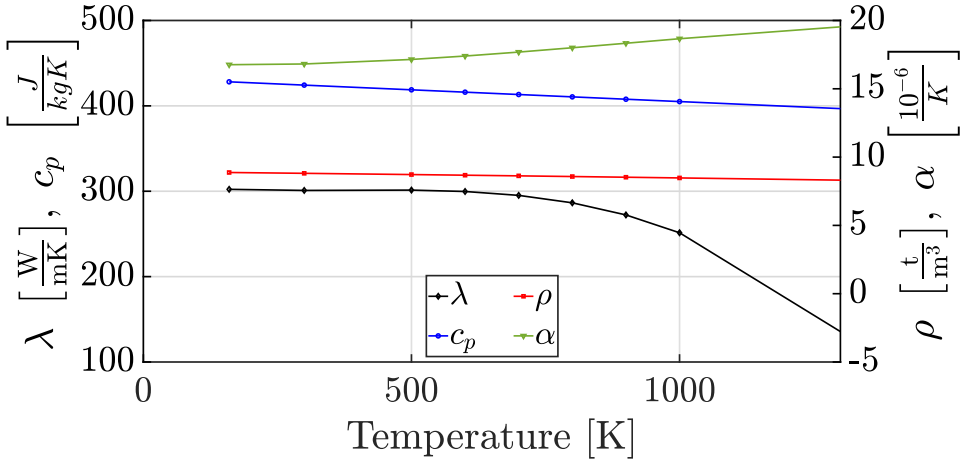

(b) Thermophysical parameters of CuCrZr

Figure 4.5: Thermophysical properties of Cu-HCP and CuCrZr

4.2 Setup in ANSYS

This section presents the setup in ANSYS in detail. It is divided into two parts: first the setup for the simulation of the HTT panel is described, secondly the setup for the mechanical analysis is presented. The purpose of the simulation of the HTT panel is to validate a 3-dimensional coupled fluid-thermal analysis. With this validated analysis the fluid-thermal conditions for the subsequently conducted mechanical analyses are obtained. The results, particularly the temperature distribution, are then fed into a quasi 2-dimensional mechanical analysis. Therefore the 2-dimensional temperature field on the cross section of the point of maximum temperature is extracted from the HTT panel simulation and applied to the quasi 2-dimensional model. This approach saves a huge amount of calculation time and energy. The 2-dimensional approach is justified as experimental data and simulation results do not show displacement and strain in the direction of fluid flow (z direction).

4.2.1 HTT Panel

Heat transfer within both liquid rocket engines and the HTT panel test setup involves dealing with asymmetrically heated cooling channels. Generally, the cooling channel wall is at higher temperature closer to the combustion chamber. Furthermore, the presence of high thermal conductivity in the solid results in significant temperature variations within the solid structure. Hence, it is important to check the order of magnitude of the Biot Number (Equation (4.16)). This assessment provides practical means of determining whether the lumped capacitance method ($Bi \ll 0.1$) [80] is applicable or if a conjugated heat transfer approach ($Bi \gg 0.1$) is required. In the latter case temperature distributions in both the solid and fluid domains must be considered simultaneously. The Biot Number is mathematically expressed as

$$Bi = \frac{hL_\mathrm{c}}{\lambda} \tag{4.16}$$

where h represents the convective heat transfer coefficient, L_c signifies the characteristic length ($L_\mathrm{c} = V/A$), and λ stands for thermal conductivity. The analysis by means of a steady state thermal analysis as published by Kringe [151] suggests that h is of sufficient magnitude to conclude that $Bi > 10$, therefore, necessitating the inclusion of conjugated heat transfer in the simulation.

Boundary Conditions

The boundary conditions for each simulation are derived from the corresponding experimental data at $t = 220$ s, a point at which conditions have stabilized and a steady state has been reached. Specifically, the following conditions are predefined:

- Outlet pressure p_{out}
- Inlet temperature T_{in}
- Mass flow rate per cooling channel $\dot{m}_{\text{cc}}$
- Heat flux q_{w}

The simulation calculates and validates the differential pressure Δp between the inlet and outlet, the maximum surface temperature T_{s}, and the fluid temperature at the outlet T_{out} which can be compared to the experimental data. Furthermore, the 2-dimensional temperature distribution on the laser loaded surface can be compared with the IR camera measurements. As previously mentioned, the laser's heat flux is applied as "Imported Load" via the "External Data" option. This approach enables a precise simulation of the laser loading on the surface, as depicted in Figure 3.6. Radiation and free convection coefficients are set on the outer surfaces of the panel. The environmental temperature within the panel housing is set to $T_{\infty} = 273$ K. Consequently, there's an inward heat flow into the panel for all surfaces where $T_{\text{HTT}} < T_{\infty}$ during the calculation. Only in a small area around the laser-loaded zone is $T_{\text{s}} > T_{\infty}$, resulting in an outward heat flow. The total amount of heat exchanged for both radiation and free convection is of the order of magnitude $Q_{\varepsilon,\text{h}} \approx 10$ W, hence, it is negligible. The physical timescale, which represents the duration required for a N_2 molecule to traverse the cooling channel, was individually computed for each experiment using Equation (4.38). The input data utilized for the simulation of the individual HTT panel cycles is summarized in Table 4.5. Additionally, simulations were performed with the boundary conditions obtained from the Central Point TMF panel test campaign as well as with the data obtained from the Temperature Variation test campaign. This further verifies the temperature distribution for the subsequent structural analysis. The data presented in Table 4.6 was used as input. The resulting temperature distribution is presented in the respective section in Section 5.1

Table 4.5: Experimental results taken as input for the simulation of the HTT panel conditions

Cycle	$\mathbf{T_s}$ [K]	$\mathbf{q_w}$ $\left[\frac{\mathrm{MW}}{\mathrm{m^2}}\right]$	$\mathbf{\dot{m}_{cc,4}}$ $\left[\frac{\mathrm{g}}{\mathrm{s}}\right]$	$\mathbf{p_{out,4}}$ [bar]	$\mathbf{T_{in,4}}$ [K]
16	648	11.95	9.29	67.30	164.83
26	648	19.83	37.59	61.24	162.35
40	648	17.15	25.54	64.38	174.13
19	763	24.64	47.19	60.39	159.45
36	763	19.61	25.28	63.45	161.31
92	763	15.08	12.28	64.46	161.93
28	886	24.39	32.47	63.18	161.90
83	886	20.39	20.13	65.03	164.31
93	886	17.49	12.09	65.61	164.05
34	1000	24.64	25.51	66.30	163.25
84	1000	22.18	19.77	65.52	161.91
94	1000	19.44	12.41	67.66	163.02

Table 4.6: Experimental results taken as input for the simulation of CP and TV test campaigns

Exp	$\mathbf{T_s}$ [K]	$\mathbf{q_w}$ $\left[\frac{\mathrm{MW}}{\mathrm{m^2}}\right]$	$\mathbf{\dot{m}_{cc,4}}$ $\left[\frac{\mathrm{g}}{\mathrm{s}}\right]$	$\mathbf{p_{out,4}}$ [bar]	$\mathbf{T_{in,4}}$ [K]
CP	800	24.25	36.9	63.6	163.9
TV	900	24.25	29.9	64.5	163.4

Geometrical Model

The geometrical model used in the coupled fluid-thermal simulation is displayed in Figure 4.6. Due to its symmetry properties in the y-zplane, it is sufficient to model only half of the HTT panel consisting of three and a half cooling channels. The unique half cooling channel positioned in the middle of the HTT panel serves as the representation of the reference cooling channel within a rocket combustion chamber. This symmetry condition reduces the number of nodes and elements by a factor of two. The symmetry within the x-y plane cannot be employed as the cooling fluid is heated up while passing through the cooling channel. The full length of the TMF panel is required as the position of the maximum surface temperature T_s is shifted downstream by the heating of the coolant. For simplification of meshing and subsequently reduction of

computational time, the bore holes for the interfaces to the fluid system as well as the sealings of the cooling channels are omitted. These simplifications are reasonable as the entry length of the TMF panel geometry accounts for a fully developed turbulent flow in the laser loaded area (see Equation 3.1). Hence, the fluid enters the HTT panel at the position where the sealing are located in the physical panel. Additionally, the bore holes for the pressure sensor are omitted as this simplifies the meshing. They have no effect on the fluid flow itself and the heat conduction in this part of the HTT panel. The edges of the cooling channel are rounded with a radius of $r = 0.24$ mm as obtained from measurements (see Section 3.1.1).

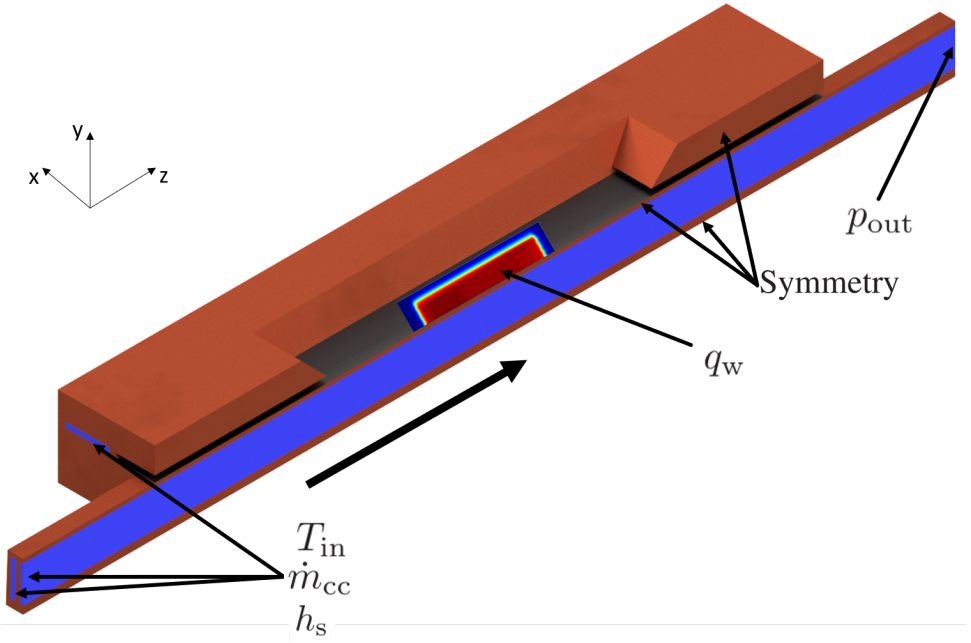

Figure 4.6: Geometrical model with boundary conditions for coupled fluid-thermal analysis in ANSYS

Coupled Fluid Thermal Simulation

To simulate the coupled fluid-thermal interaction, ANSYS CFX was employed for modeling the fluid domain and a steady-state thermal analysis in ANSYS Mechanical for analyzing the thermal field. This is in contrast to previous work where the temperature distribution was simulated by using solely ANSYS CFX [8, 9]. The analysis was carried out under steady-state boundary conditions obtained from the experimental data at $t = 220$ s. Given that the problem involved conjugated heat transfer, a bidirectional data exchange mechanism between ANSYS CFX and Mechanical was established. This exchange

encompassed the transfer of the temperature field, convective heat transfer coefficient, and fluid temperature. The maximum number of coupling iterations was capped at 50 or beforehand when the root mean square (RMS) residual reached RMS < 0.01. In general, it is reasonable to expect that a higher surface temperature would necessitate more iterations for achieving a steady state. The individual RMS residuals for CFX were set to RMS $= 10^{-6}$. In Mechanical, the termination criterion was the temperature difference between two consecutive iterations reaching values below $\Delta T_{\mathrm{i,i+1}} < 0.5\%$. The maximum number of iterations was limited to 200 for CFX and 70 for the steady-state thermal analysis.

Structural Domain

The structural domain serves as a representation of the real HTT panel, closely mirroring the geometry outlined in Section 4.2.1. Unlike previous simulations of HTT (and TMF) panels [8, 9], the curvature in the corners of the cooling channels were incorporated. This curvature originates from the manufacturing process, specifically wire cutting. For the simulation, the thermophysical parameters of the HTT panel material are detailed in Figure 4.5a and Table 4.3.

Fluid Domain

The fluid domain encompasses the supercritical nitrogen contained within the cooling channels of the HTT panel. As previously mentioned, the nitrogen coolant maintains a supercritical state throughout its flow within the HTT panel (see Figure 3.7). Consequently, it is imperative to consider real gas properties (RGP) in the coupled fluid thermal analysis. These real gas properties are derived from the National Institute of Standards and Technology (NIST) REFPROP software. The framework conditions are detailed in Table 4.7, with T_{sat} representing the saturation temperature range, which is of limited relevance here but is included for comprehensiveness. According to

Table 4.7: Frame conditions for real gas property modeling of N_2-coolant.

Parameter	**Span**	**Sampling Points**	**Critical Value**
T	$100 - 2100$ K	801	126.19 K
p	$40 - 75$ bar	801	33.96 bar
T_{sat}	$64 - 125$ K	2	

Schlichting [90] and White [95] the fluid flow is fully turbulent throughout its flow through the cooling channels as the Reynolds number in the experiment is between $Re = 0.93 \times 10^5$ and $Re = 4.89 \times 10^5$ [151] after a sufficiently long inlet length. To accurately model turbulence, the Shear Stress Transport (SST) model within ANSYS CFX is employed. The SST model is rooted in the Reynolds Averaged Navier-Stokes (RANS) equations, specifically the $k-\omega$ model developed by Wilcox [152]. It was formulated by Menter [153] and is highly recommended for precise boundary layer simulations. The roughness of the cooling channel walls plays a significant role in convective heat transfer and was quantified through optical measurements using a microscope (see Section 3.1.2). In accordance with the methodology outlined in the work by Adams [154], the equivalent sand-grain roughness, denoted as h_s which is necessary for the us of a surface roughness model in ANSYS was determined by

$$h_\mathrm{s} = 0.978 R_\mathrm{z}. \tag{4.17}$$

To obtain the value of sand-grain roughness, measurements were executed with various specimen and in different directions within each specimen. The resulting sand-grain roughness value is $h_\mathrm{s} = 1.810 \times 10^{-6}$ m. Estimations of the dimensionless sand-grain roughness, denoted as h_s^+ (see Section 2.4.6), indicate that the wall can be treated as smooth for the lowest experimental Reynolds number. However, it necessitates treatment within the transitional-roughness regime for the majority of experiments. An automated near-wall treatment is employed in this context.

Energy conservation demands for an equivalent heat flux near the wall in both the structural ($q_\mathrm{w,s}$) and fluid ($q_\mathrm{w,f}$) domains. Hence,

$$q_\mathrm{w,s} = q_\mathrm{w,f} \tag{4.18}$$

and using Equation (2.37)

$$-\lambda_\mathrm{Cu} \left.\frac{\partial T}{\partial y}\right|_{y=0} = -\lambda_\mathrm{N_2} \left.\frac{\partial T}{\partial y}\right|_{y=0} \tag{4.19}$$

under the assumption of zero velocity due to the non-slip condition at the wall, the primary transport mechanism in play is heat conduction. The non-slip condition is a result of the wall roughness. The roughness of the wall has a substantial influence on both the thickness and the logarithmic profile of the fluid and subsequently the temperature boundary layer. The dimensionless sand-grain roughness is determined by the following calculation

$$h_\mathrm{s}^+ = \frac{h_\mathrm{s} u_\tau}{\nu} \tag{4.20}$$

where ν is the kinematic viscosity and u_τ represents the friction velocity defined by

$$u_\tau = \left(\frac{\tau_\mathrm{w}}{\rho} \right)^{\frac{1}{2}} \tag{4.21}$$

with the wall shear stress given by

$$\tau_\mathrm{w} = \nu \frac{\partial u}{\partial y}\bigg|_{y=0}. \tag{4.22}$$

The dimensionless form of velocity is obtained as

$$u^+ = \frac{u}{u_\tau}. \tag{4.23}$$

The dimensionless wall distance

$$y^+ = \frac{u_\tau y}{\eta} \tag{4.24}$$

with η being the dynamic viscosity and $\eta = \nu\rho$, the dimensionless velocity gradient is defined as

$$\frac{du^+}{dy^+} = \frac{1}{1 + \frac{\varepsilon_\tau}{\eta}} \tag{4.25}$$

where ε_τ is the turbulent viscosity. To solve Equation (4.25), the near-wall region needs to be examined more closely. The boundary layer is divided into two regions [89]. In the viscous sublayer, the influence of molecular momentum transport is much greater than the turbulent influence, i.e., $\eta >> \varepsilon_\tau$. Integrating Equation (4.25) in this region results in the linear relationship

$$u^+ = y^+ \tag{4.26}$$

for the universal velocity profile. In the turbulent layer, turbulent forces dominate over friction forces, and it holds that $\eta << \varepsilon_\tau$. For this layer, the turbulent viscosity ε_τ can be expressed using the Prandtl mixing hypothesis. This leads to the logarithmic relationship for the dimensionless velocity u^+ and wall distance y^+

$$u^+ = \frac{1}{\kappa} \ln(y^+) + C \tag{4.27}$$

with the constants $\kappa = 0.41$ and $C = 5.2$ [95].
The temperature profile in the near-wall region can be determined in the same way due to the analogy between momentum and heat transport. The two-layer

approach is still employed, where heat is first transported into the boundary layer through molecular conduction, and then turbulent fluctuation variables take over the energy transport within the boundary layer. Neglecting the convective term $u\partial T/\partial x$ in the near-wall region compared to the other terms and introducing the dimensionless temperature

$$T^+ = \frac{T - T_\mathrm{w}}{T_\tau} \tag{4.28}$$

with

$$T_\tau = -\frac{q_\mathrm{w}}{\rho c_\mathrm{p} u_\tau} \tag{4.29}$$

and

$$q_\mathrm{w} = -\lambda \frac{\partial T}{\partial y}\bigg|_{y=0}, \tag{4.30}$$

the dimensionless temperature gradient in the near-wall region is given by

$$\frac{dT^+}{dy^+} = \frac{1}{\frac{1}{\mathrm{Pr}} + \frac{\varepsilon_q}{\upsilon}}. \tag{4.31}$$

Here, the molecular Prandtl number is defined as

$$\mathrm{Pr} = \frac{\eta}{\alpha}, \tag{4.32}$$

with the thermal diffusivity α. Considering the two layers again, in the viscous sublayer, integrating Equation (4.31) results in the universal temperature profile linear relationship

$$T^+ = \mathrm{Pr} y^+. \tag{4.33}$$

For the fully turbulent region, using the turbulent Prandtl number

$$\mathrm{Pr}_\tau = \frac{\eta_\mathrm{t} c_\mathrm{p}}{\lambda_\mathrm{t}}, \tag{4.34}$$

which can be determined as a function of Reynolds and Prandtl numbers using the equation

$$\mathrm{Pr}_\mathrm{t} = K_1 + K_2 \frac{1}{\mathrm{PrRe}^\mathrm{m}} \tag{4.35}$$

the logarithmic wall law for temperature or the universal temperature profile is obtained as

$$T^+ = \frac{\mathrm{Pr}_\mathrm{t}}{\kappa} \ln(y^+) + C_\mathrm{T}, \tag{4.36}$$

with the Karman constant κ, which reflects the analogy to Equation 4.27. For the parameter C_{T}, capturing the influence of the molecular Prandtl number for different media, the empirical correlation equation

$$C_{\mathrm{T}} = 12.8\mathrm{Pr}^{0.68} - 7.3 \tag{4.37}$$

can be used [155].
Another crucial parameter that must be configured in ANSYS CFX which is significant for ensuring the convergence of the simulation within CFX, is the physical timescale. This timescale is determined using

$$t_{\mathrm{ph}} = \frac{l_{\mathrm{cc}}}{u} \tag{4.38}$$

Here, l_{cc} represents the length of the cooling channel, and when combined with the conservation of mass in Equation (2.48) it signifies the time required for a fluid molecule to pass through the cooling channel.

Meshing

In both subdomains fluid and structural, 3D hexahedral elements were used for meshing. In regions with elevated heat flux, mesh refinement was applied. Specifically, for the area exposed to the laser's heat load, the surface mesh exhibited a squarish pattern with a node spacing of 0.26 mm $\times$ 0.26 mm, following the measurement of the laser intensity distribution (see Section 3.2.1). A mesh convergence analysis was conducted using a representative model to identify the most suitable meshing parameters. This approach was limited by constraints related to available computational resources. The representative model included a single cooling channel with its adjacent wall structure and maintained a consistent heat flux on the surface exposed to the laser. The selection of fluid conditions ($p_{\mathrm{out}}, T_{\mathrm{in}}, \dot{m}$) aligned with the experimental data. The primary objective was to achieve a balance between boundary layer resolution and computational efficiency. The results are presented in Figure 4.7. Based on the outcomes of the convergence study, the following mesh parameters were established: 32 elements along the width (x direction) of the cooling channel (refer to Figure 4.7a), a first mesh layer thickness of $x_{\mathrm{p}} = 0.0137$ μm (see Figure 4.7b), and a total of 28 prism layers. A comprehensive overview of the resulting total element and node count in the structural and fluid domain is presented in Table 4.8.

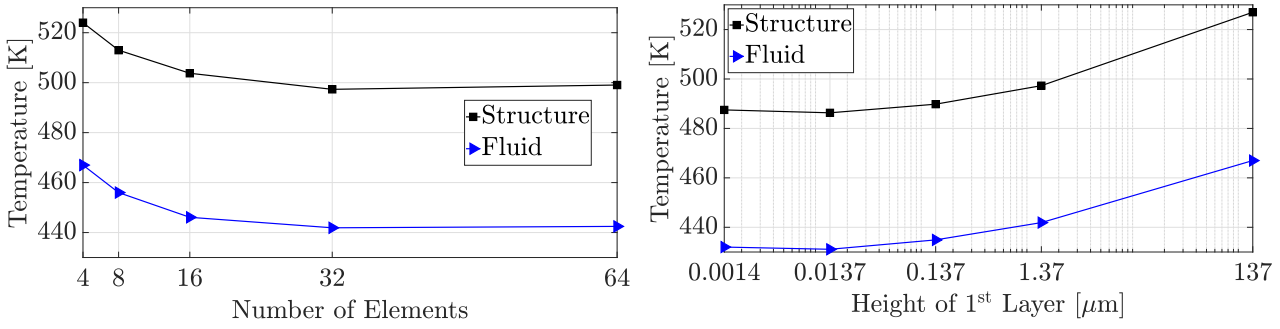

(a) Meshing study for the number of elements on the laser heated wall (x direction)

(b) Mesh study for thickness of the first prism layer

Figure 4.7: Meshing study for the 2-way coupled fluid-thermal simulation

Table 4.8: HTT meshing properties

Domain	**Elements**	**Nodes**
Structural	1.28×10^6	5.42×10^6
Fluid	4.39×10^6	17.84×10^6

4.2.2 Mechanical Analysis

This section introduces the setup for the static structural analysis in ANSYS Mechanical.

Geometrical Model

As mentioned earlier, a quasi 2-dimensional cross section of the TMF panel is used representing the section of maximum surface temperature T_s. A purely 2-dimensional analysis could not be executed as this option is not supported by the User Programmable Features used in the context of this work. Hence, the thickness in axial (z) direction was set to $t_z = 0.02$ mm. The model uses axial symmetry in the centerline of the central cooling channel, reducing the amount of elements by a factor of two. The dimensions as shown in Figure 4.8 are similar to the technical drawing of the TMF panel. The only exception is the additional radius in the cooling channels originating from manufacturing.

Meshing

For all mechanical analyses the same mesh is utilized. Due to constraints of the UPFs only uniform hexagonal elements could be used. The physics preference

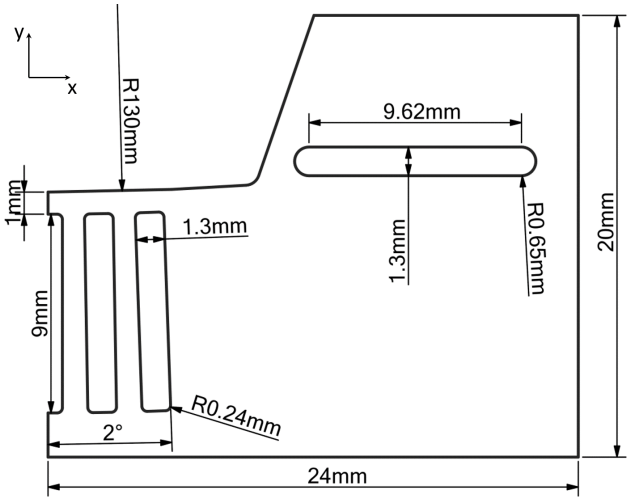

Figure 4.8: Geometrical model for analysis in ANSYS Mechanical

was set to Nonlinear Mechanical, as the considered problem deals with highly nonlinear material performance, with a Quadratic Element Order. By means of a Command Snippet it was ensured that only the element type SOLID186 [156] was present. The SOLID186 element has 20 nodes with three degrees of freedom per node. These refer to the translations in x, y and z directions. Uniform reduced integration is ensured by setting the key option (2) to 0. The mesh density varies from a very dense mesh within the region of the inner cooling channels and the laser loaded wall to a coarse mesh further outside. A single element was used in axial (z) direction. A mesh study was performed to ensure that stresses and strains do not depend on the mesh density. The results are presented in Figure 4.9.

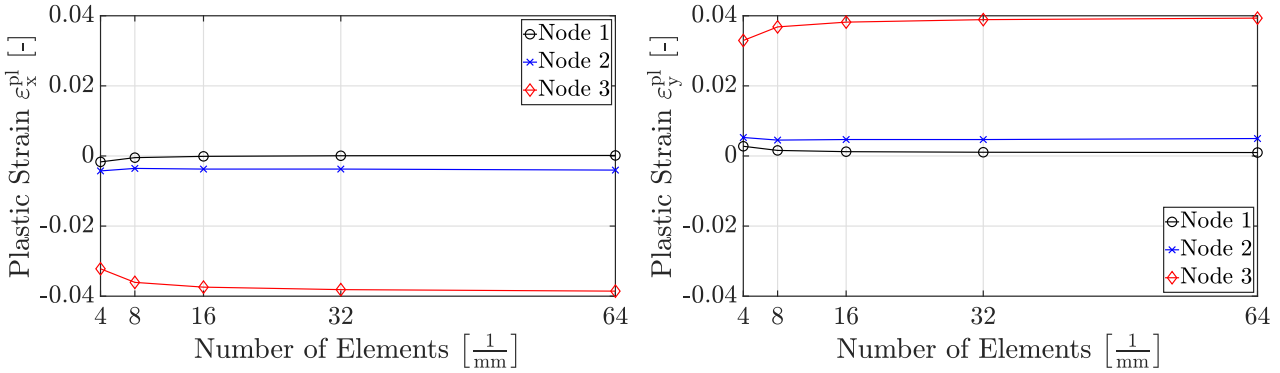

(a) Mesh study for strains in x-direction

(b) Mesh study in y-direction

Figure 4.9: Mesh study for analysis in ANSYS Mechanical

The mesh study was executed for the simulation of the central point by using

the material parameters of the Standard ANSYS Mechanical configuration. Herein the residual plastic strains were evaluated for the x and y direction at a simulation time of $t = 6820$ s, corresponding to the end of the 5^{th} cycle, for three different nodes of interest on the centerline of the central cooling channel. These strains were chosen as they drive the fatigue life in the following post processing. The number of elements along the centerline is denoted on the abscissa. It was varied by a factor of 2 by applying the option Edge Sizing. Additionally, the number of elements on the remaining Edge Sizing options were changed by a factor of 2 guaranteeing a uniform distribution of elements per millimeter. Figure 4.9 shows that a quantity of 32 elements per millimeter is sufficient to achieve mesh independence for the mechanical simulation. This results in an overall number of elements and nodes as seen in Table 4.9.

Elements	30350
Nodes	217144

Table 4.9: Meshing properties of the mechanical analyses

The mesh quality per element is calculated by

$$Q_{\text{E}} = C \left[\frac{V_{\text{E}}}{\sqrt{(\sum a^2)}} \right] \tag{4.39}$$

where $C = 41.56922$ is a element type factor [157], V_{E} is the element volume and a is the edge length. $Q_{\text{E}} \geq 0.856$ could be reached in the region of the cooling channels for all the elements present (25203 elements). The final mesh is presented in Figure 4.10.

Boundary Conditions

Constraints The constraints for the mechanical simulation need to take account for the quasi 2-dimensional character of the model, hence representing a cut-out section of the actual TMF panel. A symmetry region was applied to the centerline of the central cooling channel, constraining the model in tangential (x) direction [158]. To constrain the model in radial (y) direction, the lower face was held by a displacement constraint with the conditions $y = 0$ while x, z were set to "free". Constraints in axial (z) direction was realized by using another displacement with $z = 0$ on one of the faces in the x-y-plane, while x, y again were set to free movement. To cover the 3-dimensional character of the

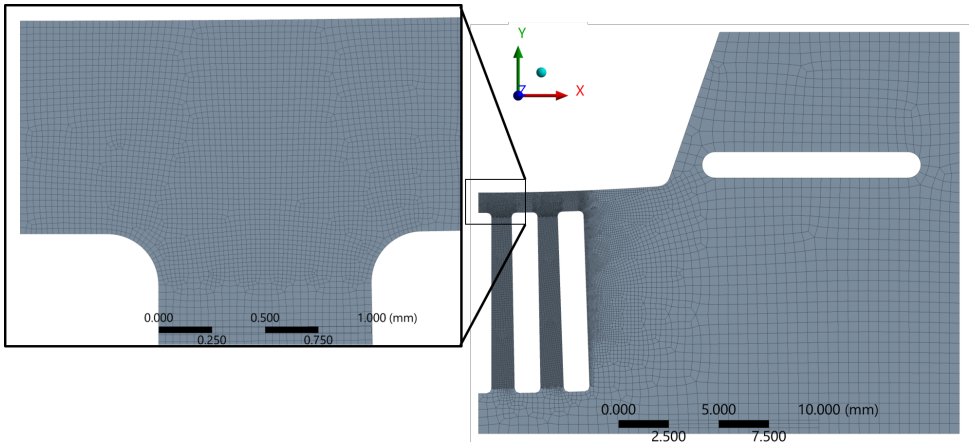

Figure 4.10: Mesh for the static structural analysis in ANSYS Mechanical

actual TMF panel in the 2-dimensional simulation the degrees of freedom in axial (z) direction of all nodes on the opposite face in the x-y-plane ($z = 0.02$) were constraint by coupling their displacement u_z with a Command Snippet. This guarantees a uniform movement of this face. A similar constraint was applied to the face at $x = x_{max}$ (far right) but here the displacement u_x of all nodes was coupled.

Temperature, Pressure The temperature distribution for the cross section in the static structural analysis was extracted from the cross section of the maximum surface temperature in the coupled fluid-thermal simulation. This temperature distribution was then applied to the static structural simulation of the 2-dimensional model in ANSYS Mechanical as an imported load. To simplify the analysis, only the relevant time steps for each cycle at $t = [0, 30, 230, 260, 740]$ s were modeled. In between the defined time steps ANSYS automatically linearly interpolates the conditions. In addition to the temperature profile, the pressure inside the cooling channels as obtained from the experimental results (see Chapter 5) was applied. Figure 4.11 presents the thermal and pressure boundary conditions for the different test cases. As an example, the pressure in the central cooling channel and the maximum surface temperature are displayed. The complete temperature distributions that are applied to the cross section are presented in the respective sections in Chapter 5.

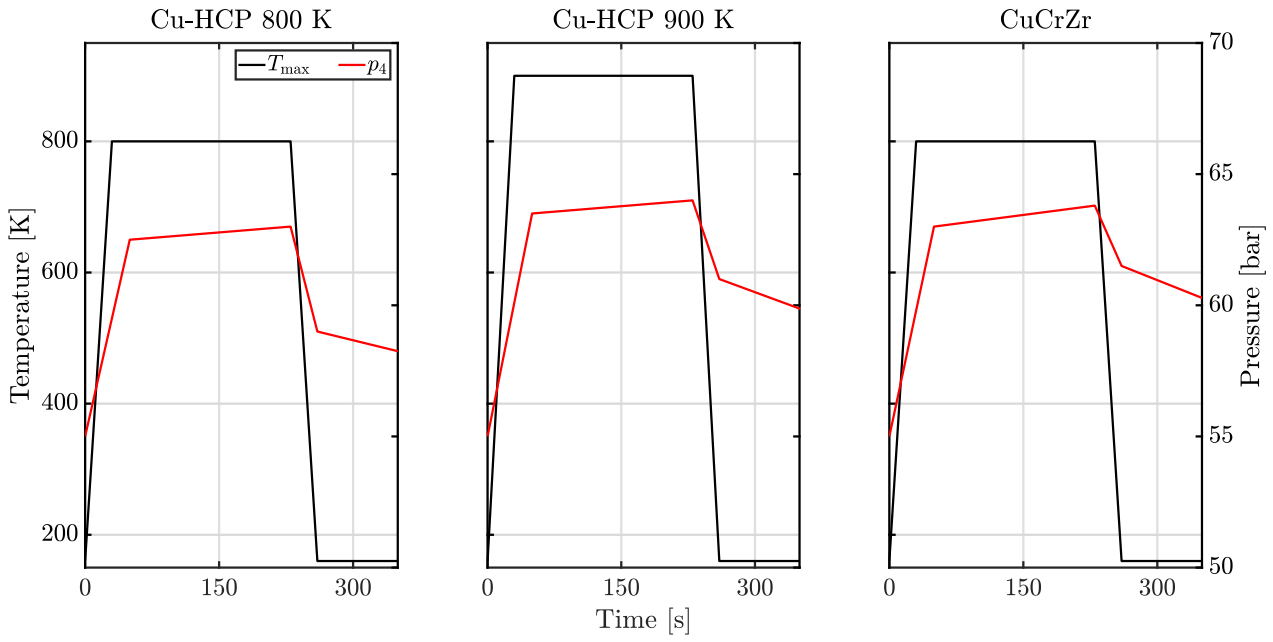

Figure 4.11: Temperature and pressure boundary conditions in the static structural analyses

Analysis Options

In each analysis for Cu-HCP 5 consecutive cycles with similar boundary conditions have been calculated. Due to the very low strain levels obtained for CuCrZr 10 cycles were calculated for this material. As results from calculations by Thiede [9], Masuoka [65] and Gulczynski [159] indicate the stress-strain relation, in particular the ratcheting effect, stays almost constant after an initial phase of cyclic hardening as no damage is involved in their calculation. In order to achieve convergence, each step used several substeps. This has not been a requirement for the simulations with Standard ANSYS Mechanical but both UPFs did not converge without predefined substeps. Therefore, a minimum number of 100 substeps was introduced, the maximum was set to 100,000. The Large Deflection option was set to "On". The reference temperature for all material parameters was set to $T_{\mathrm{ref}} = 293$ K. The engineering data for the UPFs was inserted with APDL Command Snippets. For automation, the results were extracted by Command Snippets as well, delivering text files (*.txt) for post-processing and damage evaluation in Matlab.

5 Results

In this chapter the experimental and numerical results of the four test cases are presented. First, the HTT panel results are presented as the validated temperature field obtained by the 2-way coupled simulation serves as an important input for the following simulations of the TMF panel test cases.

5.1 Heat Transfer Test Panel

In Figure 5.1a the main results of the HTT panel are presented. It shows the dependency of the HTT panel surface temperature T_s on the Reynolds number, summarizing the mass flow rate, temperature and pressure of the fluid, and the heat flux. The inlet Reynolds number was chosen on the abscissa to account for the margins in inlet pressure and temperature. The data was evaluated at cycle time of $t_\mathrm{on} = 220$ s (including 30 s of ramp-up). At this point steady state conditions in the HTT panel are reached. For the four different surface temperatures $T_\mathrm{s} = [648;\ 763;\ 886;\ 1000]$ K evaluated, the heat flux varied between $q_\mathrm{w} = 12$ ... 24.6 MW/m^2, resulting in a variation of the mass flow rate per cooling channel between $\dot{m}_\mathrm{cc} = 8.0$ ... 47.0 g/s. A linear relationship for the curves of constant temperature can be observed at low Reynolds numbers. However, as the Reynolds number increases, the curves become nonlinear. This effect becomes particularly pronounced in the plot for $T_\mathrm{s} = 763$ K. Extrapolating the curve might lead to an asymptotic maximum value of the heat flux. At this maximum value the heat flux cannot be further increased while maintaining a constant surface temperature, despite an increase in mass flow. However, further investigation is necessary to validate this hypothesis, considering the limited number of available data points. Through interpolation using Figure 5.1a, it is now feasible to estimate the surface temperature of the HTT panel for any desired boundary condition within the range of the experimental data. Moreover, this interpolation enables the prediction of the maximum surface temperature of subsequent TMF panel test campaigns for any combination of heat flux and mass flow rate within the examined range specifically for Cu-HCP. The relatively large error bars in Figure 5.1a are the result of the high measurement uncertainty of the emissivity as described in Section 3.1.3. However, the results of the HTT panel could be reproduced within reasonable accuracy

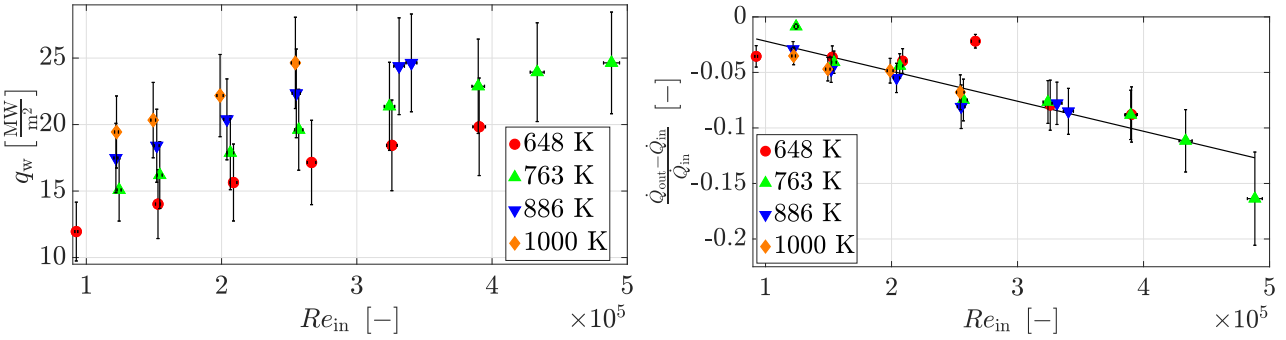

(a) Results for the heat flux over inlet Reynolds number of the HTT Panel

(b) Balance of Energy over inlet Reynolds number of the HTT Panel

Figure 5.1: Experimental results of the HTT panel

in the following test campaigns. Another important result of the HTT panel test campaign is the balance of energy displayed in Figure 5.1b in normalized form. The inward rate of heat flow is governed by the laser output power P_{out} and the emissivity $\varepsilon_{940\text{ nm}}$ of the coating at the wavelength of the laser. It is calculated by Equations (2.45), (2.46) and (2.47). As explained in Chapter 2, the heat transferred through free convection and radiation from the HTT and later TMF panels surface is significantly lower compared to the heat transported within the fluid. Consequently, the apparent disparity between $\dot{Q}_{\text{out}}$ and $\dot{Q}_{\text{in}}$ primarily stems from thermal conduction into the piping of the fluid supply system, as it serves as the sole physical connection of the HTT panel. The interfaces in this system are composed of the Nickel-base alloy MONEL400 with a thermal conductivity of $\lambda_{\text{Monel400}} \approx 25$ W/(mK). According to Figure 5.1b, the thermal conduction into the interfaces increases linearly with increasing Reynolds number.

The left side of Figure 5.2 presents the temperature distribution obtained from the infrared camera during cycle 34, chosen as an example (see Table 4.5). On the right side, the corresponding result from the coupled ANSYS simulation in ANSYS is shown. The maximum temperatures recorded are $T_{\text{s,IR}} = 996$ K for the infrared measurement and $T_{\text{s,Sim}} = 987$ K for the simulation. The corresponding heat flux was $q_{\text{w}} = 24.6$ MW/m^2 accompanied with a Reynolds number of $Re_{\text{in}} = 2.55 \times 10^5$. This yields a deviation of only $\Delta T_{\text{s}} = 0.9\%$, which is well below the measurement uncertainties of the IR camera. It is crucial to note the geometric congruence observed in both the x and z directions. Accuracy in the temperature field becomes particularly important when incorporating structural analysis into the simulation. It is worth mentioning that the uniform blue color in the infrared image is due to the camera's limited capability to

resolve temperatures below 273 K that occur outside the laser-heated area. Another significant aspect indicating the quality of the method and simulation is the deviation between the results for the parameters T_s, Δp, and T_{out} obtained from the experiment and simulation. Figure 5.3 displays these results, demonstrating an overall small and acceptable level of deviation. However, a clear

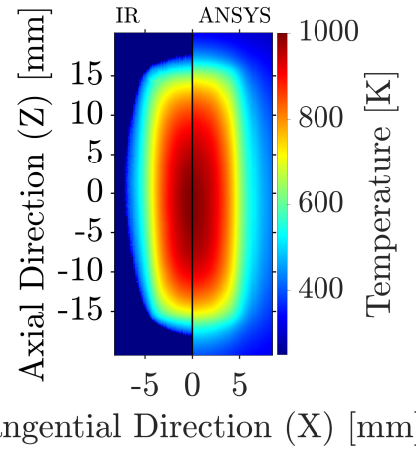

Figure 5.2: Comparison of the 2-dimensional temperature profile on the TMF panel surface for experiment 34. Infrared camera shown left, coupled simulation right.

trend is observed in all three graphs. At low Reynolds numbers, the deviation is positive ($\Delta > 0$), while at high Reynolds numbers, the deviation changes to negative ($\Delta < 0$). In Figure 5.3a, this transition can be observed at approximately $Re_{in} \approx 2.7 \times 10^5$ for ΔT_s. However, for Δp and ΔT_{out} in Figures 5.3b and 5.3c, the transition occurs around $Re_{in} \approx 3.55 \times 10^5$. Therefore, it can be concluded that the simulation underpredicts T_s for $Re_{in} < 2.7 \times 10^5$, but overpredicts T_s for $Re_{in} > 2.7 \times 10^5$. This statement also holds true for Δp and T_{out} but with a different transition point at approximately $Re_{in} \approx 3.55 \times 10^5$. It is important to note that high Reynolds numbers correspond to high heat fluxes. Bear in mind that for the linear fit in Figure 5.3b, the values for $Re_{in} < 1.5 \times 10^5$ have been excluded. The significant deviation observed in this range is attributed to the low mass flow rate and subsequently low differential pressure. This leads to an exceptionally large measurement error (see Chapter 3), which is assumed to be the primary influencing factor in this case. The results of the 2-way coupled simulation and its small deviation from experimental results is also a confirmation of the test setup. In particular, the measurements of heat flux and surface temperature are credible now as they are influenced by the high uncertainty of the coefficient of emissivity (see Figure 3.3).

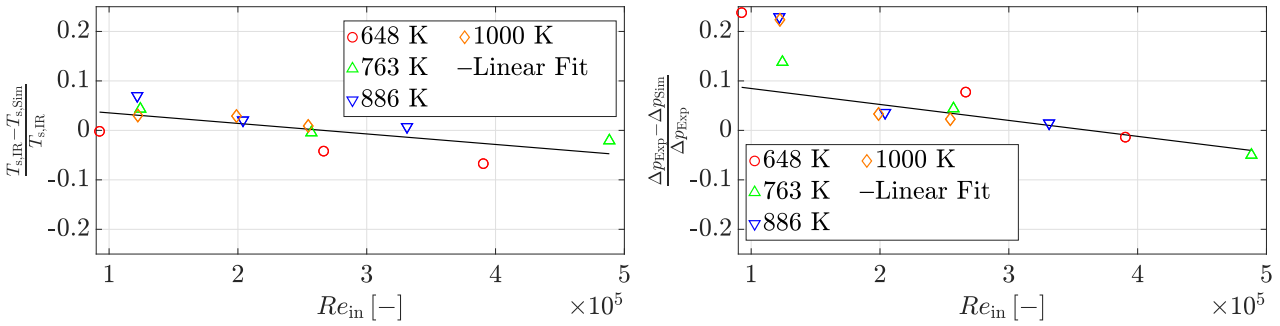

(a) Normalized difference of the maximum surface temperature T_{s}

(b) Normalized difference of pressure loss Δp

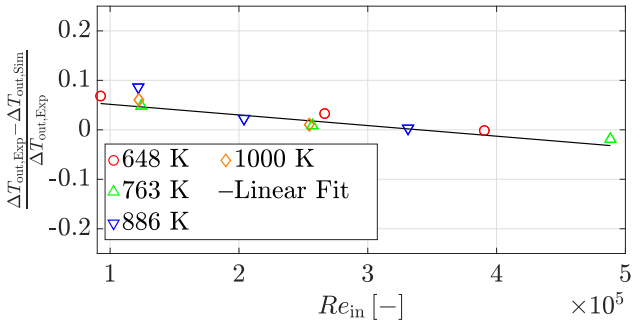

(c) Normalized difference of fluid outlet temperature in the central cooling channel $T_{4,\text{out}}$

Figure 5.3: Normalized differences between experiment and simulation over inlet Reynolds number of the HTT Panel

5.2 Central Point

The boundary conditions of the central point (CP) TMF panel test campaign to which the other experimental results are compared are chosen to be $T_s = 800$ K, $q_w = 24.25$ MW/m^2 and $t_{on} = 200$ s. This section presents the experimental results, in particular the fluid conditions and mechanical performance, as well as the achieved numerical results.

5.2.1 Experimental Results

The fatigue life of the CP TMF panel in the experiment was 151 laser-on cycles.

Fluid Conditions

Figure 5.4 illustrates the fluid conditions observed during the test campaign. The dotted lines indicate the initial conditions at the start of the cycle when the laser is activated ($t = 0$ s), while the solid line represents the conditions at a steady state ($t = 220$ s). It is evident that the target values for $T_{4,in}$ and $p_{4,out}$ at start of the cycle were consistently achieved throughout the test campaign. In Figure 5.4b, the inlet temperature shows a gradual increase of approximately $\Delta T_{4,in} = 3.0$ K to $T_{4,in} = 163.0^{+5.1}_{-1.1}$ K during the laser activation period, and the outlet temperature rises by around $\Delta T_{4,out} = 20.7$ K to $T_{4,out} = 180.7^{+3.3}_{-3.2}$ K. These temperature changes remain relatively constant throughout the test campaign. Regarding the pressure in Figure 5.4c, both the inlet and outlet pressures exhibit an increase of $\Delta p_{4,in,out} = 7.5$ bar to $p_{4,in} = 62.9^{+1.6}_{-1.9}$ bar and $p_{4,out} = 62.5^{+1.7}_{-1.9}$ bar with some minor fluctuations, which are slightly more pronounced. Nevertheless, the pressure values also remain quite constant throughout the test campaign. The observed constant behavior depicted in Figures 5.4b and 5.4c appear contradictory to the trends of the mass flow rate shown in Figure 5.4a. It ranges from $\dot{m}_{tot} = 238.3$ g/s to $\hat{\dot{m}}_{tot} = 277.0$ g/s (excluding cycles 1 to 6). The initial mass flow rate (after cycle 6) was $\dot{m}_{tot} = 260.1$ g/s which is $\Delta\dot{m} = 22.7_{tot}$ g/s (or 8.0%) lower than calculated from the results of the HTT panel test (see Fig. 5.1a). However, this deviation is acceptable considering that the CP TMF panel is at a virgin state in the first 6 cycles while the HTT panel was already subjected to initial damage at the point the data for interpolation was taken. During the first half of the test campaign, the mass flow rate had to be increased, while in the second half, it had to be significantly reduced. To explain this development, several factors need to be considered. During the first half of the TMF panel test

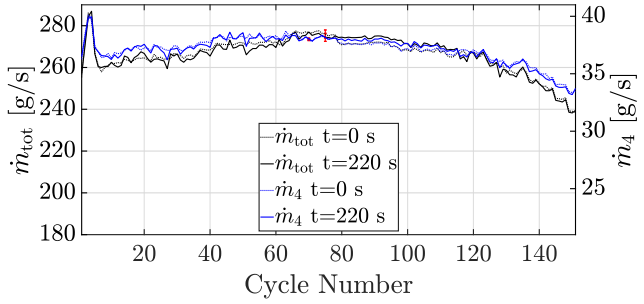

(a) Overall mass flow rate and mass flow rate in the central cooling channel for central point

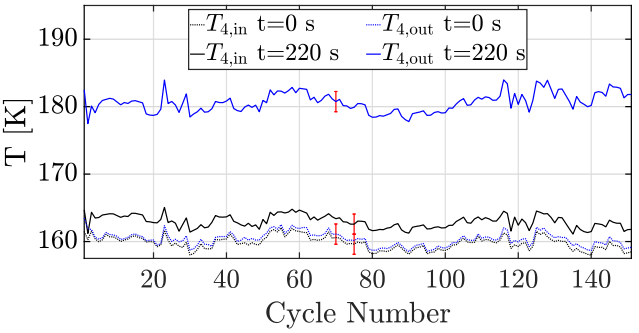

(b) Inlet and outlet temperatures of the central cooling channel for central point

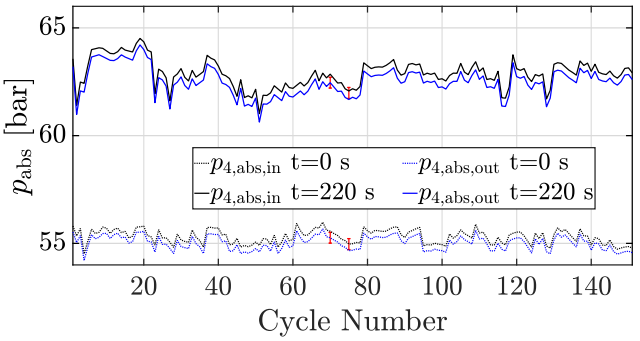

(c) Inlet and outlet pressure of the central cooling channel for central point

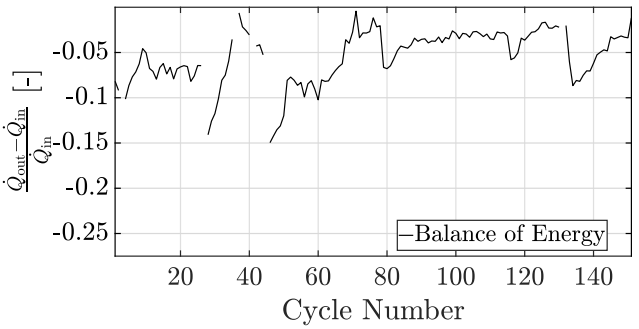

(d) Balance of energy for central point

Figure 5.4: Fluid conditions for central point

campaign, it is hypothesized that certain thermophysical parameters, specifically thermal conductivity, decrease due to the accumulation of plastic strains resulting from changes in grain size, creep, and other factors as well as the initiation of micro voids in the material. It is important to note that these effects are only observed in the x and y directions, meaning that the material does not experience deformation or strain in the flow (z) direction. The decrease in thermal conductivity is supported by the energy balance depicted in Figure 5.4d. This graph represents the disparity between the incoming heat flow rate supplied by the laser and the outgoing heat flow rate measured in the coolant. It is postulated that this disparity arises from heat conduction into the piping system [38]. A linear fit through the data in Figure 5.4d suggests that the heat conduction into the piping system diminishes over the course of the test campaign. Consequently, it is proposed that the aforementioned effects, which cause degradation of the thermophysical parameters of the material, result in more heat being transferred into the coolant fluid instead of being conducted through the piping system. It is assumed that the direct heat flow into the coolant is blocked as Figure 5.28 suggests and therefore heat conduction in the

undamaged parts of the TMF panel increases. The decrease of thermal conductivity could be measured in collaboration with the University of Virginia, Department of Mechanical & Aerospace Engineering (see Section 5.5). This, in turn, leads to a consistent fluid temperature despite an increase in mass flow rate. Another factor, growth of the cross section of the cooling channel, affects the observed behavior in the second half of the test campaign. This change in cross section results in a larger surface area for heat transfer into the fluid. The growth of the cross-section is identified by a sharp increase in deformation of the laser-loaded surface, as recorded by the LIMESS DIC system and shown later in Figure 5.7a. The deformation exhibits a significant increase, particularly around the time when the mass flow rate transitions from increasing to decreasing. This indicates that the growth of the cooling channel cross-section contributes to the changes observed in the TMF panel during the second half of the test campaign. In addition, the deformation of the wall between the laser-loaded surface and the coolant leads to a thinning of this wall. Consequently, the temperature on the coolant side increases, resulting in higher convective heat transfer to the coolant as Equation (2.38) proposes. On the other hand, the surface temperature on the laser-loaded side decreases due to these effects. These changes can be observed in the temperature plots shown in Figure 5.6. During the first half of the test campaign, represented by Cycle 6 and Cycle 75, there is minimal change in the temperature distribution on the laser-loaded surface. However, a distinct shift in the temperature distribution can be observed from Cycle 75 to Cycle 151. This shift is a direct result of the deformation and thinning of the cooling channel wall caused by the ongoing test conditions. Figure 5.5 provides an overview of the fluid conditions during Cycles 6, 75, and 151 in the central cooling channel. It is evident that both the temperature and pressure of the N_2 coolant gradually increase from the start of the laser until reaching steady state conditions at $t = 220$ s. In particular, the red curves representing cycle 151 clearly demonstrate the occurrence of a crack in the central cooling channel. This can be observed prominently in the plot of the differential pressure between the inlet and outlet of the central cooling channel shown in Figure 5.5d. The development of the crack becomes apparent through the initial drop in differential pressure around $t = 191$ s. This is followed by a rapid decline lasting approximately 4 seconds, after which a stabilization process occurs at $t = 195$ s. During this stabilization, the differential pressure converges to a value around $\Delta p_{4,151} = 100$ mbar. Additionally, the second to last IR image on the right hand side of Figure 5.6 displays the last frame captured before the crack becomes visible, while far right IR image shows the initial frame after the crack has occurred, clearly revealing a large cold spot

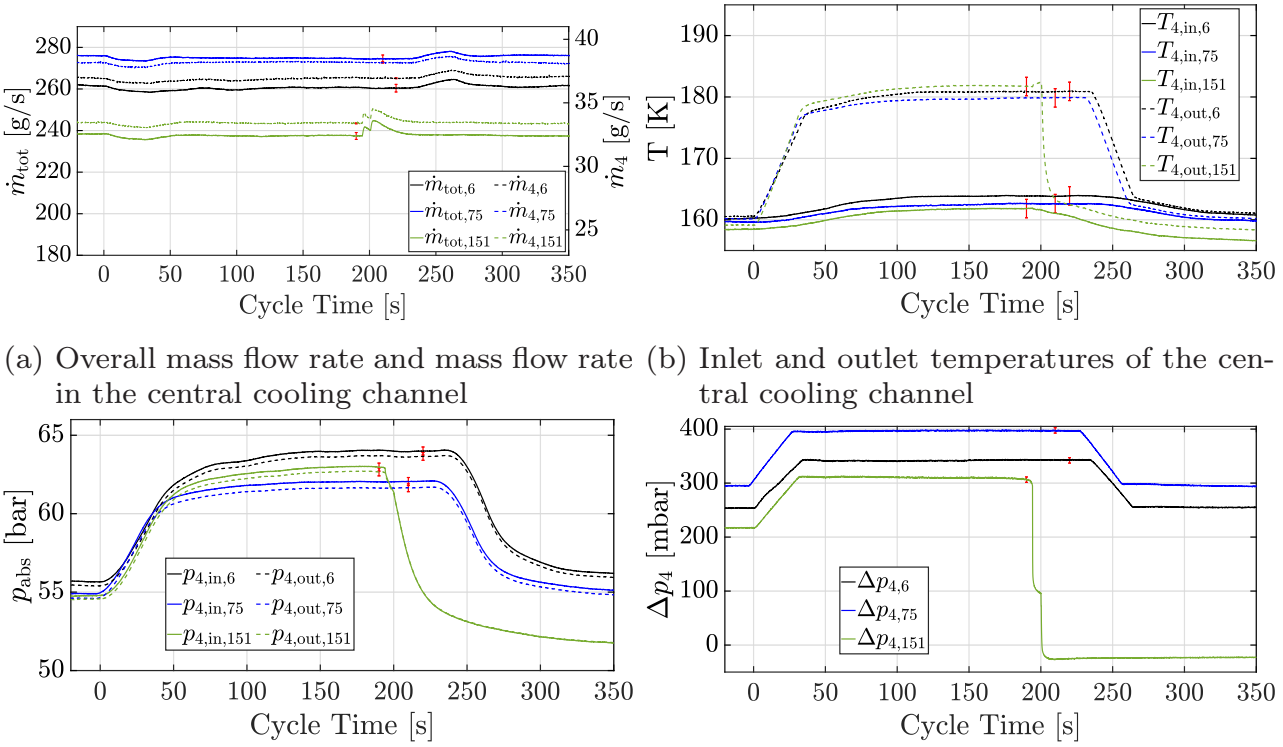

(a) Overall mass flow rate and mass flow rate in the central cooling channel

(b) Inlet and outlet temperatures of the central cooling channel

(c) Inlet and outlet pressure of the central cooling channel

(d) Pressure difference in the central cooling channel

Figure 5.5: Fluid conditions for central point at representative Cycles 6, 75, and 151

where the N_2 coolant is leaking out of the wall. Subsequently, at $t = 200$ s, the laser is manually switched off. The $\Delta p_{4,151}$ then drops below zero, indicating that a portion of the coolant is flowing backward from the collector to the crack. Also worth noting is the performance of the mass flow rate during a laser cycle (Fig. 5.5a). Conspicuous is the drop in mass flow rate while the laser is ramped up. This effect happens due to the decrease of the density of the N_2 coolant during the initial laser phase. The lower density requires more volume inside the cooling channel, blocking the passage. The obversed effect is visible by the increase of the mass flow rate during the ramp-down. Cooler fluid requires less volume in the cooling channel, freeing the passage for more coolant. The deviation from the target mass flow rate due to these effects is $\Delta\dot{m}_{\mathrm{tot}} = ^{+3.6}_{-2.7}$ g/s.

Mechanical Observations

As already mentioned, Figure 5.7a demonstrates the progress of the increasing deformation of the TMF panel surface for every 10^{th} cycle, reaching a maximum

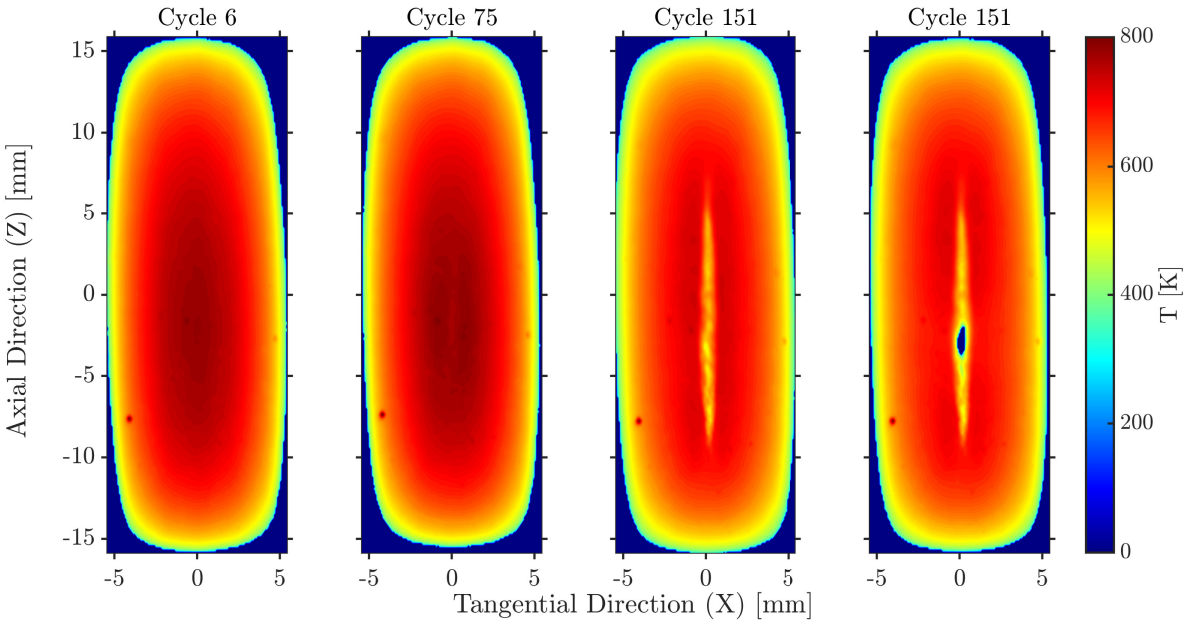

Figure 5.6: Temperature distribution of the laser loaded surface for the Central Point test campaign retrieved from the IR camera measurements for cycles 6, 75, and 151 directly before and after occurrence of the crack. Flow direction is top-down.

value of $\Delta y = 0.91$ mm after the final cycle. From the first few grey lines one can see that from the very beginning of the test campaign bulging above the fillets adjacent to the central cooling channels occurs, leading to a concave surface directly above the channel. This changes towards a convex bulge above the cooling channel after around 60 cycles leading to a bubble. Figure 5.7b shows a CT scan of the damaged cross section of the inner 5 cooling channels after the test. One can see the cooling channels 3 and 5 adjacent to the central cooling channel show high deformation. Note that the curvature of the cooling channel walls is an artifact of the CT scan and does not represent the actual shape. The crack size at the end of the test campaign covers an almost elliptical area that spans $A_{\text{crack}} = 0.396$ mm^2 with maximum extension of 1.797 mm $\times$ 0.327 mm. The evaluation of the strain in the tangential (x) direction on the laser-loaded surface, obtained using the LIMESS stereo camera system, is presented in Figure 5.8a. The plot illustrates a linear accumulation of residual strains for at least the first 61 cycles. However, it should be noted that after cycle 61, the software evaluation no longer provides reliable results due to the exposure of the pure copper beneath the coating caused by high deformation. This leads to the loss of tracking of the speckle marks by the software. The slope of the fitted curve for tensile strains is $\dot{\varepsilon}_{\text{max,fit}} = 0.20\%$ per cycle, while the slope of the

fitted curve for compressive strains is $\dot{\varepsilon}_{\mathrm{min,fit}} = -0.42\%$ per cycle. Note that the values for $\dot{\varepsilon}_{\mathrm{max,fit}}$ and $\dot{\varepsilon}_{\mathrm{min,fit}}$ are locally averaged to account for measurement uncertainties. Figure 5.8b displays the spatial distribution of strain after cycle 60. It is evident that tensile strain accumulates above the central cooling channel, whereas compressive strain accumulates above the fillets adjacent to the central cooling channel.

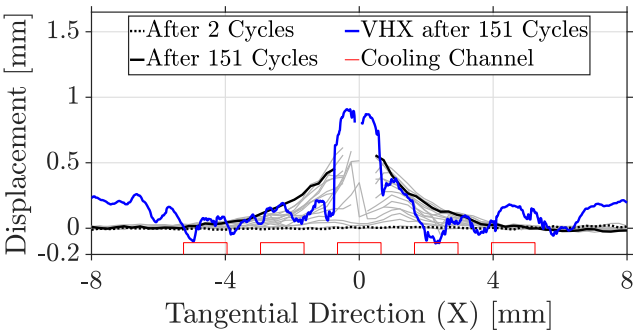

(a) Deformation of the laser loaded surface for every 10th cycle obtained with the LIMESS DIC system (gray, black curves). The blue curve shows the measurement obtained after the test campaign by the KEYENCE VHX-5000

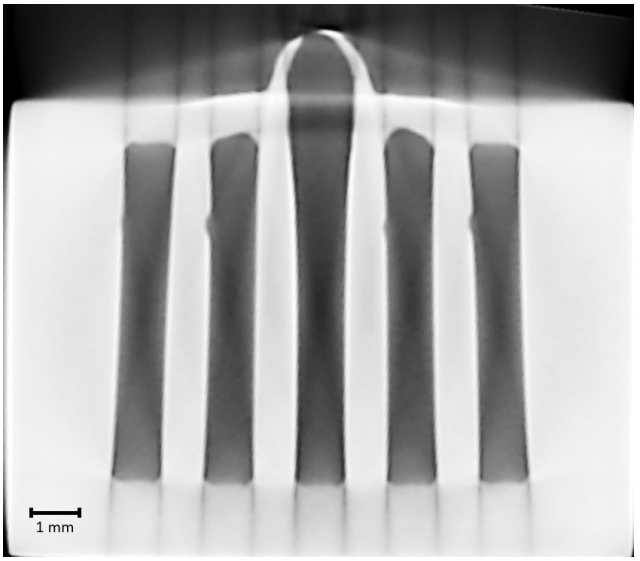

(b) CT-Scan of the TMF panel after the test.

Figure 5.7: Deformation of CP TMF panel

In general, it can be concluded that the material used in this study exhibits a remarkably high ductility at elevated temperatures, resulting in a deformation behavior akin to that of "bubble-gum". This deformation tendency becomes noticeable after approximately half of the cycles to failure have been completed. The experimentally determined useful fatigue life is determined to be 60 cycles.

5.2.2 Numerical Results

The presentation of the numerical results starts with the temperature distribution obtained from the coupled 3-dimensional fluid-thermal simulation in Figure 5.9. The cross section of the point of maximum temperature is shown. The scale is adapted to $T_{\mathrm{max}} = 900$ K in order to make it easier to compare with the temperature distributions of the other test cases (see Figures 5.17 and 5.25). This particular temperature distribution is applied to the 2-dimensional static structural analysis in ANSYS Mechanical as an input boundary condition. Figure 5.10 presents different intermediate steps and results in x-direction of the

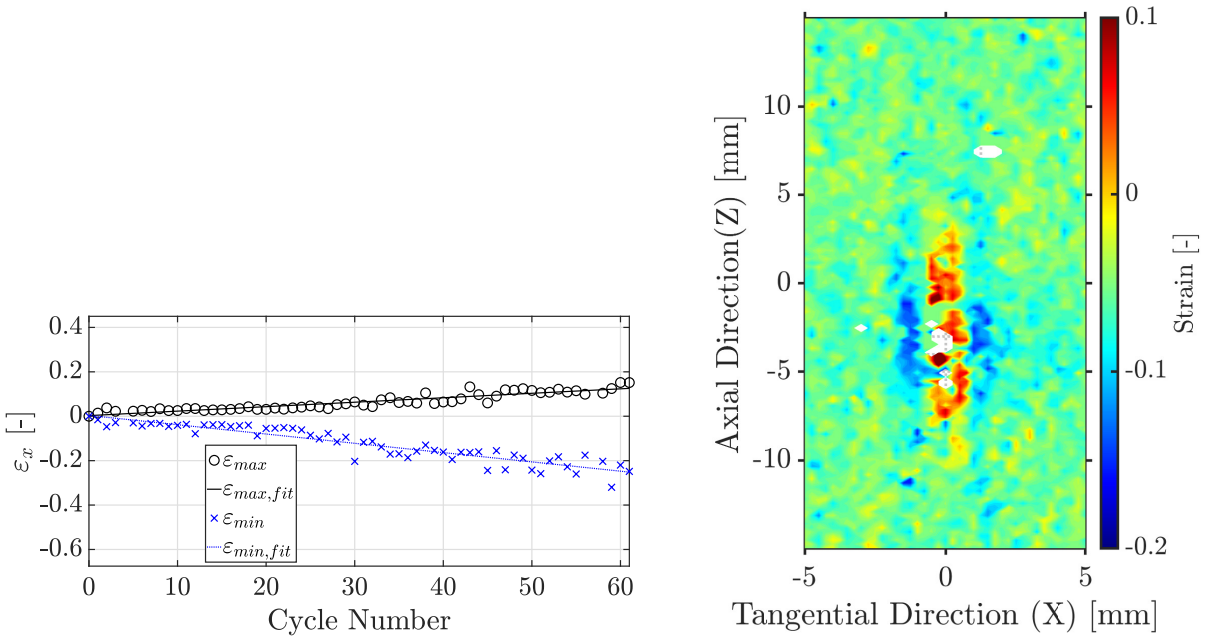

(a) Evolution of locally averaged maximum residual strain over the first 61 cycles as determined with the Limess system by DIC.

(b) Exemplary residual strain on the laser loaded surface after Cycle 60 around 40% of the overall number of cycles as determined with the Limess system by DIC.

Figure 5.8: Strain analysis of CP TMF panel

static structural analysis and the fatigue life analysis from post-processing in Matlab. Figure 5.11 shows the respective results in y-direction. Note that throughout this as well as the following sections, the left hand side always displays the results obtained by the simulation in Standard ANSYS Mechanical (SAM) while the right hand side is dedicated to the results obtained by the respective User Programmable Features (UPF). Additionally, the reader shall bear in mind that the residual plastic strain in the graphs is comprised of plastic strain and creep strain in the model in SAM while the UPF only uses plastic strain as no creep is incorporated in these models (see Chapter 4). Also note, that for all three test cases three nodes on the symmetry axis of the central cooling channel have been evaluated for their fatigue life as this is the characteristic failure point for the TMF panel. The location of these nodes are displayed in Figure 5.10a. In the figures presenting the numerical results subfigures (a), (b) show the distribution of strain in the respective direction after 5 cycles for Cu-HCP and after 10 cycles for CuCrZr. Their scale is again adapted to the maximum and minimum occurring strain in all simulations. Subfigures (c), (d) show the stress-strain-diagram obtained from subfigures (a), (b) for

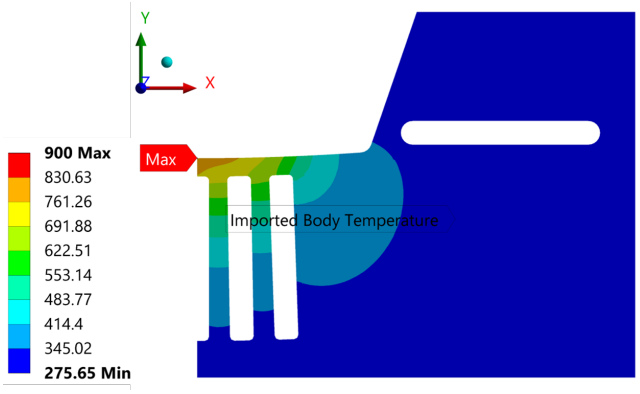

Figure 5.9: Temperature Distribution as obtained from coupled fluid-thermal analysis

Nodes 1-3. Finally, the damage evolution resulting from the post-processing tool developed in MATLAB is presented in Subfigures (e), (f) for the relevant Nodes 1-3.
Figures 5.10a to 5.10d indicate that the structural simulation with both the SAM model and the UPF deliver very comparable results regarding the distribution (e.g. compressive and tensile) and magnitude of strain after 5 cycles. While the strain around Node 1 is of compressive nature for the first cycle, this turns into tensile strain after the initial phase of the loading. Node 3 experiences compressive strains throughout the simulated time frame in both models used. A difference between the two approaches can be observed for Node 2. While for the results in SAM strains start as a compressive strain, the evolution tends towards tensile strains. Due to a very low slope of this progress, the hysteresis loop in Figure 5.10c seems to be rather static. In contrast the evolution of the strain for Node 2 obtained in the UPF simulation is purely compressive. Comparing the strain distribution for Node 1 and above the adjacent fillet of both models to the experimentally determined strain on the laser loaded surface in Figure 5.8 a good congruence can be observed. Around Node 1 tensile strain can be observed while the fillet is loaded with compressive strain in experimental and numerical results. Also the strain values at both locations are comparable for the same number of loading cycles. Figures 5.10e and 5.10f present the evolution of damage on Nodes 1-3 over the number of cycles. The damage evolution is dominated by the ductile damage portion. The brittle fatigue portion can be seen as the straight line following the abscissa. It has no influence on the total damage before the ductile damage kicks in at the cycle number where the damage threshold $\varepsilon_{\mathrm{th}}$ is reached. From there on, an exponential increase of total damage can be observed until failure. Failure occurs during the cycle number when the critical damage D_{cr} and critical strain $\varepsilon_{\mathrm{cr}}$

are met. The respective results for the fatigue life are on display in Table 5.1. It can be seen that at Node 3 the critical damage is hit after 49 cycles for the model in Standard ANSYS Mechanical and 55 cycles for the simulation using the UPF. It is important to note that reaching D_{cr} and $\varepsilon_{\mathrm{cr}}$ solely at Node 3 does not imply the crack of the overall TMF panel since the remaining nodes in the simulation are still intact. From an experimental point of view, this can be interpreted as the event where macro-crack initiation begins. Macro-crack initiation leads to an increasingly weakening structure where the remaining wall between cooling channel and laser loaded surface gradually fails. In the TMF panel test this can be interpreted as the previously described change from a concave to a convex deformation above the central cooling channel which occurred around the same number of cycles (see Figure 5.7a). This corresponds to 32 % (Standard ANSYS) and 36 % (UPF) of the experimental fatigue life. This is defined as the useful fatigue life of the simulation. According to the post processing analysis Node 2 reaches critical damage at 72 and 93 cycles respectively, followed by Node 1 after 167 and 147 cycles. Note that the damage evolution, crack initiation and its further development are not incorporated in the numerical simulation. Therefore, the fatigue life estimation of Node 1 and 2 does not take into account the weakened wall structure due to the crack initiation at Node 3. Hence, the fatigue life of these nodes is overestimated in comparison to a simulation that incorporates damage. Because the simulation is quasi-2-dimensional an evaluation of the damage based on the stress and strain results in y-direction was conducted. In previous work only the stress, strain and damage in x direction was considered [9, 159]. However, note that a factor for the triaxiality is already implemented in the damage models (see Equation (2.29)). The results are shown in Figure 5.11 and Table 5.1. When comparing Figures 5.10a and 5.10b with Figures 5.11a and 5.11b it comes to mind that the sign of the strain at the same node is inverted. Comparing Figures 5.10c and 5.10d with Figures 5.11c and 5.11d one can seen that for the latter in the y-direction almost no stresses can be observed but the strain amplitude in each cycle is higher. The increased strain amplitude leads to a much shorter fatigue life result obtained by the post-processing tool as the ductile damage hits the critical damage D_{cr} even faster. This results in a number of cycles of only 23 to 26 for Node 3 and 40 and 54 for Node 1 (see Table 5.1) respectively. Therefore a sole consideration of the damage in y-direction provides a strong underestimation of the fatigue life.

	SAM			UPF			Exp
Node	**1**	**2**	**3**	**1**	**2**	**3**	
x-direction	167	72	49	147	93	55	151
y-direction	54	42	26	40	31	23	

Table 5.1: Fatigue life results of the Cu-HCP Central Point analysis

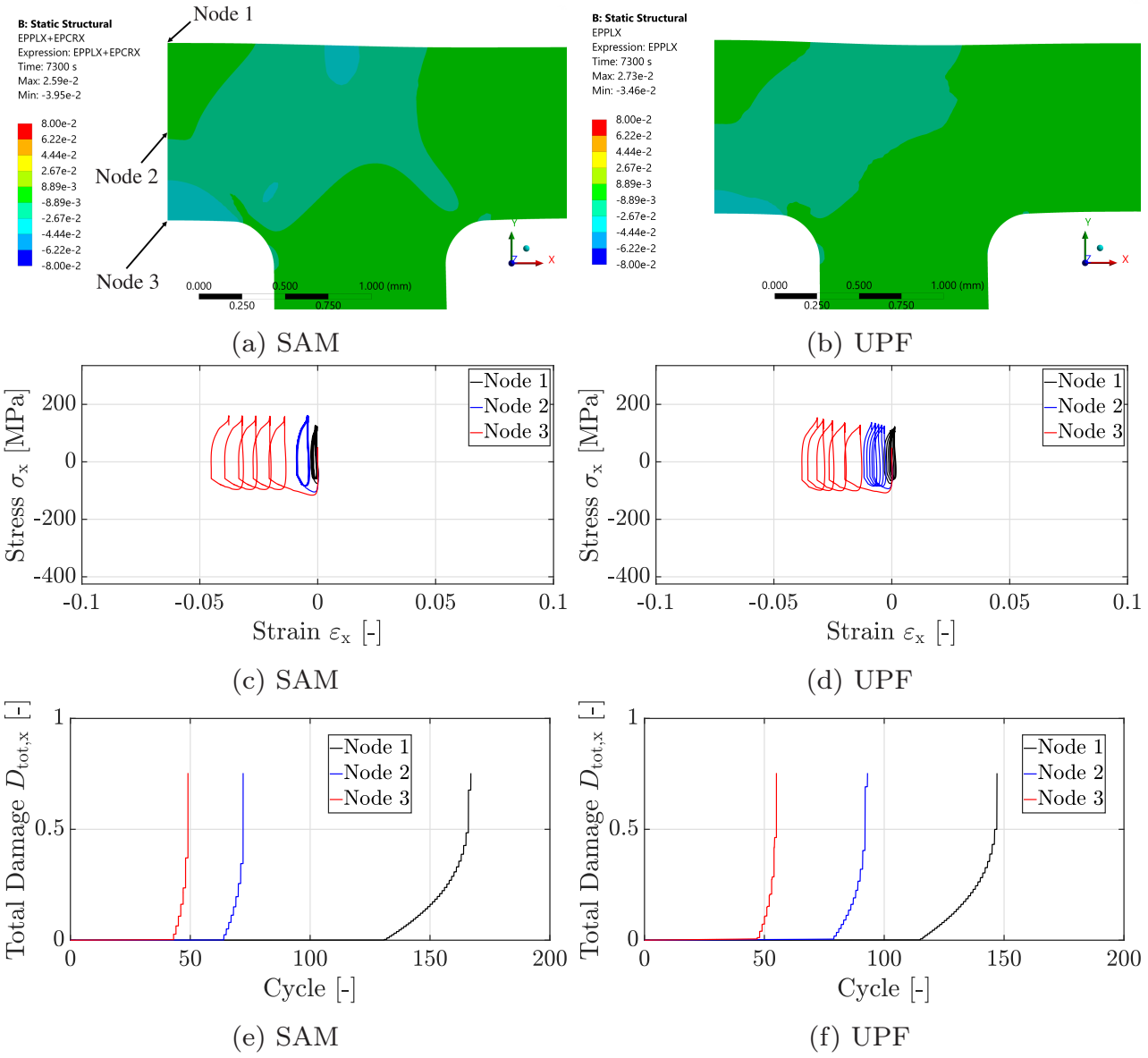

Figure 5.10: Fatigue life results of CP simulation in x-direction

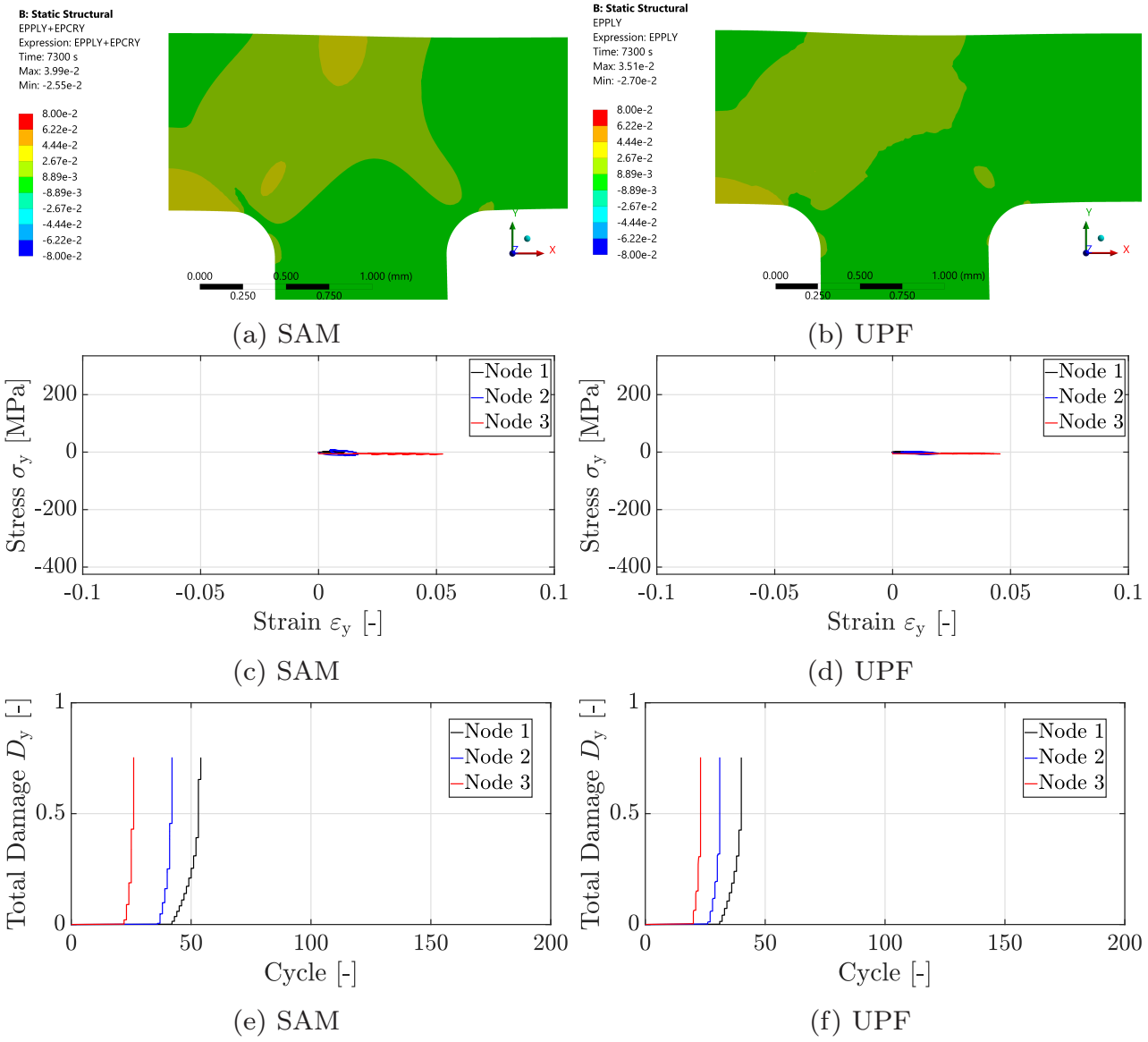

(a) SAM (b) UPF

(c) SAM (d) UPF

(e) SAM (f) UPF

Figure 5.11: Fatigue life results of CP simulation in y-direction

5.3 Temperature Variation

For the temperature variation (TV) TMF panel test the surface temperature is increased to $T_s = 900$ K. The heat flux and laser holding time were kept constant. Hence, the test conditions are $T_s = 900$ K, $q_w = 24.25$ MW/m^2 and $t_{on} = 200$ s.

5.3.1 Experimental Results

The TMF panel in the TV test campaign ruptured at the beginning of the 133rd cycle. This equals 88.1% of the CP TMF panel fatigue life.

Fluid Conditions

Figure 5.12 shows the fluid conditions of the central cooling channel during the test campaign. For maintaining a surface temperature of $T_s = 900$ K in the temperature variation TMF panel test the mass flow rate is approximately 18.3% less compared to the CP TMF panel test with a surface temperature of $T_s = 800$ K. Over the course of the test, the development of the mass flow rate for CP and TV are comparable, i.e. also for the TV campaign the mass flow rate had to be increased until the mid-test before it needed to be decreased again. However, for the last 10 cycles, a sharp increase in mass flow rate could be observed. The range of the total mass flow rate is $\dot{m}_{tot} = 210.7$ g/s to $\hat{\dot{m}}_{tot} = 242.0$ g/s. The initial mass flow rate was $\dot{m}_{tot} = 211.3$ g/s which is $\Delta\dot{m}_{tot} = 6.4$ g/s (or 2.9%) lower than calculated from the results of the HTT panel test (see Fig. 5.1a). It is expected that the same processes as already observed during the CP TMF panel test, degradation of thermophysical parameters, thinning of the cooling channel wall and an increasing cross section of the cooling channel lead to the necessary adjustments of the mass flow rate. Throughout the test campaign the outlet temperature in Figure 5.12b shows no significant trend but stays rather constant around $T_{4,out} = 185.5^{+4.6}_{-3.7}$ K. This is an average rise of $\Delta T_{out} = 25.5$ K from initial conditions at the start of the cycle to steady state conditions and a difference of $\Delta T_{out,CP,TV} = 4.7$ K to the central point conditions. The fluid inlet and outlet pressure (see Fig. 5.12c) rises by an average of $\Delta p_{in,out} = 8.5$ bar, an increase of $\Delta p_{out,CP,TV} = 1.0$ bar when compared to the CP TMF panel test. The range of the pressure is $p_{4,out} = 63.5^{+2.2}_{-2.0}$ bar. The balance of energy shows the same results for the CP and TV, i.e. in both test cases an amount of approximately 5.2% of the energy input by the laser is not comprised in the coolant at the exit of the panel. Figure 5.12 presents the fluid conditions for the representative cycles 1,

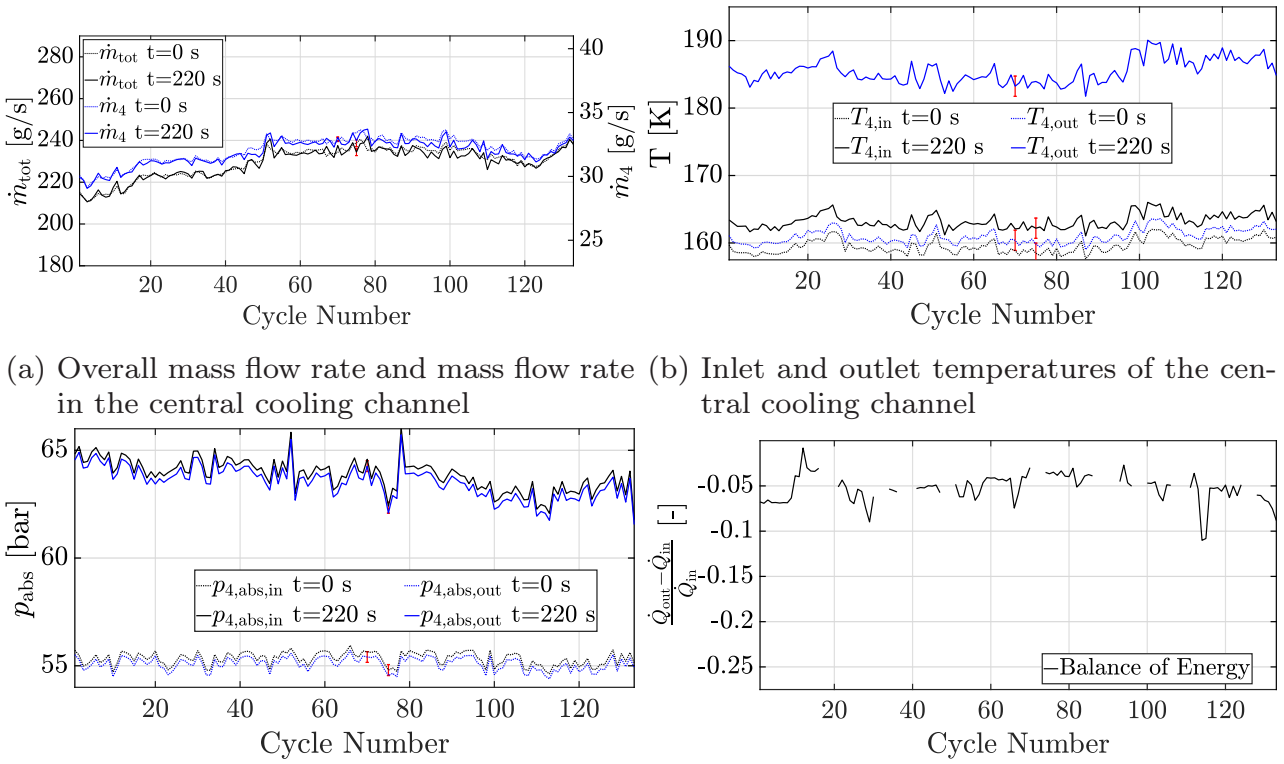

(a) Overall mass flow rate and mass flow rate in the central cooling channel

(b) Inlet and outlet temperatures of the central cooling channel

(c) Inlet and outlet pressure of the central cooling channel

(d) Balance of energy for temperature variation

Figure 5.12: Fluid conditions for temperature variation

66 and 133. Similar to the CP test campaign, the appearance of the crack is very well visible in the graphs for cycle 133. It occurred around $t_{133} = 87.5$ s. While the mass flow rate (see Fig. 5.13a), fluid temperature (Fig. 5.13b) and absolute pressure (Fig. 5.13c) show a normal similar performance in all cycles, the pressure difference for cycle 133 in Figure 5.13d appears differently. The maximum Δp is reached at $t = 28$ s before the laser is at the desired power level. Subsequently the slope of the curve is constant negative until the crack occurs. Also, this can not be observed in the remaining cooling channels. Hence, it is assumed that the initial crack already occurs at $t = 28$ s gradually extending until it becomes visible in the IR camera images and plots in Figure 5.13. The laser was switched off at $t = 103.7$ s. In the aftermath, as also observed in the CP test campaign, a backflow of the coolant from the merger towards the crack, as the Δp reaches a negative value. From Figure 5.13a the variation in mass flow rate during ramp-up and ramp-down is determined to $\Delta\dot{m}_{tot} = ^{+3.6}_{-2.5}$ g/s.

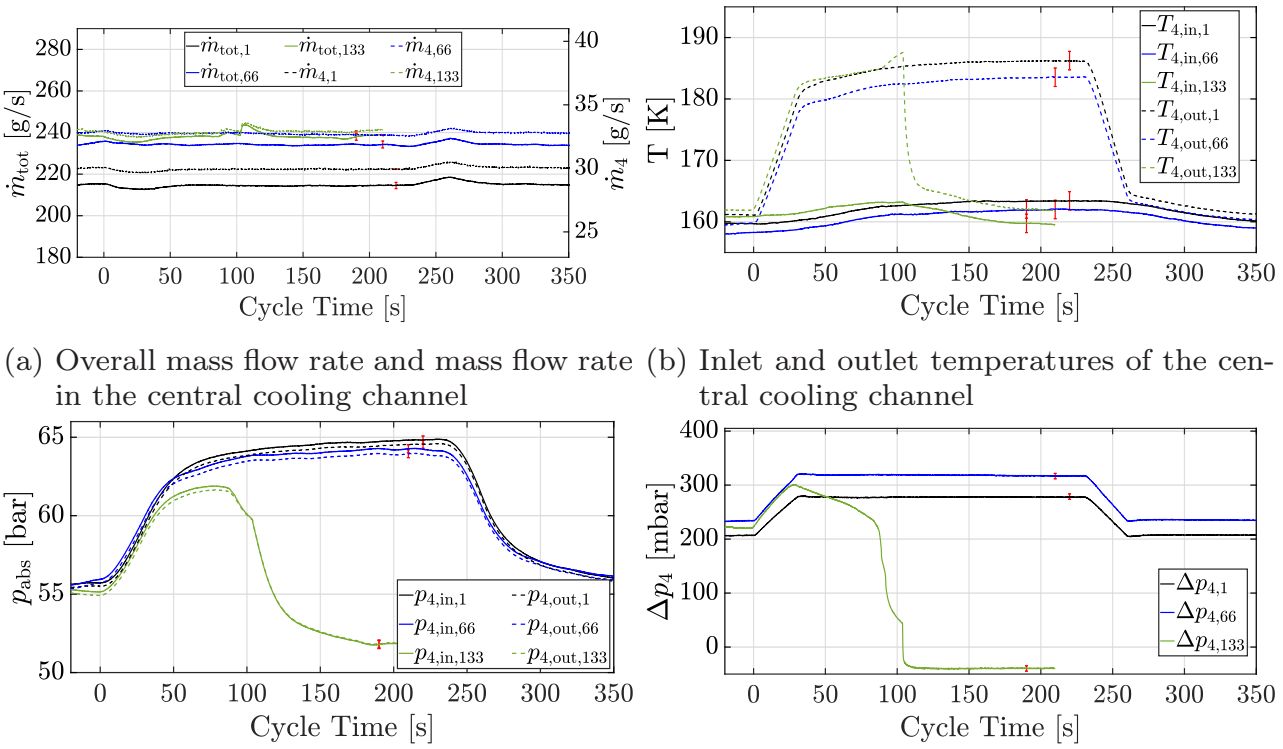

(a) Overall mass flow rate and mass flow rate in the central cooling channel

(b) Inlet and outlet temperatures of the central cooling channel

(c) Inlet and outlet pressure of the central cooling channel

(d) Pressure difference in the central cooling channel

Figure 5.13: Fluid conditions for temperature variation at representative Cycles 1, 66, and 133

Mechanical Observations

Figure 5.14 highlights the development of the temperature distribution on the laser loaded surface for the cycles 1, 66 and 133. A similar performance as for the CP TMF panel test campaign can be observed. Already at cycle 66 a minor cold region can be detected right above the central cooling channel accompanied with the hottest regions directly above the adjacent fillets. This indicates the beginning of thinning of the cooling channel and material being moved towards the fillets. Worth noting also is the irregular temperature distribution above the central cooling channel in cycle 133 with cold spots around $z = 5$ mm, $z = -5$ mm and $z = -10$ mm when compared to cycle 151 in Figure 5.6. This might indicate a non-uniform development of the thinning of the cooling channel wall beneath the surface. However, the crack occurs at the same position for both test cases. In Figure 5.15a the development of the deformation as obtained by the DIC for every 5^{th} cycle and the final deformation obtained by the microscope KEYENCE VHX-5000 are shown. Note that the DIC produced reasonable results only until cycle 74 because afterwards the

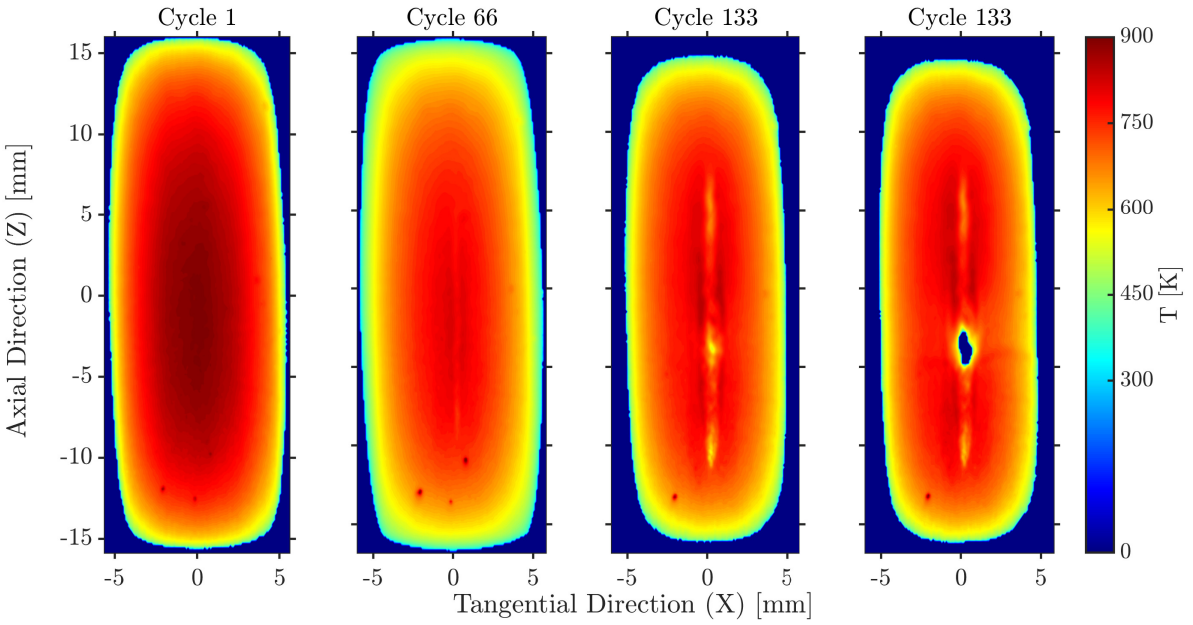

Figure 5.14: Temperature distribution of the laser loaded surface for Temperature Variation test campaign retrieved from the IR camera measurements for cycles 1, 66, and 133 directly before and after occurrence of the crack. Flow direction is top-down.

speckle marks on the TMF panel surface could not be tracked any more due to high deformation. The grey lines indicate that the deformation already starts in the very first cycles. As already mentioned, bulging above the fillets next to the central cooling channel can be observed right from the beginning of the test campaign. The bulging entails a small concave region above the central cooling channel. This cavity increases until cycle 40. Afterwards a sudden change to a convex surface occurs leading to the already known "bubble-gum"-like performance until the crack occurs. The final deformation is $\Delta\hat{y}_{\mathrm{TV}} = 1.63$ mm, an increase of 79.2% as observed for the final deformation of the CP test campaign. The final crack has an irregularly shaped area of $A_{\mathrm{crack}} = 0.911$ mm^2 with maximal extensions of 2.470 mm $\times$ 0.706 mm. Figure 5.15b shows a CT scan of the damaged cross section after the test campaign. Unfortunately, the image does not show the final bubble due to bad quality of the CT scan, though it is displayed here for the sake of completeness. However, clearly a void is perceptible above the central cooling channel. The residual strain in tangential (x) direction after each cycle up to cycle 61 is presented in Figure 5.16a. After cycle 61 the DIC did not yield any reasonable results. The residual tensile strain again increases linearly, analogous to the tensile strain in the CP test campaign, with a strain rate of $\dot{\varepsilon}_{\mathrm{max,fit}} = 0.71\%$ per cycle. This is an increase

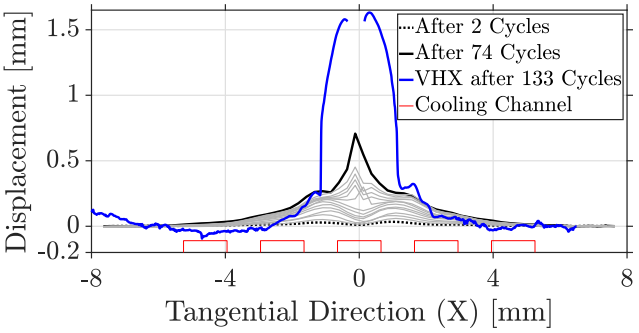

(a) Deformation of the laser loaded surface for every 5$^{\text{th}}$ cycle obtained with the LIMESS DIC system (gray, black curves). The blue curve shows the measurement obtained after the test campaign by the VHX-5000. The red lines indicate the position of the cooling channels.

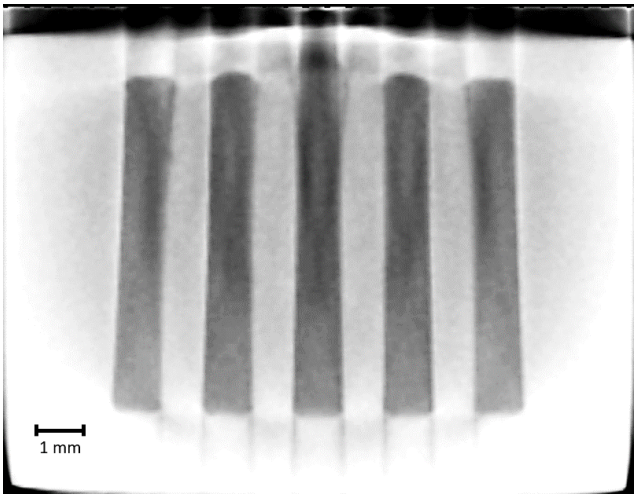

(b) CT-Scan of the TMF panel after the test.

Figure 5.15: Deformation of TV TMF panel

by 355% compared to the CP. Conspicuously, the compressive strain rate increases to a level of $\varepsilon_{\text{min}} = 0.081\%$ within the initial 5 cycles but then stays constant up to approximately cycle 42. Afterwards a steep increase in the compressive strain rate can be observed. Figure 5.16b presents the corresponding distribution of the strains on the TMF panel surface after cycle 54 (40% of test duration) to make the results comparable to Figure 5.8b. Similarly to the CP test campaign the tensile strains accumulate right above the central cooling channel while the compressive strains accumulate over the adjacent fillets. Conclusively, the experimental results of the temperature variation TMF panel test campaign show an even higher ductility of the material when the temperature is further increased. This is evident by the much higher final deformation as well as the highly increased strain rate though the fatigue life is decreased to 88.1% of the CP TMF panel.

5.3.2 Numerical Results

Similar to the numerical results of the Central Point test case, firstly the temperature distribution obtained from the coupled fluid-thermal simulation is presented in Figure 5.17. As expected, the elevated temperature inside the TMF panel spreads to a wider area. Again, this temperature distribution is used as input for the static structural analysis. The strain distribution after 5 cycles is shown in Figures 5.18a and 5.18b. When compared to the strain distribution of the CP test case, one recognizes that the sign of the strain is mainly

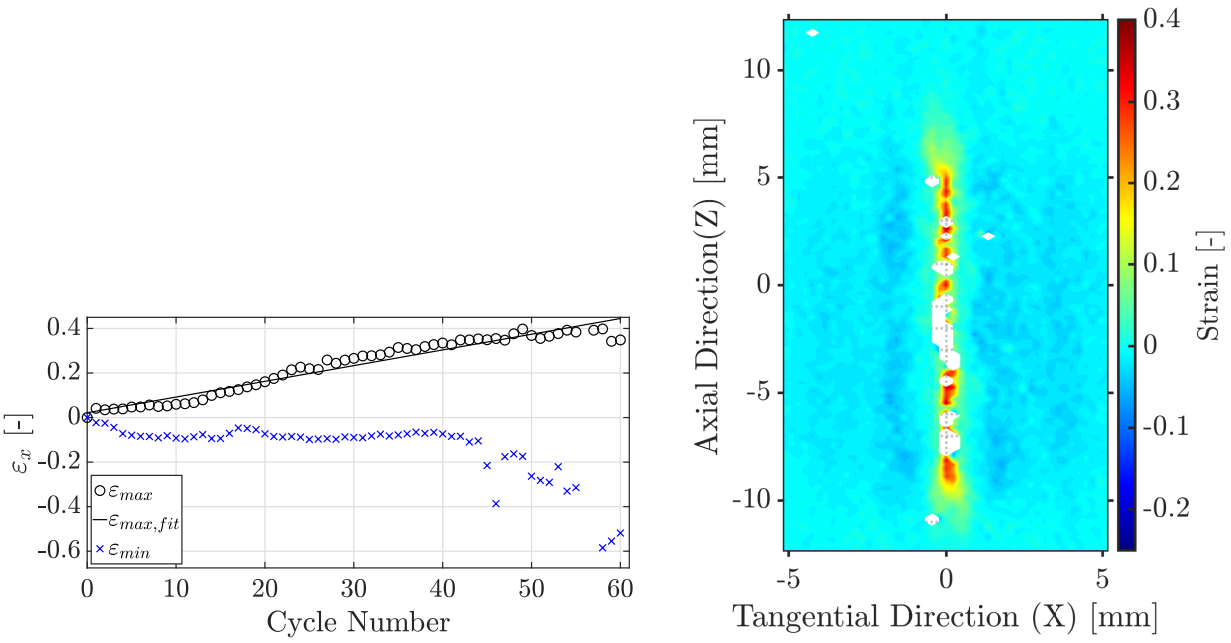

(a) Evolution of locally averaged maximum residual strain over the first 61 cycles as determined with the Limess system by DIC.

(b) Visible residual strain on the laser loaded surface after Cycle 54 around 40% of the overall number of cycles as determined with the Limess system by DIC.

Figure 5.16: Strain analysis of TV TMF panel

the same for each node/element but the magnitude is increased. This is also an expected result and in accordance with experimental observations. Due to the higher temperature levels throughout the relevant area of the TMF panel the material parameters decrease strongly i.e. the material becomes more ductile. Additionally, the temperature gradient is higher which similarly increases the gradient in thermal expansion leading to higher strains. Comparing the numerical results to the experimentally measured strain distribution on the laser loaded surface in Figure 5.16b yields a good congruence for tensile strain at the location of Node 1 and compressive strain above the adjacent fillet. Note that Node 1 is in the compressive range of strain but the overall residual strain at the end of each cycle clearly trends towards tensile strain as can be seen in Figures 5.18c and 5.18d. The strain amplitude in each cycle is increased for Nodes 1-3 but most significantly for Node 3 in both numerical models used. Consequently, the fatigue life prediction obtained from the post processing tool decreases most significantly for Node 3 to 25 cycles according to the simulation using Standard ANSYS Mechanical and 28 cycles obtained for the UPF as shown in Table 5.2. In both cases, this is only half the number of cycles

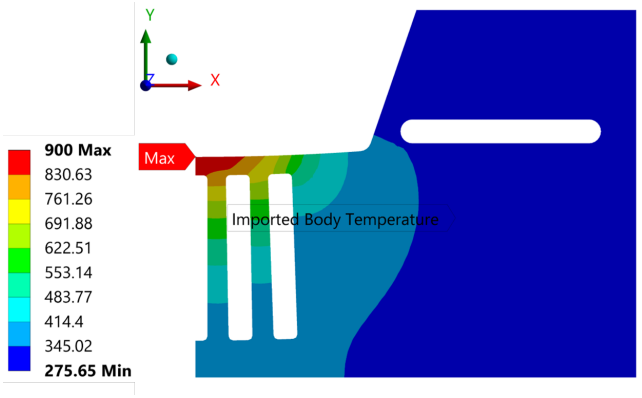

Figure 5.17: Temperature Distribution as obtained from coupled fluid-thermal analysis

compared to Node 3 in the CP test case. Again this event can be interpreted as transition point between concave and convex deformation on the surface over the central cooling channel as depicted in Figure 5.15a. This corresponds to 19 % (SAM) and 21 % (UPF) of the TV TMF panel experimental fatigue life. The fatigue life prediction of Node 2 yields 49 and 56 cycles, respectively. For Node 1 the fatigue life results diverge by almost 20 % between SAM and UPF. While the model used with the data from the simulation with Standard ANSYS Mechanical yields 160 cycles, hence, over-predicts the fatigue life strongly, the UPF yields 129 cycles. Again, bear in mind that the simulation in ANSYS is decoupled from the damage calculation. The results for the fatigue life analysis in y-direction are shown in Figure 5.19 and Table 5.2. Similarly to the results in y-direction for the CP test case, almost no stress can be observed but large strains are present. Again, the fatigue life is highly underestimated.

	SAM			**UPF**			**Exp**
Node	**1**	**2**	**3**	**1**	**2**	**3**	
x-direction	160	49	25	129	56	28	132
y-direction	33	22	9	30	20	13	

Table 5.2: Fatigue life results of the Cu-HCP Temperature Variation analysis

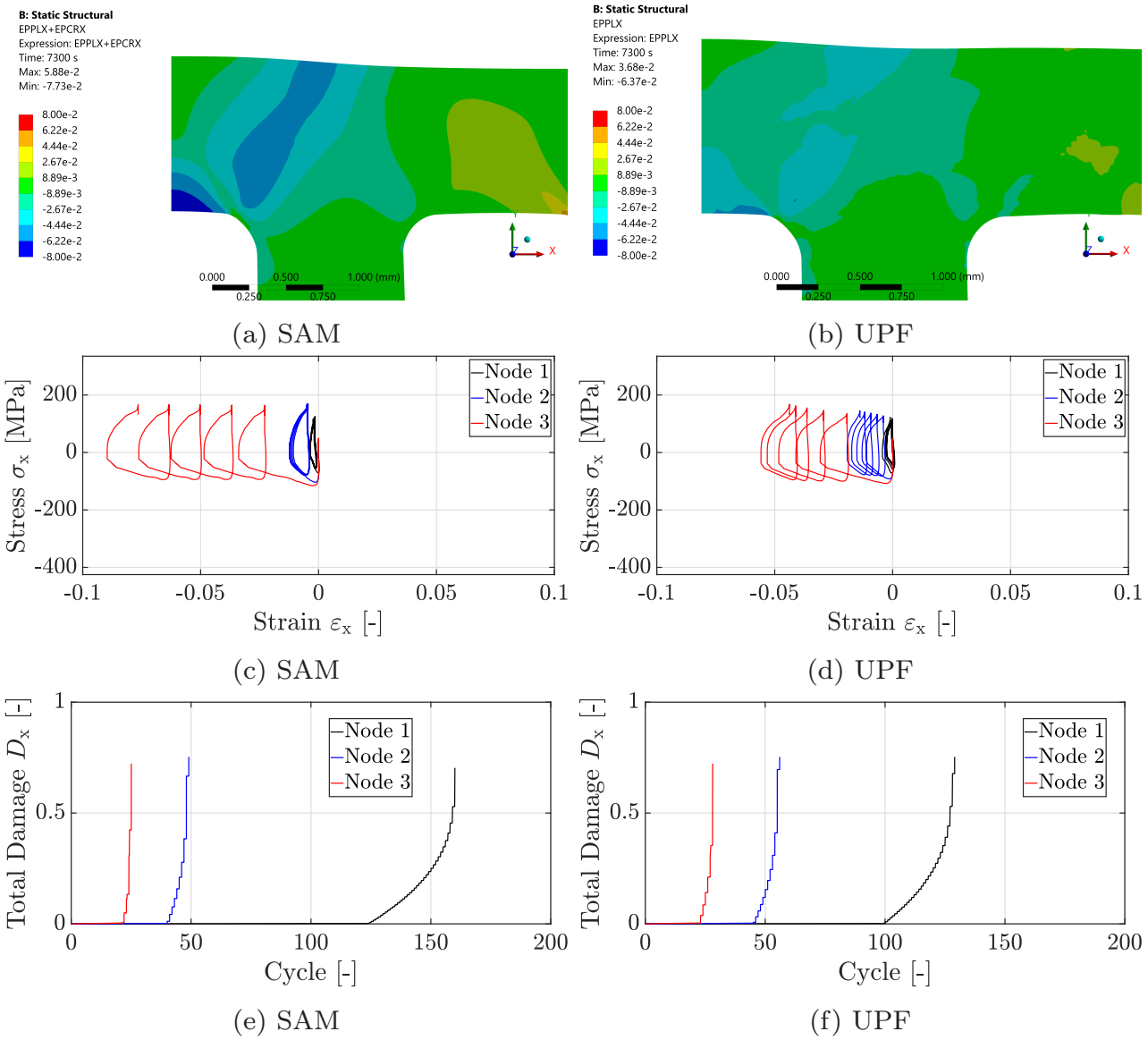

(a) SAM (b) UPF

(c) SAM (d) UPF

(e) SAM (f) UPF

Figure 5.18: Fatigue life results of TV simulation in x-direction

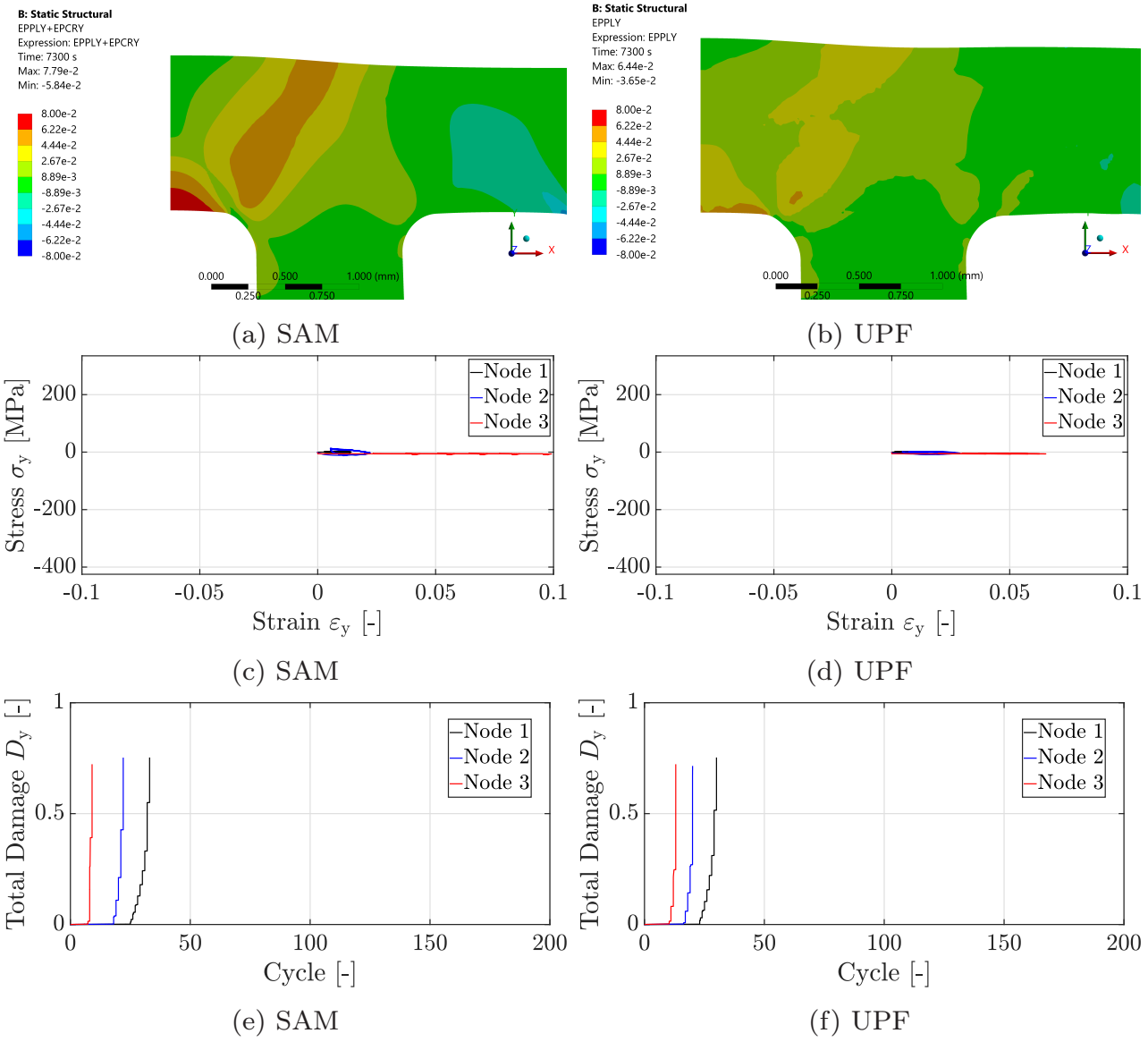

(a) SAM (b) UPF

(c) SAM (d) UPF

(e) SAM (f) UPF

Figure 5.19: Fatigue life results of TV simulation in y-direction

5.4 Material Variation - CuCrZr

This section presents the results of the fatigue life analysis for the material variation (MV) of CuCrZr. The test conditions are similar to the central point conducted with Cu-HCP $T_s = 800$ K, $q_w = 24.25$ MW/m^2 and $t_{on} = 200$ s.

5.4.1 Experimental Results

In contrast to the previously presented experimental results the TMF panel made from CuCrZr ruptured during the ramp-down or post-cooling after the 645th cycle. This represents 427.1% of the central point TMF panel fatigue life. The exact time could not be determined because the crack is too small to be detected in the plots for pressure difference or mass flow rate. It could only be detected by a tiny cold spot on the IR thermal field when the maximum surface temperature was about $T_s = 310$ K.

Fluid Conditions

For the same heat flux and surface temperature as the central point, the CuCrZr TMF panel requires approximately 25% less coolant compared to Cu-HCP (Figure 5.20a). However, this lower mass flow rate results in a higher outlet temperature of the coolant at steady state conditions ($t_{on} = 220$ s) for CuCrZr, as evident in Figure 5.20b. The coolant outlet temperature rises by an average of $\Delta T_{4,out} = 26.4$ K to $\Delta T_{4,out} = 186.4^{+6.8}_{-7.8}$ K That is an increase of $\Delta T_{4,out,CP-MV} = 5.7$ K compared to the CP. The inlet temperature increases by $\Delta T_{4,in} = 3.4$ K to $T_{4,in} = 163.4^{+4.4}_{-4.7}$ K. The inlet and outlet pressure increase by $\Delta p_{4,in,out} = 8.7$ bar to an absolute outlet pressure of $p_{4,in} = 63.9^{+2.0}_{-2.0} \pm 2.1$ bar and $p_{4,out} = 63.7^{+2.0}_{-2.0} \pm 2.1$ bar (Fig. 5.20c). Both, outlet temperature and pressure again do not show a clear trend during the test campaign. This outcome contradicts the initial expectations. Considering that Cu-HCP exhibits a higher thermal conductivity than CuCrZr, (see Fig. 4.5), according to Fourier's law (Eqn. (2.37)) one would anticipate a higher temperature on the fluid side for Cu-HCP. Consequently, a lower mass flow rate should be required for energy transport in the Cu-HCP panel since the convective heat flow rate is influenced by the temperature difference between the wall temperature T_w and the bulk temperature of the fluid T_b (Eqn. (2.38)). Additionally, the balance of energy in Figure 5.20d for the CuCrZr TMF panel shows that around 18% of the incoming energy is not transported outward in the coolant. An even bigger discrepancy of the mass flow rate could be observed in the results published by Kringe in 2020 [10] comparing the

CuCrZr TMF panel test with a maximum surface temperature of $T_s = 1000$ K to the results presented for the Cu-HCP made HTT panel test (Section 5.1) for $T_s = 1000$ K. For these test campaigns the initial total mass flow rates were $\dot{m}_{tot,CuCrZr} = 110$ g/s and $\dot{m}_{tot,Cu-HCP} = 175$ g/s. However, the mass flow rate for CuCrZr at $T_s = 1000$ K had to be increased significantly during the course of the test to $\dot{m}_{tot,CuCrZr} > 212.5$ g/s supporting the decrease of thermal conductivity (see Section 5.5). In order to resolve this discrepancy in mass flow rate several factors were examined. Firstly, the roughness of the coating of the CuCrZr and Cu-HCP TMF panels was compared, as an increased roughness implies an increased absorption of heat provided by the laser. However, no difference could be observed. Secondly, the thickness of the individual coatings was analyzed but again no deviation could be observed. Also the roughness of the cooling channel walls is almost similar (see Table 3.3), hence, can be excluded as a source of the observed deviation. In contrast to Cu-HCP at the same test conditions, the total mass flow rate remains rather constant to maintain the surface temperature of $T_s = 800$ K. It had to be slightly increased during the first 100 cycles, followed by a minor decrease until the middle of the test duration around cycle 322 where a minimum is observable. From here on, the mass flow rate was increased again but still only minor changes were applied. The mass flow rate spans between $\dot{m}_{tot} = 183.3$ g/s and $\hat{\dot{m}}_{tot} = 206.5$ g/s. It is assumed that again during the first 100 cycles the thermophysical parameters, particularly λ, decrease so the mass flow rate had to be increased. As later (see Section 5.4.1) will be seen, the cross section of the cooling channel does not increase significantly compared to the Cu-HCP panel tests. Additionally, no significant thinning of the channel wall could be observed. Hence, the mass flow rate was not decreased at the end of the test campaign. As representative cycles for the CuCrZr fluid conditions Cycles 4, 322 and 645 are presented in Figure 5.21. Cycle 4 was chosen because cycles 1 to 3 were used to regulate the mass flow rate to the exact value to achieve the intended test conditions since no HTT panel for CuCrZr was available. As mentioned earlier, the crack of the central cooling channel occurred after cycle 645 and could not be detected by the fluid conditions as the mass flow rate and pressure loss through the tiny hole was too small. From Figure 5.21a can be seen that the mass flow rate at laser ramp-up and ramp-down vary with the same amount of $\Delta\dot{m}_{tot} = \pm 3$ g/s as for the Cu-HCP panel.

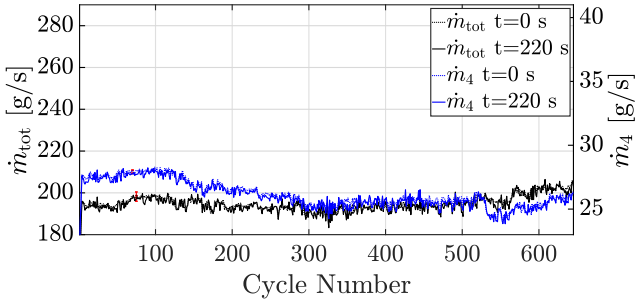

(a) Overall mass flow rate and mass flow rate in the central cooling channel for material variation

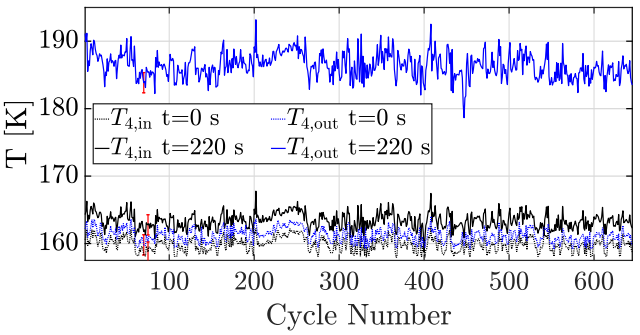

(b) Inlet and outlet temperatures of the central cooling channel for material variation

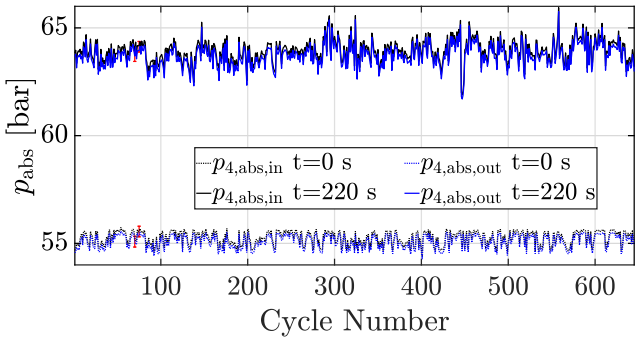

(c) Inlet and outlet pressure of the central cooling channel for material variation

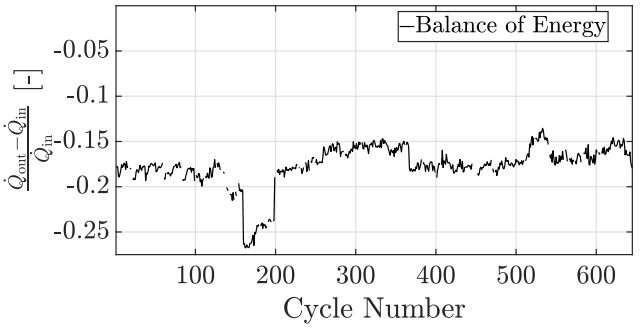

(d) Balance of energy for material variation

Figure 5.20: Fluid conditions for material variation

Mechanical Observations

In contrast to Figure 5.6 the IR thermal field of the MV TMF panel test for the cycles 1, 322 and 645 in Figure 5.22 does not show a significant change until the end of the test campaign. The area of observable temperature ($T > 273$ K) distribution becomes slightly smaller but no cold region above the central cooling channel indicating any thinning of the wall is visible. As mentioned, during the ramp-down or cool-down phase, the occurrence of cracking was observed for CuCrZr. As a result, Figure 5.22 far right was captured after the cycle with minimal laser power and a maximum temperature of $T_s = 308$ K, to assess whether the TMF panel had already developed cracks. The crack is visible as the cold spot in the center because of supercritical nitrogen flowing out. Figure 5.23a shows the progress of deformation of the cross section of the laser loaded surface for every 25th cycle obtained by the LIMESS DIC. The blue line indicates the final deformation as measured with the optical KEYENCE VHX-5000 microscope. The final deformation is, compared to Cu-HCP, very small, i.e. the maximum value is $\Delta\hat{y}_{MV} = 0.44$ mm which corresponds to 48.3% of total

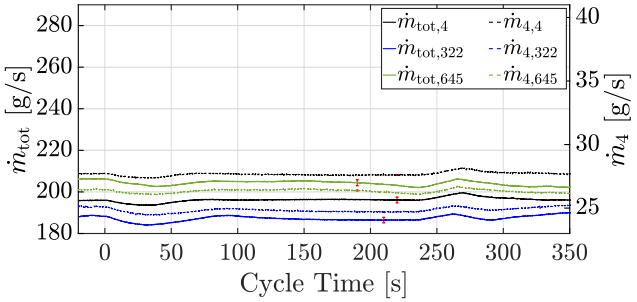

(a) Overall mass flow rate and mass flow rate in the central cooling channel for material variation

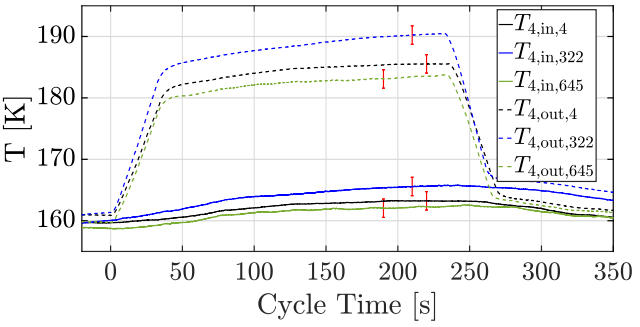

(b) Inlet and outlet temperatures of the central cooling channel for material variation

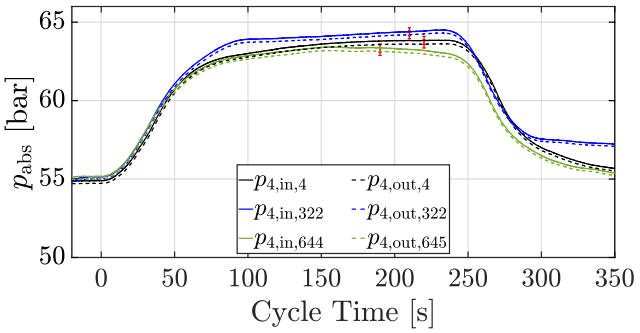

(c) Inlet and outlet pressure of the central cooling channel for material variation

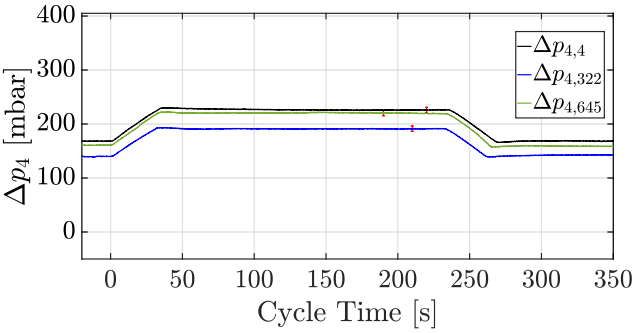

(d) Pressure difference in the central cooling channel

Figure 5.21: Fluid conditions for material variation at representative Cycles 4, 322 and 645

deformation of the central point TMF panel. Because of the small deformation the DIC could even track the last cycle so that a good congruence between the measurements of DIC and VHX can be observed. Also important to note is the non-linear progress of deformation. This becomes evident as the gray lines representing the majority of the deformation measurements are located close to each other, while a few lines towards the end of the test show increasing distance, hence deformation. In Figure 5.23b a CT scan of the cross section incorporating the crack is shown. Herein only little thinning of the cooling channel wall can be observed. The crack also appears to be a straight line stretching from the fluid side to the laser loaded side across the wall. This indicates a very brittle behavior of the material. Furthermore, the crack is not located on the line of symmetry, it is slightly shifted to the right. This shift can also be seen in the cavity that has developed close to the symmetry line in Figure 5.23a directly above the right half of the central cooling channel. Figure 5.24a presents the results for the development of strains in tangential (x) direction on the laser loaded surface obtained by the LIMESS DIC system. For

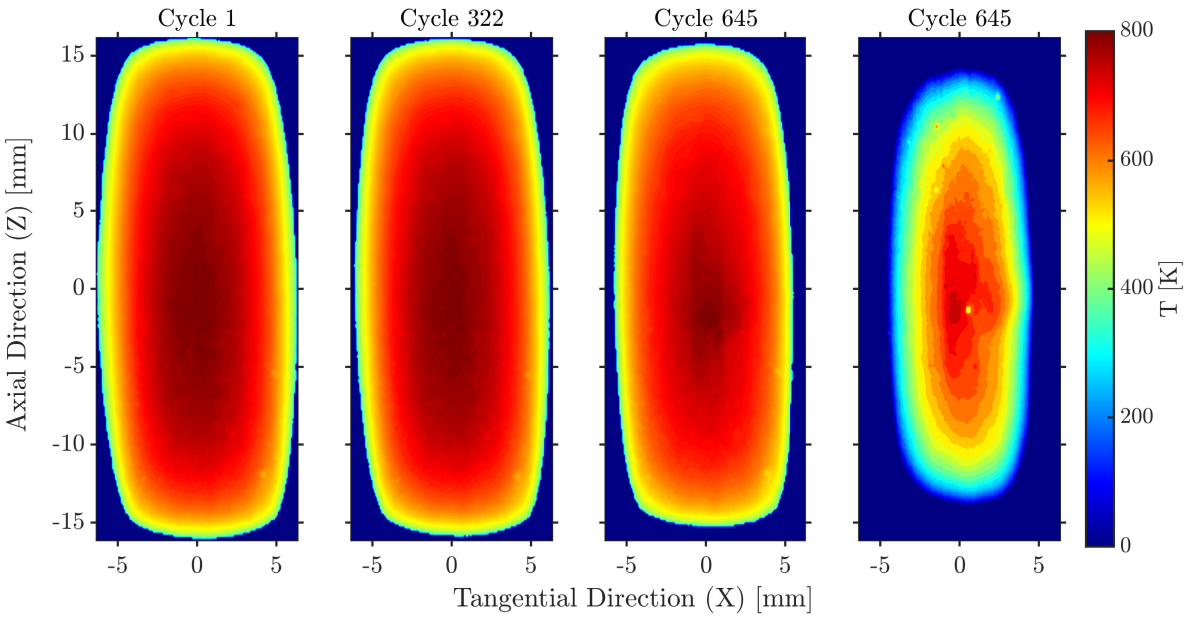

Figure 5.22: Temperature distribution of the laser loaded surface for Material Variation test campaign retrieved from the IR camera measurements for cycles 1, 322, and 645 directly before and after occurrence of the crack. Flow direction is top-down.

CuCrZr, it appears that within the initial 5 cycles, a strain of $\varepsilon_{5,\max} \approx 1.5\%$ and $\varepsilon_{5,\min} \approx -3.0\%$ is developing, but it remains constant for approximately 280 cycles, indicating some shakedown of the cyclic elasto-plastic deformation. However, after cycle 360, an exponential increase in tensile and compression strain is observed. The rate of increase is much higher for the compressive strains. However, similar to Cu-HCP (see Fig. 5.8b), tensile strains develop over the central cooling channel, while compressive strains are found over the adjacent fillets as shown in Figure 5.24b after 40% of the overall number of cycles. Due to technical limitations unfortunately for cycles >160 only a limited number of data points are available. The experimentally determined useful fatigue life is set to 360 cycles as up to this point deformation and plastic strains are very limited.

5.4.2 Numerical Results

The temperature distribution of the CuCrZr material variation test case is displayed in Figure 5.25. It is scaled to $T_{\max} = 900$ K for comparability. In contrast to the temperature distribution of the Cu-HCP TMF panel test case elevated temperatures are limited to the area beneath the laser loaded surface.

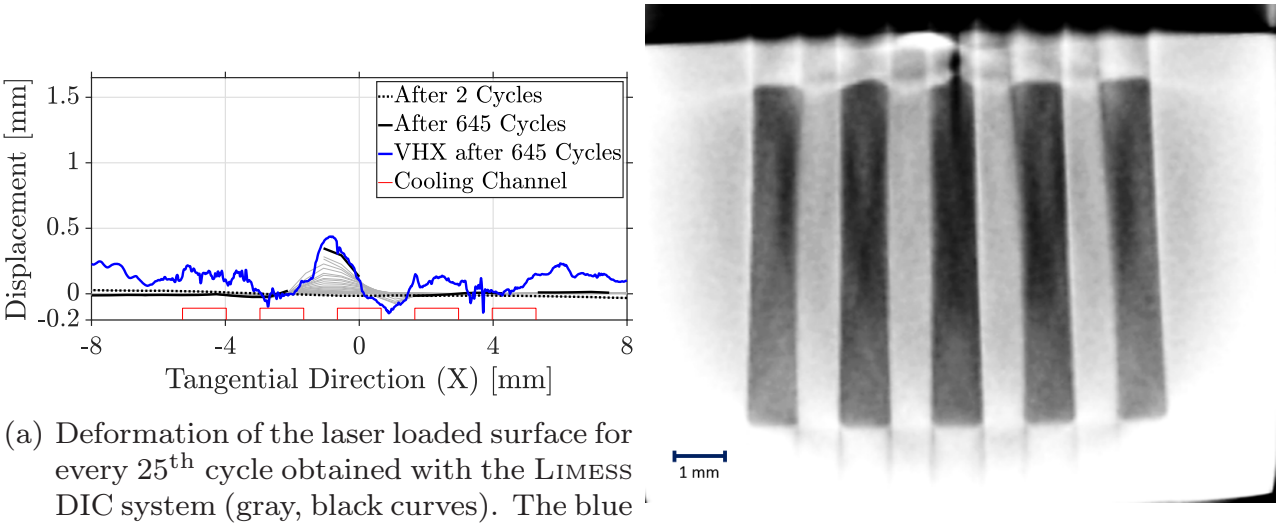

(a) Deformation of the laser loaded surface for every 25th cycle obtained with the Limess DIC system (gray, black curves). The blue curve shows the measurement obtained after the test campaign by the VHX-5000

(b) CT-Scan of the MV TMF panel after the test campaign

Figure 5.23: Deformation of MV TMF panel

This is caused by the reduced thermal conductivity of CuCrZr when compared to Cu-HCP (see Figure 4.5). Generally, this increases the thermal gradient in the relevant region of the TMF panel but it is opposed by more stable mechanical material parameters for cooler temperatures. As for previous test cases the resulting strain is shown in Figures 5.26a and 5.26b. Note that for CuCrZr the results after the simulation of 10 cycles are displayed as the strains are very low. The scale is adapted to the overall maximum and minimum of all test cases examined in this work for comparability. In Figures 5.26c and 5.26d the stress-strain relation is displayed. Herein a major difference between the simulation in Standard ANSYS Mechanical and the UPF becomes apparent. While for the former simulation the strain accumulates only towards compressive loading for Nodes 1-3, the strains in the UPF all tend to compressive strains in the first 5 cycles but after that the accumulation of each cycle ends with a positive, hence tensile, contribution for all nodes. Consequently, the results obtained by the simulation in Standard ANSYS mechanical for Node 1 and above the adjacent fillet are in contrast to the experimentally determined strain distribution presented in Figure 5.24. On the other hand, the strain distribution on the laser loaded surface obtained by the simulation of the User Programmable Feature is in good compliance with the experimental results on the relevant positions. Furthermore, the strain amplitude per cycle for SAM is larger then for the UPF but for the stress amplitude this relation is inverted. Comparing the stress-strain results for CuCrZr to the Cu-HCP CP test case,

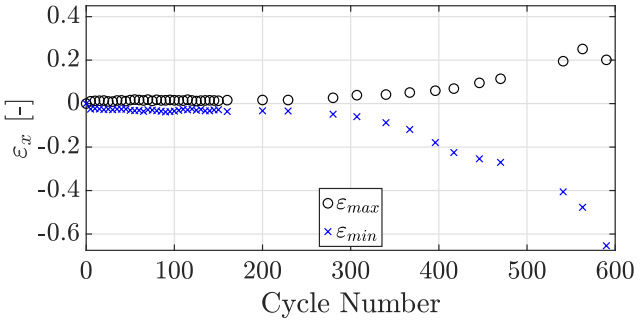

(a) Evolution of maximum and minimum residual strain over 590 cycles as determined with the Limess system by DIC.

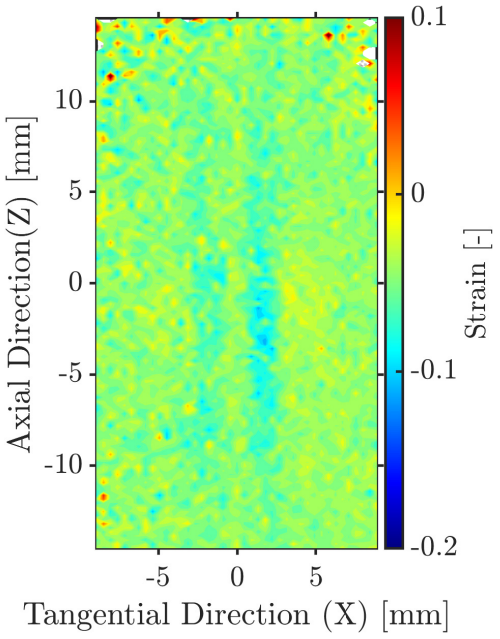

(b) Visible residual strain on the laser loaded surface after Cycle 279 around 40% of the overall number of cycles as determined with the Limess system by DIC.

Figure 5.24: Strain analysis of MV TMF panel

the strain levels are significantly lower for CuCrZr whereas the stress levels are significantly larger. Regarding the fatigue life estimation for the simulation using SAM in Figure 5.26e it is questionable if the results are of any meaning as the strain in Node 1 is not congruent with the experimental results. Additionally, the post-processing tool yields considerably large differences to the fatigue life estimation using the data obtained by the UPF. These results are presented in Figure 5.26f. As for previously described test cases the critical damage is reached first at the position of Node 3 after 486 cycles. This is in agreement with Figure 5.23a. Herein the exponential growth of the deformation starts around the same number of cycles. Hence, this event again can be interpreted as the beginning of macro-crack propagation in the experiment and subsequently rapid weakening of the wall structure. This point corresponds to 75% of the experimental fatigue life. This value is more than double the values obtained for the usable fatigue life of Cu-HCP and can be justified with the significantly more brittle behavior of the CuCrZr alloy. Node 2 hits the critical damage after 611 cycles and Node 1 fails after 665 cycles. The results, also comprising the fatigue life obtained by the post-processing tool for the simula-

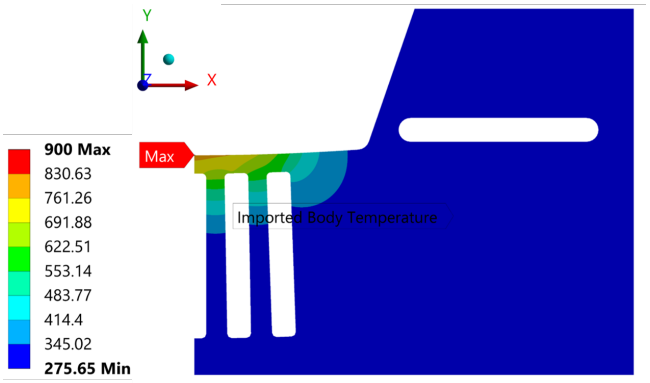

Figure 5.25: Temperature Distribution as obtained from coupled fluid-thermal analysis

tion with SAM, are summarized in Table 5.3. As for previously described test cases an evaluation of the stress-strain relation and damage was also performed for the in y-direction. As can be seen in Figures 5.27a to 5.27d the strain is almost exclusively positive (tensile). Additionally, also for the simulation of the CuCrZr TMF panel the stress levels in y-direction are very low but the strain amplitude per cycle is increased when compared to the previously described results for the x-direction. Following that, the fatigue life analysis with the post-processing tool yields unreasonably low results for each node. For the evaluation in Standard ANSYS Mechanical this ranges from 53 to 55 while the UPF yields 71 to 93 (see Table 5.3). The y-direction should therefore not be considered for the fatigue life estimation.

	SAM			**UPF**			**Exp**
Node	**1**	**2**	**3**	**1**	**2**	**3**	
x-direction	481	425	317	665	611	486	645
y-direction	54	55	53	71	89	93	

Table 5.3: Fatigue life results of the CuCrZr Material Variation analysis

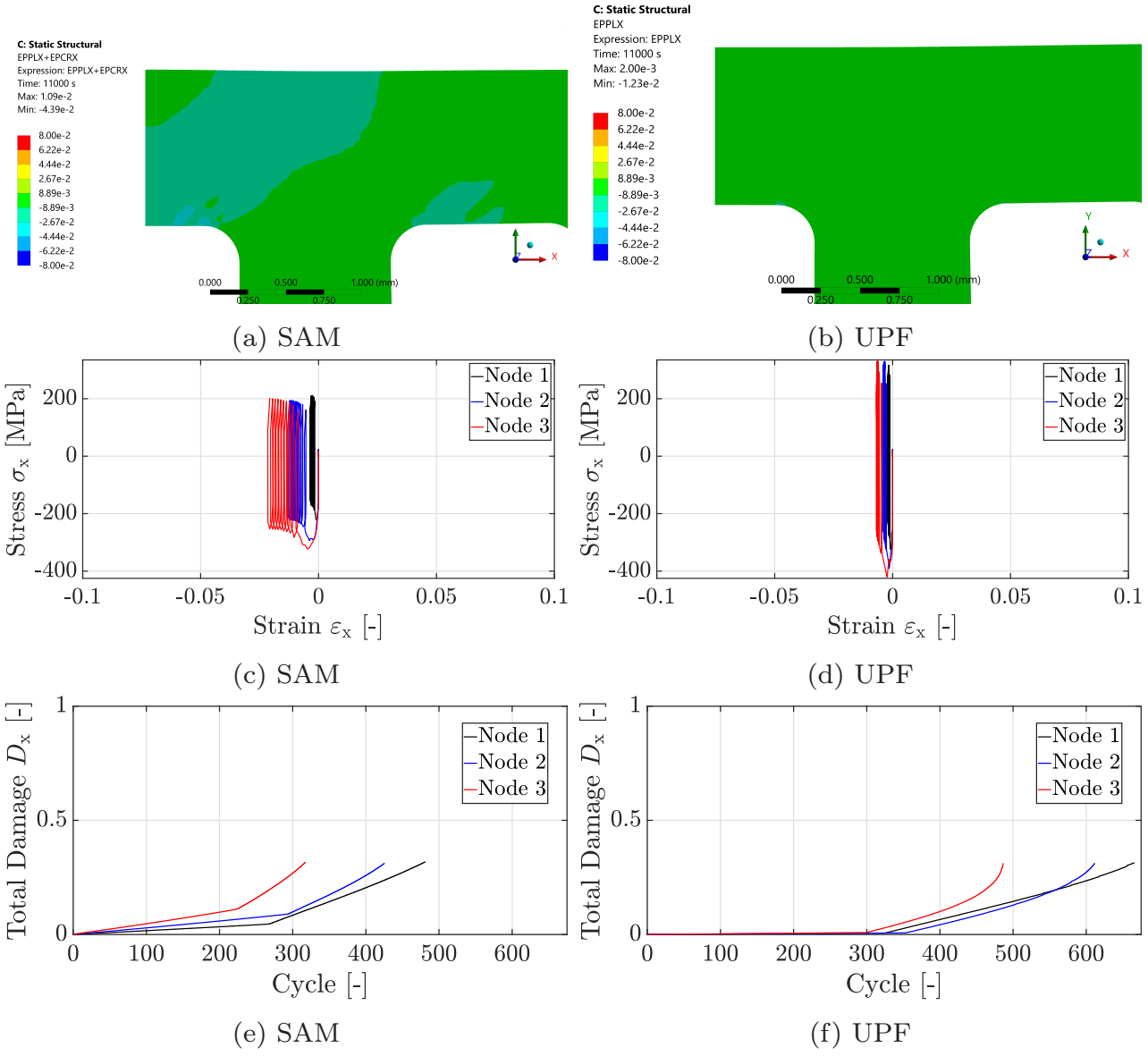

Figure 5.26: Fatigue life results of MV in x-direction

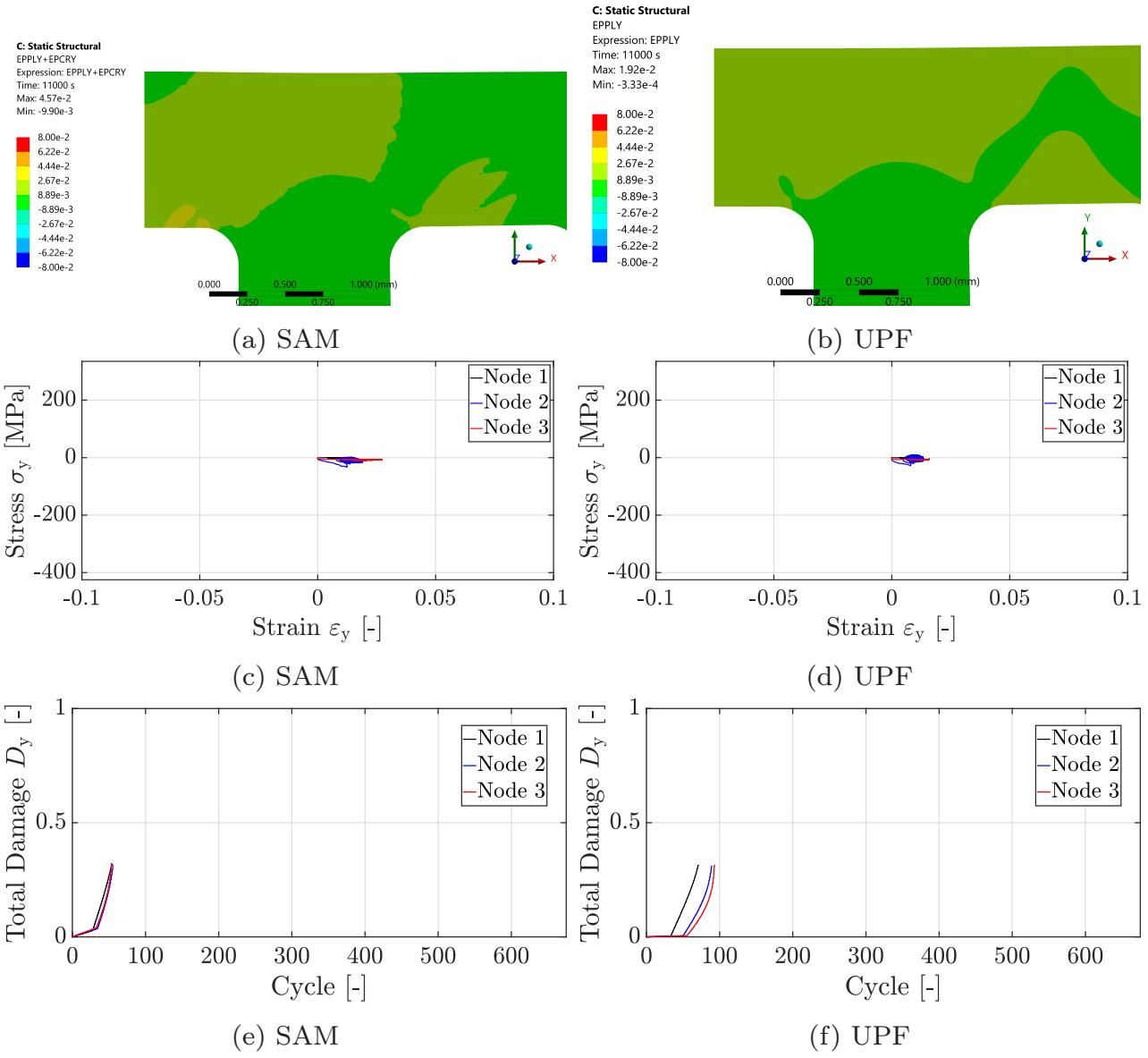

Figure 5.27: Fatigue life results of MV in y-direction

5.5 Mapping of Thermal Conductivity

As previously mentioned, a prominent result of the experimental work within this thesis is the influence of the progressing damage development on the degradation of thermal conductivity in the TMF panel. The local thermal conductivity on a sub-millimeter scale can be measured by the steady-state thermoreflectance method (SSTR) [160, 161]. This method has been used to uncover the thermal conductivity of a small area of $A_{\mathrm{SSTR}} = 1.2 \times 1.0\ \mathrm{mm}^2$ in a cross section of a tested CuCrZr TMF panel. The TMF panel test was executed at a maximum surface temperature of $T_{\mathrm{s}} = 1000$ K and a heat flux of $q_{\mathrm{w}} = 24.8\ \mathrm{MW/m^2}$ [10]. The SSTR analysis was performed at University of Virginia, Department of Mechanical and Aerospace Engineering [162, 163]. The results are displayed in Figure 5.28. The chosen cross section is located at

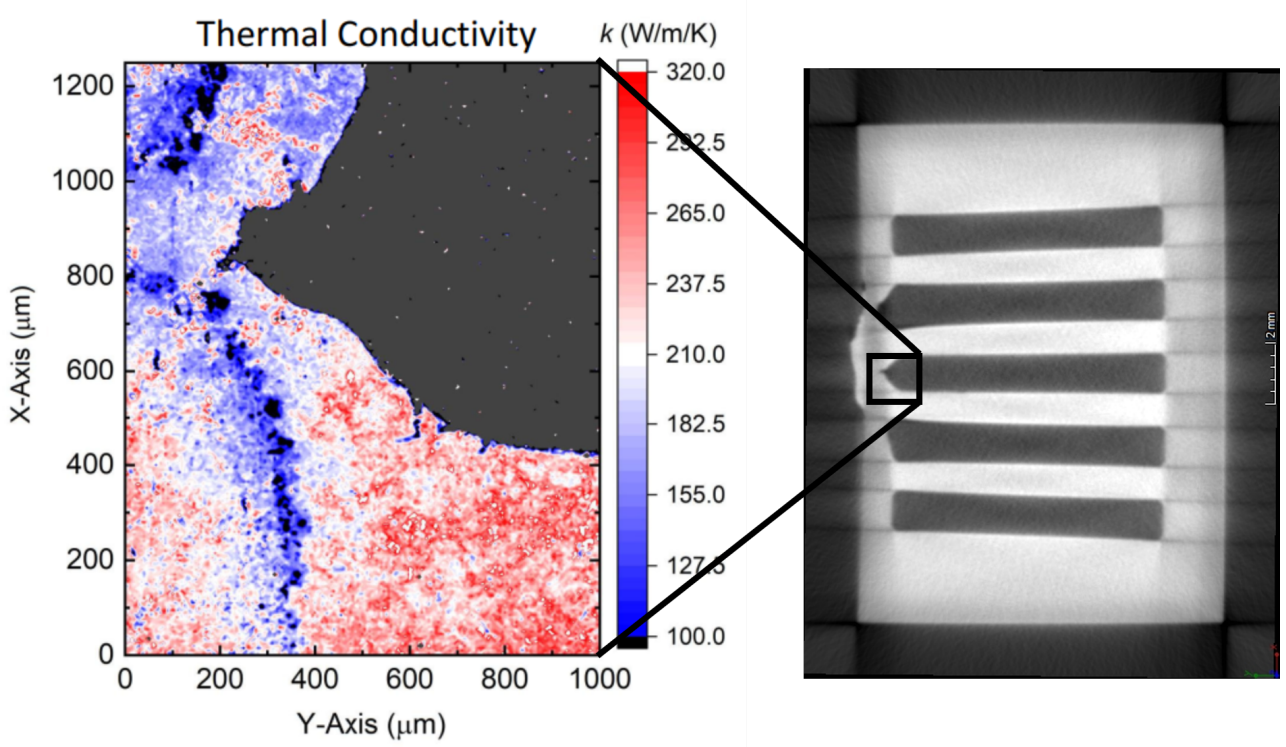

Figure 5.28: Results of thermal mapping via SSTR

$z = 2.5$ mm downstream of the final crack. The uppermost part of the central cooling channel was analyzed. The progressing tip of the crack can be seen around the coordinates $x = 800\ \mu$m, $y = 200\ \mu$m as its forefront propagates in the doghouse failure mode towards the laser loaded surface. From the leading edge of the crack two bands of very low thermal conductivity spread arching mainly in the x-direction. While the lower of the two can be clearly identified,

the upper one is mostly out of the measurement field. However, a symmetric picture is likely. It is assumed that these bands match with the predominant locations where plastic strain accumulates most and damage begins to form causing micro-cracks and voids. The position of these bands might have moved during the course of the test as the material moves. This can be seen from the accumulation of material on the laser loaded surface in Figure 5.28. The low-conductivity bands origin in the formation of micro cracks and voids which break the physical connection between atoms and prevent the transport of energy.

6 Application to LRE Segment

The previously described approach to estimate the fatigue life of a TMF panel is applied to a generic segment of a liquid rocket engine combustion chamber [9, 94]. The conditions of the TMF panel test cases have been applied to the LRE segment. Again, SAM and the UPF models are evaluated. The main geometry of the cooling channel and combustion chamber wall as well as the meshing is similar to the TMF panel. On the non-loaded side of the cooling channel a fragment of a generic Nickel jacket is added.

6.1 Numerical Setup

The geometry and mesh of the LRE segment are shown in Figure 6.1. The most significant features of geometry and mesh are similar to the simulations of the TMF panel test cases. Hence, the thickness of the quasi 2-dimensional model is $t_z = 0.02$ mm. The angular size of the model is $\gamma = 0.5°$, that covers half of a cooling channel and half of a fillet with angular symmetry conditions applied to both ends in x-direction. Three different temperature fields were obtained from three steady state thermal analyses. In particular, these refer to a maximum surface temperature of $T_{max} = 800$ K for Cu-HCP and CuCrZr and $T_{max} = 900$ K for Cu-HCP. A constant heat flux of $q_w = 50$ MW/m^2 has been applied to the hot gas wall to achieve heat fluxes closer to real LREs. On the cooling channel side, a constant convective boundary condition (film coefficient) was applied. Its magnitude was iteratively determined until the desired maximum temperature was reached. The resulting temperature distribution was subsequently applied to the static structural analysis. Note that due to the increased heat flux, the temperature level on the cooling channel side of the hot gas wall is increased.

The same meshing has been applied to both, the steady-state thermal anal-

Elements	6408
Nodes	47350

Table 6.1: Mesh properties of LRE Segment

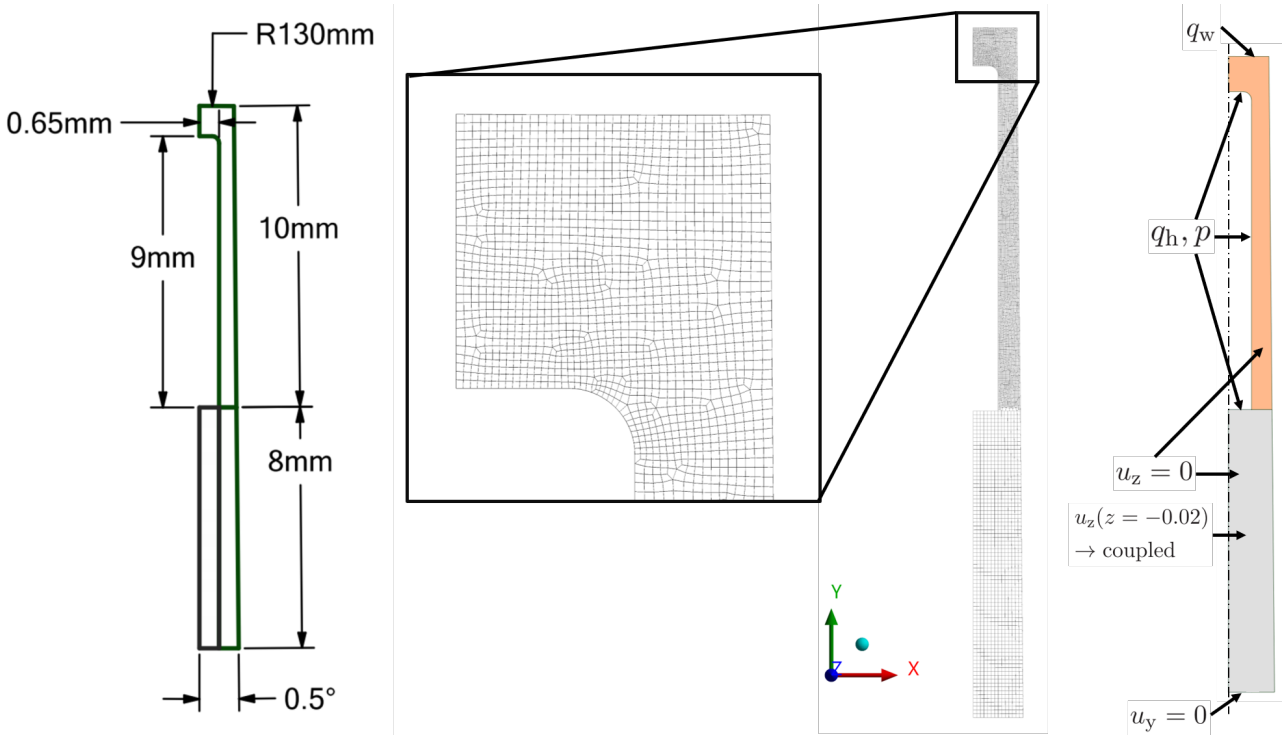

Figure 6.1: Geometry and mesh of the generic LRE combustion chamber segment

ysis and the mechanical analysis. The hot gas wall features 32 elements in y-direction. Over the complete model one element is applied in the z-direction. All elements are 3D hexahedral elements of type SOLID186. For all six mechanical analyses the same uniform pressure was applied to the cooling channel walls. It is similar to the pressure distribution of the Cu-HCP central point.

6.2 Results

The temperature distribution applied to the mechanical model as imported load for the individual simulations is shown in Figure 6.2. The individual fatigue life results of the three different sets of boundary conditions are presented in Figures 6.3 (Cu-HCP, $T_s = 800$ K), 6.4 (Cu-HCP, $T_s = 900$ K) and 6.5 (CuCrZr, $T_s = 800$ K). The layout is similar to the results presented in Chapter 5 for the simulation of the TMF panel tests. Additionally, the calculated number of cycles obtained by the post-processing tool are summarized in Table 6.2.

Generally, for Cu-HCP the stress levels of the LRE segment and TMF panel simulations are comparable for both test cases as well as for the Standard ANSYS Mechanical and the usage of the UPF. The strain amplitude is slightly increased for the LRE segment when comparing to its counterpart of the TMF

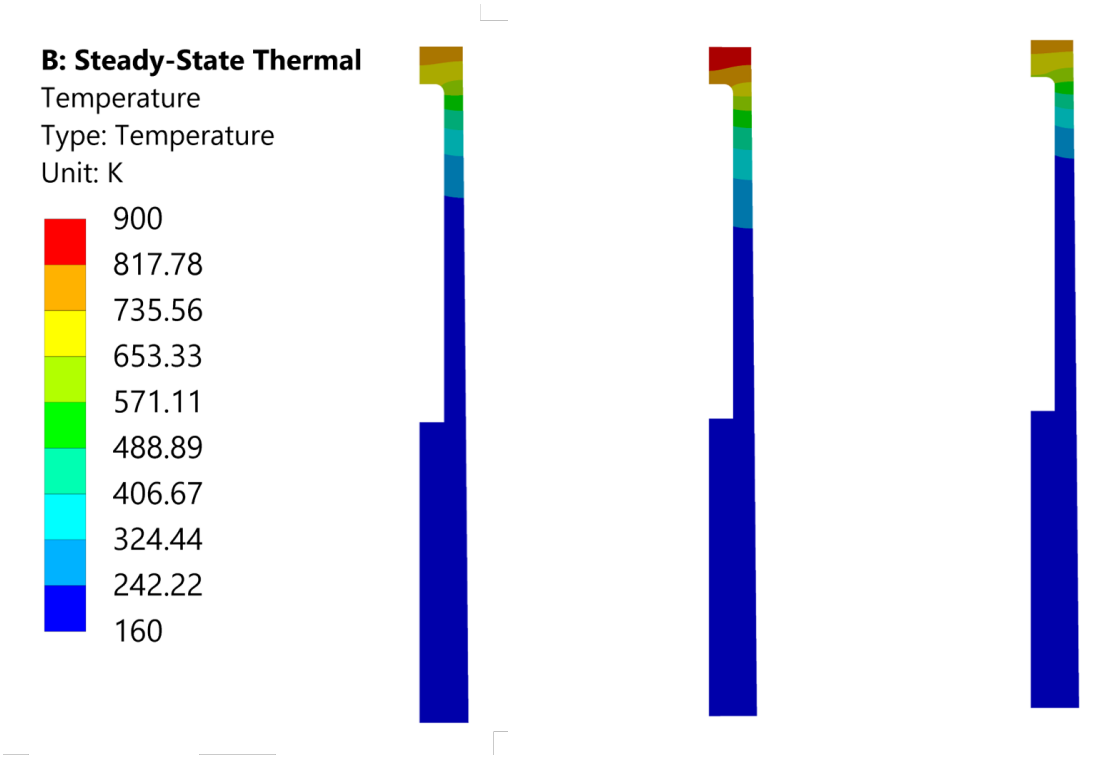

(a) Cu-HCP, $T_s = 800$ K

(b) Cu-HCP, $T_s = 900$ K

(c) CuCrZr, $T_s = 800$ K

Figure 6.2: Temperature distribution of the different LRE segment simulations

panel simulations. The major difference between the LRE segment simulation and the TMF panel test simulation is observed in ratcheting. In particular Node 3 shows very small amounts of ratcheting in the LRE segment. In contrast to that, Node 1 and 2 show an increased amount of ratcheting. However, for SAM Node 3 has the highest amount of ratcheting, for the UPF this changes to Node 1. The number of cycles until the critical damage is reached in Node 3 is 59. That number of cycles is similar for the post-processing with SAM and the UPF model but higher than calculated for the respective TMF panels. This is defined as the useful fatigue life. The fatigue life results for Nodes 1 and 2 are lower for the LRE segment analysis. This is mainly due to the increased ratcheting.

For the CuCrZr test case the simulation and fatigue life results greatly differ between LRE segment and TMF panel. This is caused by highly increased stress and strain levels for the LRE segment simulation. Interestingly, the fatigue life of Node 3 for the CuCrZr and Cu-HCP LRE segment are very close, but slightly higher for Cu-HCP. In the analyses performed by Thiede [9] a similar deviation between the simulation of the fatigue life of the TMF

panel (356 cycles) and the LRE Segment was observed (37 cycles). Since the simulation for the CuCrZr TMF panel test delivered accurate and reasonable results for the present work and the work of Thiede, the root cause of the significantly higher stress and strain levels leading to a lower fatigue life in the LRE segment simulation needs further in-depth investigation which is beyond the scope of this work.

	SAM			**UPF**		
Node	**1**	**2**	**3**	**1**	**2**	**3**
Cu-HCP 800 K	107	64	59	89	79	59
Cu-HCP 900 K	94	38	28	75	43	33
CuCrZr 800 K	84	59	57	69	51	50

Table 6.2: Fatigue life results of a generic LRE segment

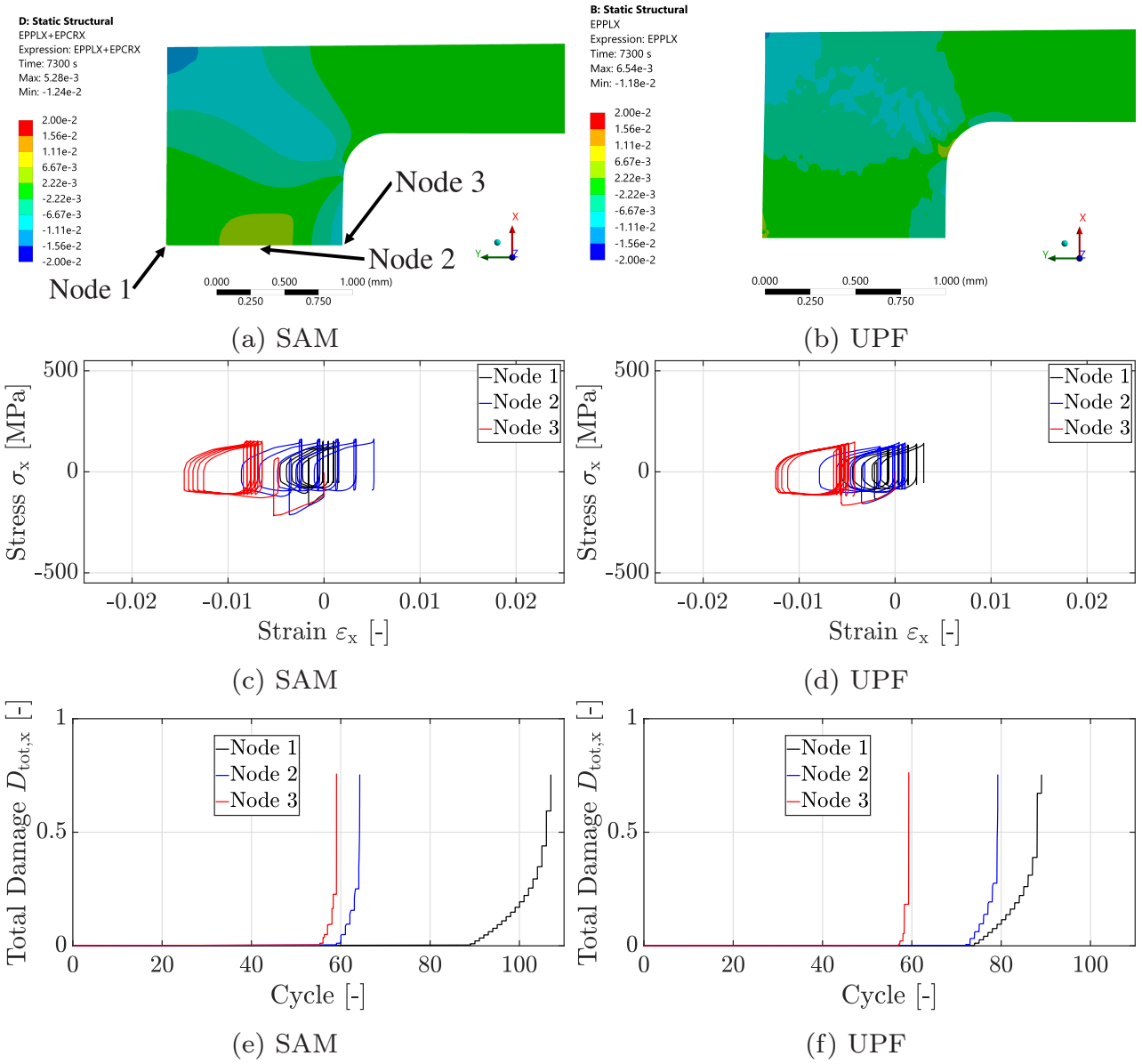

(a) SAM (b) UPF

(c) SAM (d) UPF

(e) SAM (f) UPF

Figure 6.3: Fatigue life results of a Cu-HCP LRE Segment $T_s = 800$ K in x-direction

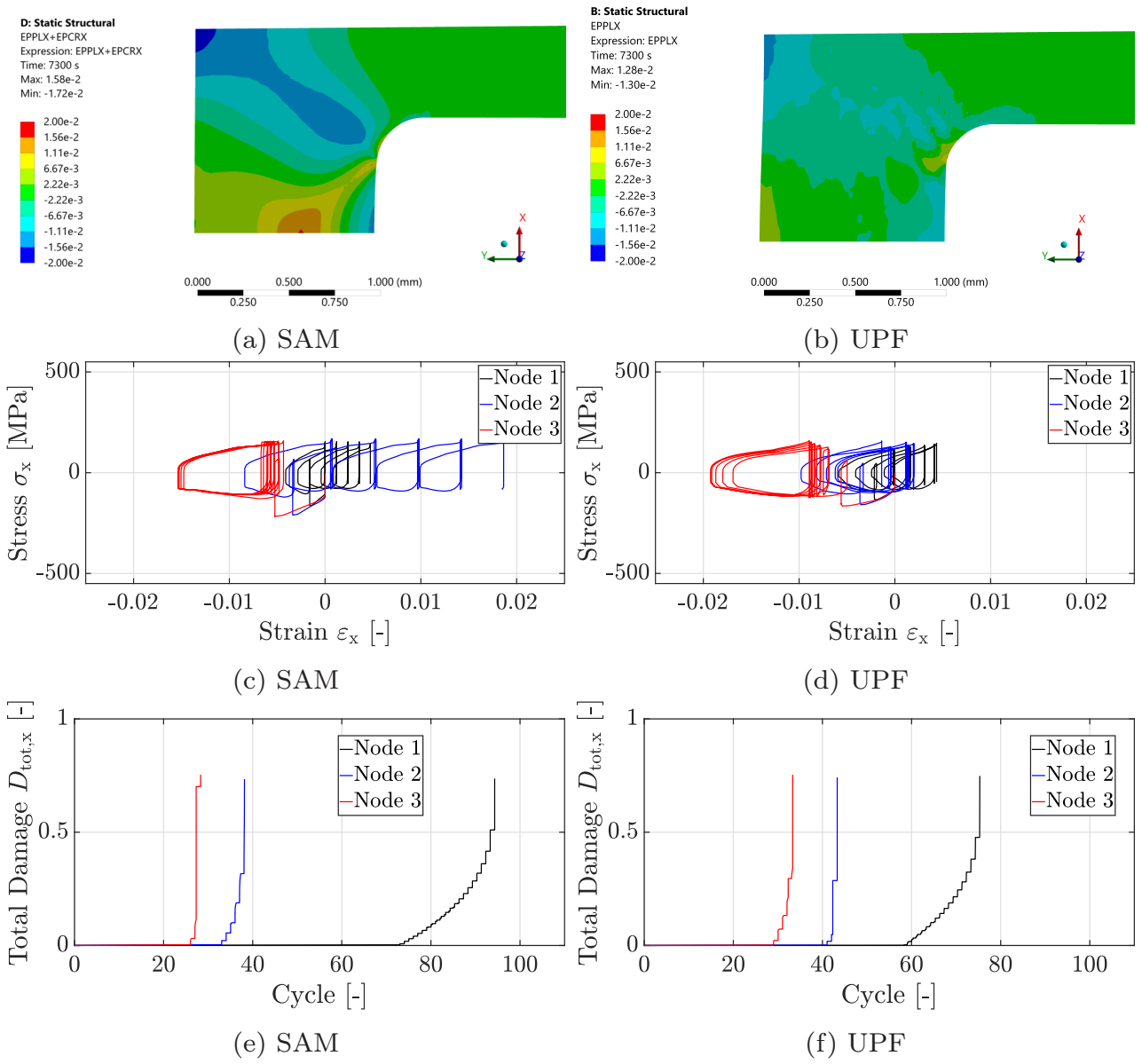

(a) SAM (b) UPF

(c) SAM (d) UPF

(e) SAM (f) UPF

Figure 6.4: Fatigue life results of a Cu-HCP LRE Segment with $T_s = 900$ K in x-direction

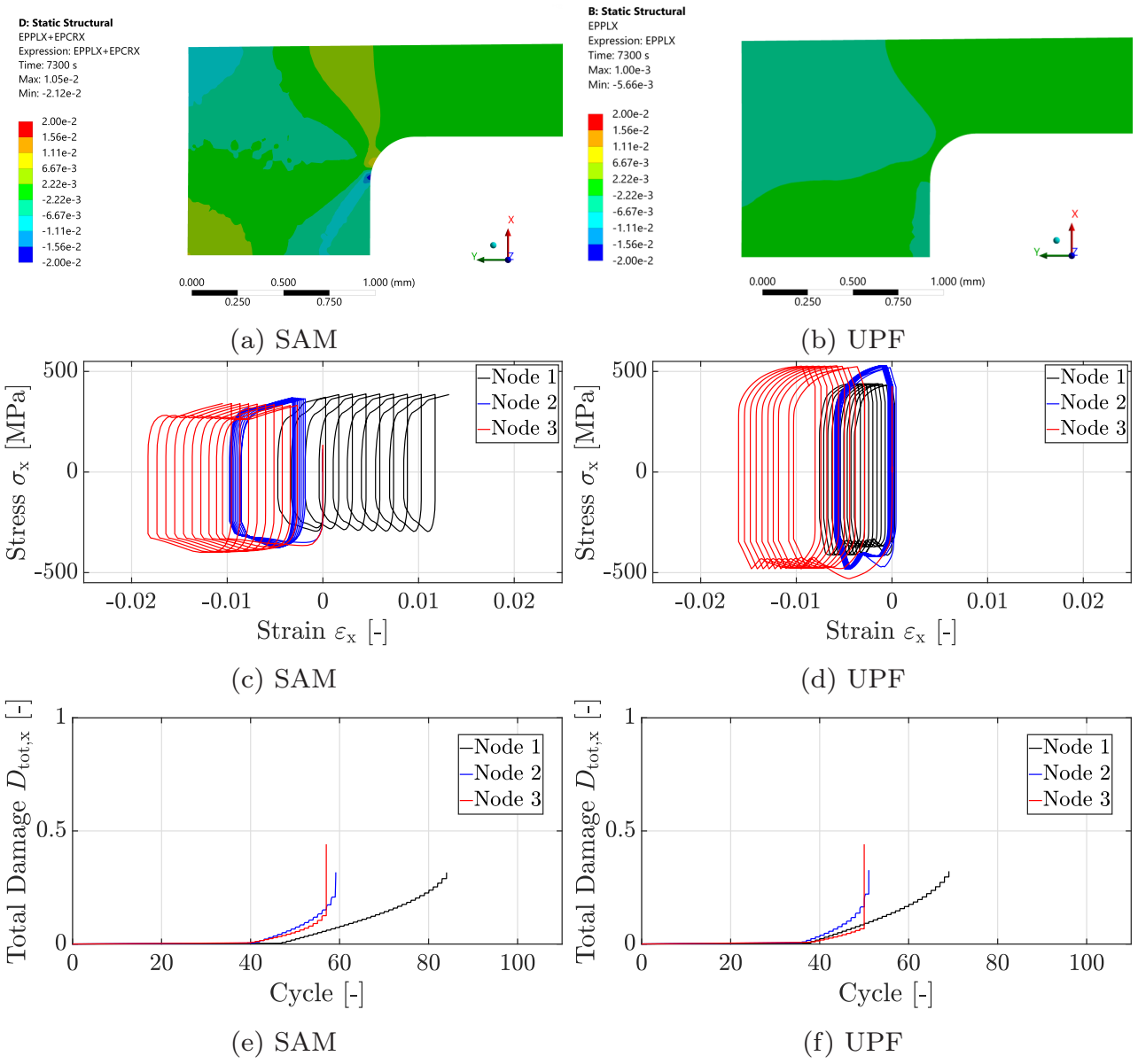

(a) SAM (b) UPF

(c) SAM (d) UPF

(e) SAM (f) UPF

Figure 6.5: Fatigue life results of a CuCrZr LRE Segment with $T_s = 800$ K in x-direction

7 Conclusions and Outlook

In the present thesis the thermomechanical fatigue of TMF panels representing the inner liner of liquid rocket engine combustion chamber geometries has been examined experimentally and numerically. A TMF panel represents a small portion of a regeneratively cooled rocket combustion chamber, typically seven cooling channels. Four experimental panel test campaigns were conducted using three TMF panels made from Cu-HCP and one made from CuCrZr. The panels undergo cyclic thermal loading until failure. The TMF panel test campaigns are executed at the TMF test bench at DLR Institute of Space Propulsion. The test bench uses supercritical nitrogen as a coolant, replacing hydrogen or methane that is commonly used in LREs. The heat load is applied by a high power diode laser that is cyclically turned on demonstrating multiple load cycles as required for a reusable rocket engine. With the present setup the pure mechanical performance of the material can be analyzed excluding any influences that arise from combustion processes like temperature and pressure fluctuations or chemical reactions. Furthermore, the setup allows for the precise measurement of heat flux, surface temperature, mass flow rate as well as temperature and pressure of the fluid. This serves as the accurate basis for the following numerical simulation and its validation.
For all test campaigns the conditions of the supercritical nitrogen were fixed to an inlet temperature of $T_{\mathrm{in}} = 160$ K and an outlet pressure of $p_{\mathrm{out}} = 55$ bar when the laser is powered on. The laser has a top-hat shaped profile in the focal plane spanning an area of $A_{\mathrm{focal}} = 11.2$ mm $\times$ 32.2 mm. The laser sequence included a linear ramp-up of 30 s to a heat flux of $q_{\mathrm{w}} = 24.25$ MW/m^2 followed by a constant loading duration of 200 s and a ramp-down of 30 s.
At first, a heat transfer test (HTT) panel investigated the relation of surface temperature, mass flow rate and heat flux for Cu-HCP. The surface temperature was varied between $T_{\mathrm{s}} = 648$ K to $T_{\mathrm{s}} = 1000$ K while the heat flux was varied between $q_{\mathrm{w}} = 12.0$ MW/m^2 and $q_{\mathrm{w}} = 24.6$ MW/m^2. This results in Reynolds numbers between $Re = 0.93 \times 10^5$ to $Re = 4.89 \times 10^5$ for the supercritical nitrogen coolant. With the help of the experimental results it is possible to determine the mass flow rate for the following Cu-HCP TMF panel test campaigns by interpolation, eliminating the need of an iterative approach as done before. More importantlz a coupled simulation in ANSYS consisting

of a CFX fluid simulation and a steady state thermal analysis for the structure could be validated. This yields the temperature field inside the TMF panel which is a key input for the following structural analyses in ANSYS Mechanical.
Subsequently, three TMF panel test campaigns were conducted. Two test campaigns with panels made from Cu-HCP studied the influence of the surface temperature at $T_s = 800$ K (central point, CP) and $T_s = 900$ K (temperature variation, TV). The higher temperature causes a decrease of the fatigue life of 12 %, i.e. the panels ruptured in the 151^{st} and 133^{rd} cycle. Generally, Cu-HCP becomes very ductile at high temperatures, eventually leading to a significant bubble shaped deformation on the TMF panel surface that bursts at the point of failure. The bubble starts to develop after 60 cycles for the central point test campaign and after 42 for the TMF panel at higher temperature. It is characterized by a nonlinear increase of the rate of deformation. This point is described as the "useful fatigue life" of the TMF panel as in a real liquid rocket engine the high deformation would likely cause a rapid failure of the inner liner because it would affect the flow condition, increase the heat flux and be subjected to abrasion. The useful fatigue life is associated with the number of cycles after which the innermost point of the heat loaded wall reaches critical damage, hence a macro-crack is formed. In addition to the fatigue life results the mass flow rate over the course of the test campaigns caught attention. It had to be increased until circa half of the cycles to failure. From here on it had to be decreased again. It is assumed that the mechanical damage in the TMF panel wall significantly affects the thermal conduction as micro cracks and voids locally prohibit heat transfer. This theory is strongly supported by a steady state thermoreflectance analysis conducted with a section of a used TMF panel segment. In this analysis very low thermal conductivity could be observed in small bands that coincide with the locations of high accumulation of plastic strain.
The third TMF panel test campaign utilized a TMF panel made from CuCrZr and was also tested at $T_s = 800$ K to investigate the influence of a different material on the fatigue life. The panel ruptured after 645 cycles increasing the fatigue life when compared to Cu-HCP at the same boundary conditions to 427.1 %. The useful fatigue life in the experiment was determined to around 360 cycles.
The numerical analyses of the TMF panel tests uses three different mechanical models in ANSYS Mechanical to determine the stress and strain field in a quasi 2-dimensional cross section of the TMF panel at the point of maximum surface temperature. Subsequently, the fatigue life and particularly the useful fatigue

life is estimated by a post processing tool in MATLAB. Due to symmetry, the numerical model could be reduced to half a TMF panel cross section. Two of the material models were implemented in ANSYS by a user programmable feature, one for each material. The third model is a custom material model comprised of the available models in ANSYS Mechanical. In particular these models are the kinematic hardening model according to Chaboche, the isotropic hardening developed by Voce, a strain-rate dependent model based on the work of Peirce, and Norton's creep law. The parameters for the user programmable features were taken from literature and externally determined in the framework of an ongoing project, respectively. The parameters for the individual parts of the custom material model have been determined from an extensive set of complex low cycle fatigue tests. The temperature field as determined by the previously mentioned coupled analysis is taken from the cross section of maximum surface temperature and applied as imported load on a the quasi 2-dimensional model. As the structural analysis and damage evolution are decoupled it is sufficient to simulate only 5 cycles for Cu-HCP and 10 cycles for CuCrZr. After this number of cycles a constant accumulation of plastic strains is achieved. The subsequent analysis of damage evolution in MATLAB used a combination of the damage evolution law for the ductile damage model developed by Bonora and the fatigue damage model according to Lemaitre. The respective parameters were determined from interrupted tensile tests for the Bonora model and in case of the model by Lemaitre from the previously mentioned complex low cycle fatigue tests. The damage evaluation was conducted using the stress and strain relations for three representative nodes on the symmetry axis of the TMF panel. The nodes are located on the TMF panel surface, at the top of the cooling channel and right in the middle between the two previously mentioned nodes. Generally, the node located at the cooling channel surface experiences the highest strain amplitude per cycle but also the highest amount of ratcheting. Hence, according to the post-processing damage analysis the critical damage is reached first at this point, implying the initiation of a macro-crack. Secondly, the node in the middle of the heat loaded wall reaches critical damage, followed by the node on the TMF panel surface. The number of cycles until critical damage is reached at the node on the cooling channel side of the loaded wall is congruent with the experimentally determined useful fatigue life. The difference in the number of cycles between the user programmable feature and the model available in ANSYS is very low for both test cases of Cu-HCP. However, it becomes significant for CuCrZr. Here the user programmable feature shows a higher number of cycles until the critical damage is reached for all three nodes considered.

In summary, the experimental results show that the approach developed to predict the useful fatigue life by three steps including the determination of the temperature field that is applied to a 2-dimensional structural analysis yielding stress and strain values which are fed into a post-processing tool evaluating the damage evolution is robust. The described approach yields a computationally efficient and fast estimation of the useful fatigue life for a regeneratively cooled liquid rocket engine combustion chamber.
The described approach was subsequently applied to a segment of a liquid rocket engine consisting of half a cooling channel and half the fillet between cooling channels. The same boundary conditions were utilized as for the simulations of the TMF panels, except the heat flux into the combustion chamber wall was increased to $q_{\mathrm{w}} = 50\ \mathrm{MW/m^2}$ as this value is closer to real liquid rocket engines. The resulting useful fatigue life for the LRE segment yields good congruence with the TMF panel results for Cu-HCP. For the CuCrZr case, a great difference could be observed which has to be investigated further. From an experimental point of view each of the test campaigns was only conducted once. Hence, the number of cycles achieved for the experimental fatigue life is statistically not reliable. Future work should therefore involve the repetition of the TMF panel test campaigns. This would increase the reliability of the developed approach and lead to a statistically more sophisticated evidence of the fatigue life. Furthermore, the degradation of the thermal conduction due to damage should be investigated further. This can be done by including a damage parameter into the thermal analysis but would involve several coupled simulations. For this proposal the structural analysis has to incorporate a damage variable that is transferred to the thermal analysis. Again, the thermal analysis has to be coupled with the CFX simulation to update the temperature fields in the fluid and the structure. Afterwards, the new temperature field has to be considered by the structural analysis again. Unfortunately, this would be a computationally intense setup of the simulation. The analysis can be validated by further measurements of the thermal conductivity with the steady state thermoreflectance method. Also in the software package ANSYS several methods for crack initiation and development are already implemented. Since the models available in ANSYS generally showed faster computation times than the user programmable features they should be considered in the first place.

A Material

ZOLLERN
ZOLLERN GmbH & Co. KG
Zentrallabor
Central laboratory

Laborbericht
Test report
Nr. / no.: 46561

Kunde: Customer	DLR		
Auftrags-Nr. Zollern Internal production order	7976601	**Proben Anlieferung:** Specimen handed over by	ZGT-QS-Streich
Charge: Batch	3648 / 4 / 1	**Anlieferdatum:** Specimen handed over at	27.06.2017
Legierung: Alloy	OF-CU	**Lieferzustand:** Delivery condition	geschmiedet
Materialnummer: Internal designation	1518095	**Schliffanzahl:** Microsections:	1
Spezifikation: Specification	entsprechend Prüfplan	**Verwendete Prüfmittel Nr.:**	30

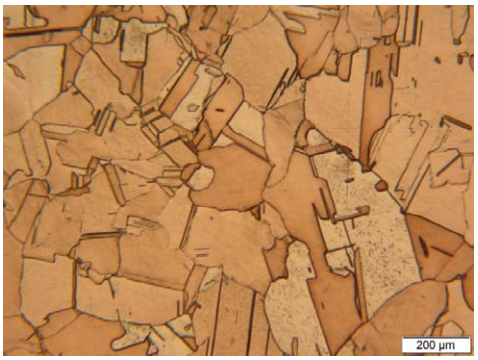

Schliff-Nr: 46561

Durchgeführte Prüfungen entsprechend Prüfplan:
Korngröße / Grain size
Mittlere Korngröße / median grain size
Soll: < 0,30 mm Ist: 0,19 mm

Datum: Date 30.06.2017
Bearbeiter: Tested by Zimmerer

914 Rev. 03 vom 28.11.2013
Seite / page 1 von / of 1
In Zweifelsfällen ist die deutsche Version maßgeblich. In case of doubt, the German version shall apply.

Abnahmeprüfzeugnis 3.1 / Inspection certificate 3.1

DIN EN 10 204

ZOLLERN GmbH & Co. KG, Hitzkofer Str. 1, D-72517 Sigmaringendorf-Laucherthal

ZOLLERN

Seite/Page: 1 von/of 1

Kunde/Customer	**Deutsches Zentrum Für Luft-**	Kunden-Nr./Customer No.	**153411**
Material-Nr./Mat.No.	**1518095**	Kunden-Mat-Nr./Customer Mat.No.	
Bezeichnung/Description	**Vierkant**	Kundenprojekt/Client project	
Probe-Nr./Sample No.		Charge-Nr./Heat No.	**3648/4/1**
Bestell-Nr./Purchase Order No.	**X/647/67244740/29.05.2017**	Kundenauftrag/Customer Order	**1113023912 / 000010**
Lieferung/Delivery	**1114057625 / 000010**	Liefermenge/Delivery Quantity	**1 ST**

Kundenzeichnung/Client drawing:	**Index**	Erschmelzungsart/melting type	**Induktiv / inductive**
Fertigungsverfahren/prod. proc.	**Freiformgeschmiedet / hot forged**	Oberflächenzust./surface condition	**mechanisch bearbeitet / mech. machined**
Werkstoffspez./material spec.	**EN 13601**	Werkstoff/material	**Cu-ETP/CW004A**

Kennzeichnung: **Charge Nr.; Zollern Logo**

Marking: **heat-no.; zollern logo**

Prüfergebnisse/Test results

Chemische Analyse in % /chemical analysis in %

	Cu	Bi	Pb	O												
Soll/ ref.	99,90	0,0005	0,005	0,040												
Ist/act.	**99,98**	**0,0001**	**0,001**	**0,040**												

Mechanische Eigenschaften/mechanical properties

	Rm N/mm²	A5 %					HB HB		
Prüftemp./Test temp.	RT	RT							
Soll/ reference									
Ist/actl.	**208**	**55,8**					**63**		

Es wird bestätigt, dass die Erzeugnisse den Anforderungen der Bestellung und der aktuell gültigen Spezifikationen entsprechen.
We hereby confirm that the products comply with the order requirements and the currently valid specifications.

Datum/date:	**17.07.2017**	Abnahmebeauftragter/inspection representative:	**Paul Schuler**

Das Prüfzeugnis wurde maschinell erstellt und ist ohne Unterschrift gültig.
This is a computer generated inspection document and it is valid without signature.

Note that the material is wrongly designated as "Cu-ETP" due to a mistake by the supplier, though it still is Cu-HCP.

Charge-Nr. 3648/4

ppm_Ni	ppm_Sn	ppm_Fe	ppm_Zn	ppm_Ag	ppm_S	ppm_As	ppm_Sb	ppm_Cd	ppm_Mn
5.7	0.9	4.1	1.2	13.9	13.8	0.3	0.5	0.2	1.0

ppm_Se	ppm_Te
0.4	0.5

Charge Nr.	Leitf. Sm/mm²	O2 (ppm)	Pb (ppm)	P (ppm)	Bi (ppm)	Cu (%)
1381/3	58,00	5	1,0	29,9	0,5	99,98
2640/1	58,00	4	1,0	22,5	0,5	99,98
3648/4	58,00	5	1,0	25,6	0,5	99,98

B Uniaxial Material Tests

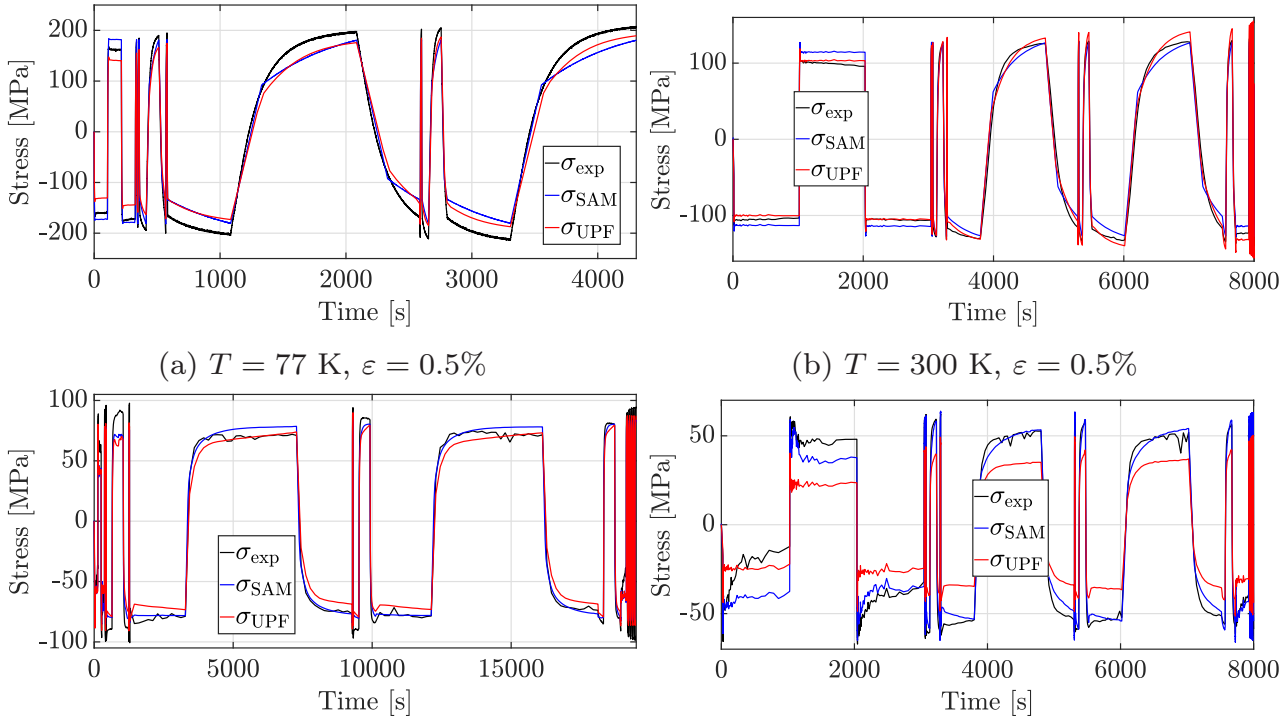

(a) $T = 77$ K, $\varepsilon = 0.5\%$

(b) $T = 300$ K, $\varepsilon = 0.5\%$

(c) $T = 427$ K, $\varepsilon = 2.0\%$

(d) $T = 527$ K, $\varepsilon = 0.5\%$

Figure B.1: Exemplary CLCF test pre-program data and comparison with numerical models

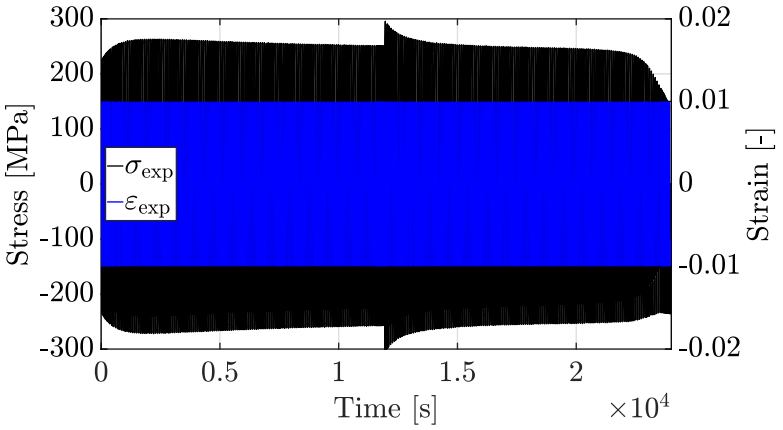

(a) $T = 77$ K, $\varepsilon = 1.0\%$

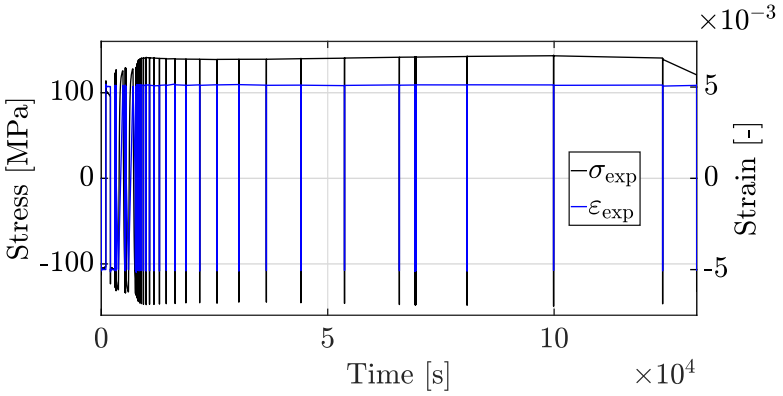

(b) $T = 300$ K, $\varepsilon = 0.5\%$

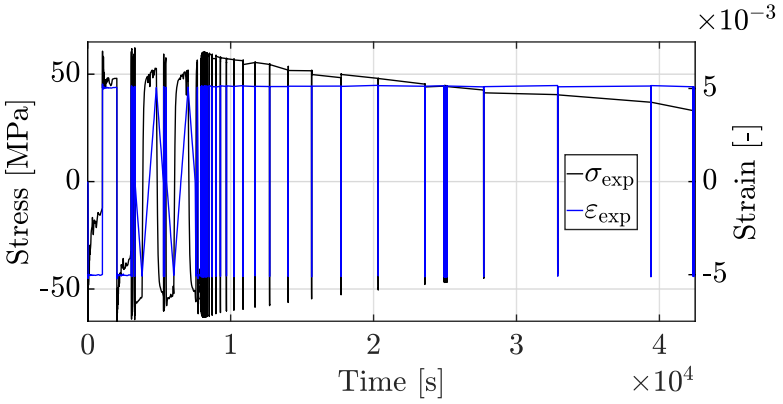

(c) $T = 527$ K, $\varepsilon = 0.5\%$

Figure B.2: Complete exemplary CLCF test data with gaps due logarithmic data reduction

C Roughness Cu-HCP

Bestimmung der Rauhigkeit der Kanaloberflächen des TMF-Panels

Horizontale Linie 1 - Fläche 1

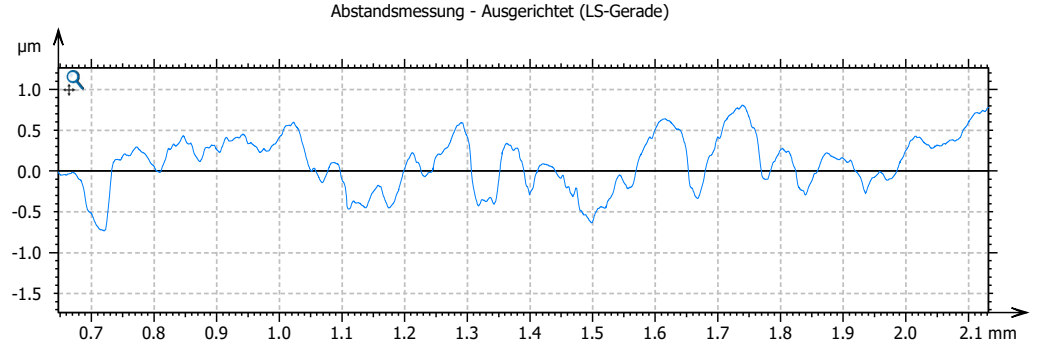

Parameter	0-1	Einheit
Höhenunterschied der Punkte	2.204	µm
Winkel	2.379	°

ISO 4287 - Rauheit (S-L)			
F: [Analyseablauf] Ausgerichtet (LS-Gerade)			
S-Filter (λs): Doppelter Gauß, 2.500 µm			
L-Filter (λc): Doppelter Gauß, 0.8000 mm			
Messstrecke: Alle λc (3)			
Amplituden-Parameter			
Rz	1.754	µm	*Maximale Höhe des Rauheitsprofiles*
Ra	0.3030	µm	*Arithmetische Durchschnittsabweichung des Rauheitsprofiles*
Rq	0.3799	µm	*Durschschnittliche quadratische Abweichung (RMS) vom Rauhei...*

Achse:	X	
Länge:	2.546	mm
Größe:	6609	Punkte
Schrittabstand:	0.3853	µm
Achse:	**Z**	
Länge:	4.830	µm
Min.:	5.980	µm
Max:	10.81	µm
Größe:	48300000	Ziffern

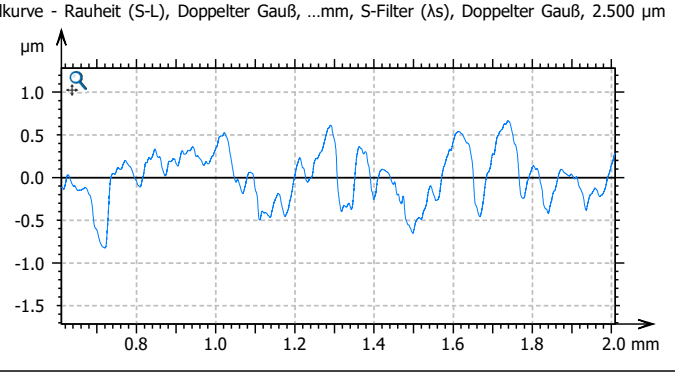

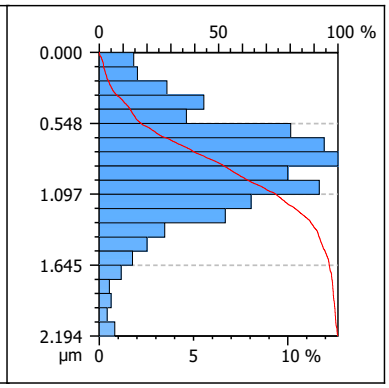

MountainsMap® Imaging Topography 8.1.9413

Bibliography

[1] D. Preclik et al. “Reusability aspects for space transportation rocket engines: programmatic status and outlook”. In: *CEAS Space Journal* 1.1-4 (June 2011), pp. 71–82. DOI: 10.1007/s12567-011-0006-x.

[2] S. Harris. “Block II - The new Space Shuttle Main Engine”. In: *32nd Joint Propulsion Conference and Exhibit*. American Institute of Aeronautics and Astronautics, July 1996. DOI: 10.2514/6.1996-2853.

[3] R. J. Quentmeyer. “Experimental fatigue life investigation of cylindrical thrust chambers”. In: *13th Propulsion Conference*. American Institute of Aeronautics and Astronautics, July 1977. DOI: 10.2514/6.1977-893.

[4] Astra. Mar. 2023. URL: https://astra.com/news/conclusion-tropics-1-mishap-investigation/.

[5] George Paul Sutton and Oscar Biblarz. *Rocket propulsion elements*. 7. ed. A Wiley-Interscience publication. Includes bibliographical references and index. New York: Wiley, 2001. 751 pp.

[6] Carmen Ramirez and Shamim Rahman. “An Analysis of Rocket Propulsion Testing Costs”. In: *46th AIAA/ASME/SAE/ASEE Joint Propulsion Conference & Exhibit*. American Institute of Aeronautics and Astronautics, July 2010. DOI: 10.2514/6.2010-6797.

[7] Jörg R. Riccius et al. “TMF: Laser Application for a Close-to-Reality Simulation of Thermo-Mechanical Fatigue Processes in Rocket Engines”. In: *EUCASS 2007*. Ed. by von Karman Institute and ULB. July 2007. URL: https://elib.dlr.de/53140/.

[8] Andreas Gernoth. “Untersuchung der Turbulenzmodellierung von rauen Rechteckkanalströmungen mit Berücksichtigung der Oberflächenverformung im Hinblick auf die Anwendung in Raketenmotoren”. PhD thesis. Universität Stuttgart, 2013. URL: https://elib.dlr.de/86243/.

[9] Gordan Thiede. “Validation of Damage Parameter Based Finite Element Fatigue Life Analysis Results to Combustion Chamber Type Thermomechanical Fatigue Panel Tests”. PhD thesis. Rheinisch-Westfälische Technische Hochschule Aachen, 2019. URL: https://elib.dlr.de/131273/.

[10] Pascal H. Kringe, Jörg R. Riccius, and Michael Oschwald. "Low-cost life assessment of liquid rocket engines by replacing full-scale engine tests with TMF panel tests". In: *Journal of the British Interplanetary Society* 73.5 (May 2020), pp. 152–162.

[11] Jörg R. Riccius, Micha W. Böttcher, and Hugo Duval. "A first step into the blanching modelling of Liquid Rocket Engines: taking into account the roughness increase of the chamber wall". In: 2019.

[12] A. Carden, D. Harman, and E. Franco-Ferreira. *Thermal fatigue analysis of a cryogenically cooled rocket nozzle*. Tech. rep. Oak Ridge, Tennessee: Oak Ridge National Labaratory, 1966.

[13] NASA. "NTRS - NASA Technical Reports Server". In: (). URL: https://ntrs.nasa.gov/.

[14] R W Miller. *Cyclic fatigue analysis of rocket thrust chambers: Volume 1: OFHC copper chamber low cycle fatigue,* Tech. Report NASA-CR-134641-VOL-1. NASA LewisResearch Center, 1974.

[15] Harold J Kasper. *Graphical method for predicting life of a rocket thrust chamber with half-hard zirconium-copper liner and electroformed nickel closeout*. Tech. rep. 1977.

[16] Ned P Hannum and RG Price Jr. *Some effects of thermal-cycle-induced deformation in rocket thrust chambers*. Tech. rep. 1981.

[17] M. L. Badlani et al. "Development of a simplified procedure for rocket engine thrust chamber life prediction with creep". In: 1983. URL: https://ntrs.nasa.gov/api/citations/19840011404/downloads/19840011404.pdf.

[18] Albert J. Pavli, John M. Kazaroff, and Robert S. Jankovsky. "Hot fire fatigue testing results for the compliant combustion chamber". In: 1992. URL: https://ntrs.nasa.gov/citations/19930001555.

[19] Robert S. Janovsky et al. "Structurally compliant rocket engine combustion chamber - Experimental and analytical validation". In: *Journal of Spacecraft and Rockets* 32.4 (July 1995), pp. 645–652. DOI: 10.2514/3.26665.

[20] RT Cook, EE Fryk, and JF Newell. *SSME main combustion chamber life prediction*. Tech. rep. NASA-CR-168215. NASA-Lewis Research Center, 1983.

[21] Vinod K. Arya. "Nonlinear structural analysis of cylindrical thrust chambers using viscoplastic models". In: *Journal of Propulsion and Power* 8.3 (May 1992), pp. 598–604. DOI: 10.2514/3.23520.

[22] Vinod K. Arya and Steven M. Arnold. “Viscoplastic analysis of an experimental cylindrical thrust chamber liner”. In: *AIAA Journal* 30.3 (Mar. 1992), pp. 781–789. DOI: 10.2514/3.10985.

[23] Olivier Ferrandon et al. “Vulcain 2 Nozzle Extension: Integrated European Team and Advanced Computational Model to the Service of Nozzle Design”. In: *41st AIAA/ASME/SAE/ASEE Joint Propulsion Conference & Exhibit*. American Institute of Aeronautics and Astronautics, July 2005. DOI: 10.2514/6.2005-4535.

[24] Lars-Olof Winterfeldt et al. “Redesign of the Vulcain 2 Nozzle Extension”. In: *41st AIAA/ASME/SAE/ASEE Joint Propulsion Conference & Exhibit*. American Institute of Aeronautics and Astronautics, July 2005. DOI: 10.2514/6.2005-4536.

[25] G. Kirchhoff and L. Brummer. “Prüfstand für Thermoschock- und Temperaturwechselfestigkeit”. In: *Photonik* 37.5 (2005), p. 17.

[26] Andreas Gernoth et al. “TMF panel tests: close-to-reality simulation of thermo-mechanical fatigue processes in heat-loaded walls”. In: *44th AIAA/ASME/SAE/ASEE Joint Propulsion Conference & Exhibit*. July 2008. URL: https://elib.dlr.de/54538/.

[27] Andreas Gernoth et al. “TMF test based validation of numerical methods for the analysis of heat-loaded walls”. In: *46th AIAA/ASME/SAE/ASEE Joint Propulsion Conference & Exhibit*. July 2010. URL: https://elib.dlr.de/68028/.

[28] Andreas Gernoth, Jörg Riccius, and S. Schlechtriem. “Optical heating, thermography and deformation measurement of nozzle wall structures”. In: *49th AIAA Aerospace Sciences Meeting*. AIAA 2011-1264. 2011. URL: https://elib.dlr.de/72179/.

[29] Jörg Riccius et al. “A LASER plateau size optimization strategy for TMF tests”. In: *3rd EUropean Conference for AeroSpace Sciences*. July 2009. URL: https://elib.dlr.de/62424/.

[30] Dmitry Suslov et al. “Test Specimen Design and Measurement Technique for Investigation of Heat Transfer Processes in Cooling Channels of Rocket Engines under Real Thermal Conditions”. In: *39th AIAA/ASME/SAE/ Joint Propulsion Conference, Huntsville, AL, 20 - 23 July 2003*. Ed. by American Institute of Aeronautics and Astronautics. AIAA. LIDO-Berichtsjahr=2003, monograph_id=AIAA 2003-4613, AIAA, 2003. URL: https://elib.dlr.de/1632/.

[31] Jörg Riccius. "Cyclic Laser Heating and Optical Measurement of Combustion Chamber Wall Structures". In: *48th AIAA/ASME/SAE/ASEE Joint Propulsion Conference & Exhibit*. 2012. URL: https://elib.dlr.de/78225/.

[32] Jörg Riccius, W. Bouajila, and E. Zametaev. "Comparison of Finite Element analysis and experimental results of a combustion chamber type TMF panel test". In: *49th AIAA/ASME/SAE/ASEE Joint Propulsion Conference*. 2013. URL: https://elib.dlr.de/85325/.

[33] Ray Gordan Thiede et al. "Comparison of Damage Parameter Based Finite Element Fatigue Life Analysis Results to Combustion Chamber Type TMF Panel Test Results". In: *51st AIAA/SAE/ASEE Joint Propulsion Conference*. 2015. URL: https://elib.dlr.de/99733/.

[34] Ray Gordan Thiede, Jörg Riccius, and S. Reese. "Validation of Damage Parameter Based Finite Element Fatigue Life Analysis Results to Combustion Chamber Type TMF Panel Test Results". In: *52nd AIAA/SAE/ASEE Joint Propulsion Conference*. July 2016. URL: https://elib.dlr.de/107782/.

[35] Gordan Thiede, Jörg R. Riccius, and Stefanie Reese. "Life prediction of rocket combustion-chamber-type thermomechanical fatigue panels". In: *Journal of Propulsion and Power* (July 2017). URL: https://elib.dlr.de/114079/.

[36] Waldemar Schwarz. "Modelling of Viscoplasticity, Ageing and Damage for Life Prediction of Rocket Combustion Chambers". PhD thesis. Universität Erlangen-Nürnberg, 2013.

[37] Vivian Tini. "Lifetime prediction of a typical rocket combustion chamber by means of viscoplastic damage modeling". Zsfassung in dt. u. engl. Sprache; Zugl.: Aachen, Techn. Hochsch., Diss., 2014. PhD thesis. Aachen, 2014, II, 129 S. : Ill., graph. Darst. URL: https://publications.rwth-aachen.de/record/465634.

[38] Pascal H. Kringe et al. "Dependency of Surface Temperature on Coolant Mass Flow and Heat Flux in Rocket Combustion Chambers". In: *2022 IEEE Aerospace Conference (AERO)*. IEEE, Mar. 2022. DOI: 10.1109/aero53065.2022.9843694.

[39] Pascal H. Kringe et al. "Experimental and Numerical Fatigue Life Study of Inner Liner Material in Rocket Combustion Chambers". In: *2023 IEEE Aerospace Conference*. IEEE, Mar. 2023. DOI: 10.1109/aero55745.2023.10115623.

[40] Pascal H. Kringe et al. “Comparison of Experimental Fatigue Life Study for two Inner Liner Materials for Liquid Rocket Engines”. Eng. In: Proceedings of the Aerospace Europe Conference - EUCASS - CEAS - 2023, 2023. DOI: 10.13009/EUCASS2023-922.

[41] Felix Hötte et al. “Experimental lifetime study of regeneratively cooled rocket chamber walls”. In: *International Journal of Fatigue* 138 (Sept. 2020), p. 105649. DOI: 10.1016/j.ijfatigue.2020.105649.

[42] Felix Hötte et al. “Lifetime Experiments of Regeneratively Cooled Rocket Combustion Chambers and PIV Measurements in a High Aspect Ratio Cooling Duct”. In: *Future Space-Transport-System Components under High Thermal and Mechanical Loads*. Springer International Publishing, Oct. 2020, pp. 279–293. DOI: 10.1007/978-3-030-53847-7_18.

[43] Nikolaus A. Adams et al., eds. *Future Space-Transport-System Components under High Thermal and Mechanical Loads: Results from the DFG Collaborative Research Center TRR40*. Springer International Publishing, 2021. DOI: 10.1007/978-3-030-53847-7.

[44] M. Fassin et al. “Design studies of rocket engine cooling structures for fatigue experiments”. In: *Archive of Applied Mechanics* 86.12 (July 2016), pp. 2063–2093. DOI: 10.1007/s00419-016-1160-6.

[45] J.-L. Chaboche. “Cyclic Viscoplastic Constitutive Equations, Part I: A Thermodynamically Consistent Formulation”. In: *Journal of Applied Mechanics* 60.4 (Dec. 1993), pp. 813–821. DOI: 10.1115/1.2900988.

[46] ANSYS. *Mechanical APDL Material Reference*. Release 2022 R2. Canonsburg, PA 15317, July 2022.

[47] J.L. Chaboche. “Constitutive equations for cyclic plasticity and cyclic viscoplasticity”. In: *International Journal of Plasticity* 5.3 (Jan. 1989), pp. 247–302. DOI: 10.1016/0749-6419(89)90015-6.

[48] J.L. Chaboche. “On some modifications of kinematic hardening to improve the description of ratchetting effects”. In: *International Journal of Plasticity* 7.7 (Jan. 1991), pp. 661–678. DOI: 10.1016/0749-6419(91)90050-9.

[49] E Voce. In: *Metallurgica* 51 (1955), pp. 219–25.

[50] D. Peirce, C.F. Shih, and A. Needleman. “A tangent modulus method for rate dependent solids”. In: *Computers & Structures* 18.5 (Jan. 1984), pp. 875–887. DOI: 10.1016/0045-7949(84)90033-6.

[51] F.H. Norton. *The Creep of Steel at High Temperatures*. Bulletin. McGraw-Hill book Company, Incorporated, 1929.

[52] Jean Louis Chaboche. "Viscoplastic constitutive equations for the description of cyclic and anisotropic behaviour of metals". In: 1977.

[53] ANSYS. *Mechanical APDL Theory Reference*. Release 2022 R2. Canonsburg, PA 15317, July 2022.

[54] ANSYS. *Workbench Technology Showcase: Example Problems*. Release 2022 R2. Canonsburg, PA 15317, July 2022.

[55] C.O. Frederick and P.J. Armstrong. "A mathematical representation of the multiaxial Bauschinger effect". In: *Materials at High Temperatures* 24.1 (Apr. 2007), pp. 1–26. DOI: 10.3184/096034007x207589.

[56] Alice Petry et al. "Optimizing the Voce–Chaboche Model Parameters for Fatigue Life Estimation of Welded Joints in High-Strength Marine Structures". In: *Journal of Marine Science and Engineering* 10.6 (June 2022), p. 818. DOI: 10.3390/jmse10060818.

[57] ANSYS. *Programmer's Reference*. Release 2022 R2. Canonsburg, PA 15317, July 2022.

[58] T. Seifert, T. Schenk, and I. Schmidt. "Efficient and modular algorithms in modeling finite inelastic deformations: Objective integration, parameter identification and sub-stepping techniques". In: *Computer Methods in Applied Mechanics and Engineering* 196.17-20 (Mar. 2007), pp. 2269–2283. DOI: 10.1016/j.cma.2006.12.002.

[59] T. Seifert and I. Schmidt. "Line-search methods in general return mapping algorithms with application to porous plasticity". In: *International Journal for Numerical Methods in Engineering* 73.10 (2008), pp. 1468–1495. DOI: 10.1002/nme.2131.

[60] Thomas Seifert and Hermann Riedel. "Fatigue life prediction of high temperature components in combustion engines and exhaust systems". In: (2009).

[61] T. Seifert and I. Schmidt. "Plastic yielding in cyclically loaded porous materials". In: *International Journal of Plasticity* 25.12 (Dec. 2009), pp. 2435–2453. DOI: 10.1016/j.ijplas.2009.04.003.

[62] T. Seifert et al. "Mechanism-based thermomechanical fatigue life prediction of cast iron. Part II: Comparison of model predictions with experiments". In: *International Journal of Fatigue* 32.8 (Aug. 2010), pp. 1368–1377. DOI: 10.1016/j.ijfatigue.2010.02.005.

[63] Thomas Seifert, Radwan Hazime, and Steven Dropps. “TMF Life Prediction of High Temperature Components Made of Cast Iron HiSiMo: Part II: Multiaxial Implementation and Component Assessment”. In: *SAE International Journal of Materials and Manufacturing* 7.2 (Apr. 2014), pp. 421–431. DOI: 10.4271/2014-01-0905.

[64] J.L. Chaboche. “Time-independent constitutive theories for cyclic plasticity”. In: *International Journal of Plasticity* 2.2 (Jan. 1986), pp. 149–188. DOI: 10.1016/0749-6419(86)90010-0.

[65] Tadashi Masuoka and Jörg R Riccius. “Life evaluation of a combustion chamber by thermomechanical fatigue panel tests based on a creep fatigue and ductile damage model”. In: *International Journal of Damage Mechanics* 29.2 (Mar. 2019), pp. 226–245. DOI: 10.1177/1056789519835881.

[66] Jean Lemaitre. “How to use damage mechanics”. In: *Nuclear Engineering and Design* 80.2 (July 1984), pp. 233–245. DOI: 10.1016/0029-5493(84)90169-9.

[67] Jean Lemaitre. *A Course on Damage Mechanics*. Springer Berlin Heidelberg, 1996. DOI: 10.1007/978-3-642-18255-6.

[68] Dietmar Gross and Thomas Seelig. *Bruchmechanik*. Springer Berlin Heidelberg, 2011. DOI: 10.1007/978-3-642-10196-0.

[69] Jean Lemaitre and Rodrigue Desmorat. *Engineering Damage Mechanics*. Springer-Verlag, 2005. DOI: 10.1007/b138882.

[70] LM Kachanov. “Time of rupture process under deep conditions”. In: *Izv. Akad. Nauk SSSR* 8 (1958), p. 26.

[71] Yu. N. Rabotnov, F. A. Leckie, and W. Prager. “Creep Problems in Structural Members”. In: *Journal of Applied Mechanics* 37.1 (Mar. 1970), pp. 249–249. DOI: 10.1115/1.3408479.

[72] J. L. Chaboche. “Continuum Damage Mechanics: Part I—General Concepts”. In: *Journal of Applied Mechanics* 55.1 (Mar. 1988), pp. 59–64. DOI: 10.1115/1.3173661.

[73] Jörg Riccius, Oskar Haidn, and Evgeny Zametaev. “Structural Analysis of the Cyclic Loading of Regeneratively Cooled Combustion chamber Walls Using 2D and 3D Finite Element Models”. In: *DGLR*. Ed. by DGLR. Nov. 2006. URL: https://elib.dlr.de/49569/.

[74] Jörg Riccius. “Results of a Liquid Rocket Booster (LRB) Nozzle Throat Related Thermo-Mechanical Fatigue (TMF) Panel Test”. In: *32nd International Symposium on Space Technology and Science*. 2019. URL: https://elib.dlr.de/133369/.

[75] Nicola Bonora. “A nonlinear CDM model for ductile failure”. In: *Engineering Fracture Mechanics* 58.1-2 (Sept. 1997), pp. 11–28. DOI: 10.1016/s0013-7944(97)00074-x.

[76] Marcus Lehmann. “Implementation of a mesh-size-independent viscoplasticity damage model through a nonlocal continuum mechanical approach”. Veröffentlicht auf dem Publikationsserver der RWTH Aachen University; Dissertation, Rheinisch-Westfälische Technische Hochschule Aachen, 2021. Dissertation. Aachen: Rheinisch-Westfälische Technische Hochschule Aachen, 2021, 1 Online–Ressource : Illustrationen, Diagramme. DOI: 10.18154/RWTH-2021-07951. URL: https://publications.rwth-aachen.de/record/824943.

[77] R. D. Thomson and J. W. Hancock. “Ductile failure by void nucleation, growth and coalescence”. In: *International Journal of Fracture* 26.2 (Oct. 1984), pp. 99–112. DOI: 10.1007/bf01157547.

[78] Nicola Bonora et al. “Ductile damage evolution under triaxial state of stress: theory and experiments”. In: *International Journal of Plasticity* 21.5 (May 2005), pp. 981–1007. DOI: 10.1016/j.ijplas.2004.06.003.

[79] Nicola Bonora. “On the Effect of Triaxial State of Stress on Ductility Using Nonlinear CDM Model”. In: *International Journal of Fracture* 88.4 (1997), pp. 359–371. DOI: 10.1023/a:1007479522972.

[80] Frank P. Incropera. *Fundamentals of Heat and Mass Transfer*. Hoboken, NJ, USA: John Wiley & Sons, Inc., 2007.

[81] Heinz Herwig. *Wärmeübertragung A-Z*. Springer Berlin Heidelberg, 2000. DOI: 10.1007/978-3-642-56940-1.

[82] *VDI Heat Atlas*. Springer Berlin Heidelberg, 2010. DOI: 10.1007/978-3-540-77877-6.

[83] Octave Levenspiel. *Engineering Flow and Heat Exchange*. Springer US, 2014. DOI: 10.1007/978-1-4899-7454-9.

[84] Jan Haemisch. “Heat Transfer Processes for Hydrogen and Methane in Cooling Channels of Regeneratively Cooled Thrust Chambers of Cryogenic Rocket Engines”. PhD thesis. RWTH Aachen University, Jan. 2020. URL: https://elib.dlr.de/137918/.

[85] Nikolaos Perakis. “Wall Heat Transfer Measurement and Prediction in Methane/Oxygen Rocket Engines”. en. PhD thesis. Technische Universität München, 2021, p. 277.

[86] Yohann Torres. “Transferts énergétiques dans les canaux de refroidissement courbes de moteurs fusées”. Thèse de doctorat dirigée par Desmet, Bernard Mécanique. Énergétique Valenciennes 2008. PhD thesis. Dissertation L’Universite de Valenciennes et du Hainaut Cambresis, 2008, 1 vol. (190 p.) URL: http://www.theses.fr/2008VALE0021.

[87] Frank Kreith, Raj M. Manglik, and Mark S. Bohn. *Principles of Heat Transfer, SI Edition*. CENGAGE Learning, 2010, p. 696.

[88] Joel H. Ferziger, Milovan Peric, and Robert L. Street. *Numerische Strömungsmechanik*. Springer Berlin Heidelberg, 2020. DOI: 10.1007/978-3-662-46544-8.

[89] ANSYS. *ANSYS CFX-Solver Theory Guide*. Release 2022 R2. Canonsburg, PA 15317, July 2022.

[90] H. Schlichting et al. *Grenzschicht-Theorie*. Springer, 2006. URL: https://books.google.de/books?id=MOt-kTuzLxoC.

[91] Bruce R. Munson et al. *Fundamentals of Fluid Mechanics*. Wiley & Sons, Incorporated, John, 2012.

[92] Clemens Schaefer. “26. Die van der Waalssche Zustandsgleichung für reale Gase - Anwendung des ersten Hauptsatzes auf ein reales Gas”. In: *Theorie der Wärme, Molekular-kinetische Theorie der Materie*. De Gruyter, Dec. 1921, pp. 108–117. DOI: 10.1515/9783112364765-027.

[93] O. C. Jones. “An Improvement in the Calculation of Turbulent Friction in Rectangular Ducts”. In: *Journal of Fluids Engineering* 98.2 (June 1976), pp. 173–180. DOI: 10.1115/1.3448250.

[94] Detlef Kuhl, Jörg Riccius, and Oskar J. Haidn. “Thermomechanical Analysis and Optimization of Cryogenic Liquid Rocket Engines”. In: *Journal of Propulsion and Power* 18.4 (July 2002), pp. 835–846. DOI: 10.2514/2.6007.

[95] Frank White. *Fluid mechanics*. New Delhi, India: McGraw-Hill Education, 2017.

[96] Herbert Wittel et al. *Roloff/Matek Maschinenelemente*. 20. Edition. Vieweg+Teubner Verlag, 2011. DOI: 10.1007/978-3-8348-8279-0.

[97] Wolfgang S. M. Werner, Kathrin Glantschnig, and Claudia Ambrosch-Draxl. "Optical Constants and Inelastic Electron-Scattering Data for 17 Elemental Metals". In: *Journal of Physical and Chemical Reference Data* 38.4 (Dec. 2009), pp. 1013–1092. DOI: 10.1063/1.3243762.

[98] Shaista Babar and J. H. Weaver. "Optical constants of Cu, Ag, and Au revisited". In: *Applied Optics* 54.3 (Jan. 2015), p. 477. DOI: 10.1364/ao.54.000477.

[99] Biliyar N. Bhat, Sandra Greene, and Jogender Singh. "Fabrication of High Thermal Conductivity NARloy-Z-Diamond Composite Combustion Chamber Liner for Advanced Rocket Engines". In: *57th AIAA/ASCE/AHS/ASC Structures, Structural Dynamics, and Materials Conference*. American Institute of Aeronautics and Astronautics, Jan. 2016. DOI: 10.2514/6.2016-1416.

[100] Kai Bubenheim. *Experimentelle Untersuchungen zur Hochtemperaturdegradation von Kupfer-Silber-Zirkonium Legierung unter Raketenbrennkammerbedingungen*. Berichte aus der Luft- und Raumfahrttechnik. Aachen: Shaker Verlag, 2016.

[101] Toshiya KIMURA, Shin-Ichi MORIYA, and Masaharu TAKAHASHI. "Effects of Cu-alloy Material Properties on Lifetime of a Combustion Chamber with or without a Thermal Barrier Coating". In: (2017). DOI: 10.13009/EUCASS2017-535.

[102] M. Popp and G. Schmidt. "Rocket engine combustion chamber design concepts for enhanced life". In: *32nd Joint Propulsion Conference and Exhibit*. American Institute of Aeronautics and Astronautics, July 1996. DOI: 10.2514/6.1996-3303.

[103] Jan C. Deeken. *Experimentelle Untersuchungen zu neuartigen, porösen Injektoren für den Einsatz in kryogenen Hochdruck-Raketenantrieben*. Tech. rep. Universität Stuttgart, 2014. URL: https://elib.dlr.de/93971/.

[104] Marcel Pouliquen and Georges S. Gill. "Performance Characteristics of the HM7 Rocket Engine for the Ariane Launcher". In: *Journal of Spacecraft and Rockets* 16.6 (Nov. 1979), pp. 367–372. DOI: 10.2514/3.57676.

[105] *Cu-HCP – CW021A*. 2005. URL: https://www.kupferinstitut.de/wp-content/uploads/2019/11/Cu-HCP.pdf.

[106] M. P. Celano et al. "Injector characterization for a gaseous oxygen-methane single element combustion chamber". In: *Progress in Propulsion Physics*. Ed. by M. Calabro et al. EDP Sciences, 2016. DOI: 10.1051/eucass/201608145.

[107] *DIN CEN/TS 13388:2020-09, Kupfer und Kupferlegierungen - Übersicht über Zusammensetzungen und Produkte Deutsche Fassung*. 2020. DOI: 10.31030/3057412.

[108] *DIN EN ISO 6506-1:2015-02, Metallische Werkstoffe_ - Härteprüfung nach Brinell_ - Teil_ 1: Prüfverfahren (ISO_ 6506-1:2014) Deutsche Fassung EN ISO 6506-1:2014*. DOI: 10.31030/2146324.

[109] *KME Germany GmbH & Co. KG Data Sheet: ELBRODUR-Alloy*. Tech. rep. Doc.-No.0315.000.0100., 2015.

[110] David Ellis, Dennis Keller, and Michael Nathal. "Thermophysical Properties of GRCop-84". In: (July 2000).

[111] Bernd Köhler et al. "11-kW direct diode laser system with homogenized 55 × 20 mm² Top-Hat intensity distribution". In: *Proc. SPIE 6456, High-Power Diode Laser Technology and Applications V, 64560O*. 7. 2007. DOI: 10.1117/12.698837.

[112] KRYTEM GmbH. *Data Sheet Reciprocating Pump - C 09 020*. Willich, Germany, Jan. 2004.

[113] *FLIR SC7000 Series*. 10/14. FLIR Systems Inc., Oct. 2014.

[114] *Q400 DIC Digital Image Correlation*. LIMESS Messtechnik u. Software GmbH, Germany, 2019. URL: https://www.limess.com/en/component/jdownloads/send/12-q400/10-q400-leaflet-english.

[115] *Allied Vision Prosilica GE - Technical Manual GigE Vision Cameras*. V2.3.3. Allied Vision Technologies GmbH, Germany, Sept. 2018.

[116] *ISTRA 4D Software Manual Q-400 System*. Version 2.6.2. Dantec Dynamics GmbH, Germany, 2020.

[117] Electronic Sensor GmbH. *Druckthermoelemente Typ K für Swagelok-Verschraubungen, Klasse 1 gem. IEC 584-3*. Heilbronn, Germany, 2013. URL: https://electronic-sensor.de/attachments/article/20/2-5_druckthermoelemente-swagelok.pdf.

[118] OMEGA Engineering GmbH. *TJC1 Miniatur-Thermoelementfühler mit kompakter Metall-Übergangsstelle*. Deckenpfronn, Germany, 2015. URL: https://www.omega.de/temperature/pdf/TJC100.pdf.

[119] Isothermal Technology Limited. *Thermocouple Reference Unit TRUrac Model 847*. Merseyside, England. URL: https://isotech.co.uk/wp-content/uploads/2020/09/TRUrac-Model-847.pdf.

[120] Sensing, Control Automation, and Control Solutions Honeywell. *Model KZ - Low Range Wet/Wet DifferentialPressure Transducer*. MN, USA, May 2008. URL: https://sensing.honeywell.com/honeywell-test-and-measurement-model-kz-low-diff-pressure-transducer-datasheet-008766-1-en.pdf.

[121] Sensing, Control Automation, and Control Solutions Honeywell. *Model HL-Z - High Line Wet/Wet Differential Pressure Transducer*. MN, USA, Dec. 2011. URL: https://sensing.honeywell.com/honeywell-test-and-measurement-model-hl-z-diff-pressure-transducer-datasheet-008715-2-en.pdf.

[122] Emerson Electric Co. Micro Motion. *Product Data Sheet - Micro Motion™ ELITE™ Coriolis Flow and Density Meters*. PS-00374, Rev. AK. Boulder, Colorado, USA, Jan. 2020.

[123] *DAQP-STG - Isolated universal input module*. URL: https://www.dewetron.com/product/daqp-stg/.

[124] H. Horn. *Messverstärkereinschub AS4*. Deutsches Zentrum für Luft- und Raumfahrt e.V, Nov. 2008.

[125] National Instruments Corporation. *NI 6030E/6031E/6032E/6033E Family Specifications*. 370720C-01. Dec. 2005.

[126] National Instruments. *NI 6221 Device Specifications*. 375303C-01. June 2016.

[127] G. G. Simeoni et al. "The Widom line as the crossover between liquid-like and gas-like behaviour in supercritical fluids". In: *Nature Physics* 6.7 (June 2010), pp. 503–507. DOI: 10.1038/nphys1683.

[128] D.T. Banuti. "Crossing the Widom-line – Supercritical pseudo-boiling". In: *The Journal of Supercritical Fluids* 98 (Mar. 2015), pp. 12–16. DOI: 10.1016/j.supflu.2014.12.019.

[129] A. de Castro e Sousa, A. R. Hartloper, and D. G. Lignos. *RESSPyLab 1.1.6.* 2019. URL: Available%20online:%20https://pypi.org/project/RESSPyLab/.

[130] Albano de Castro e Sousa, Yusuke Suzuki, and Dimitrios Lignos. "Consistency in Solving the Inverse Problem of the Voce-Chaboche Constitutive Model for Plastic Straining". In: *Journal of Engineering Mechanics* 146.9 (Sept. 2020). DOI: 10.1061/(asce)em.1943-7889.0001839.

[131] Martin Antonio René Garcia. "Multiaxial fatigue analysis of high-strength steel welded joints using generalized local approaches". en. PhD thesis. 2020. DOI: 10.5075/EPFL-THESIS-7394.

[132] Jean Lemaitre and Jean-Louis Chaboche. *Mechanics of Solid Materials*. Cambridge University Press, Feb. 1990. DOI: 10.1017/cbo9781139167970.

[133] Sheldon Imaoka. "Chaboche Nonlinear Kinematic Hardening Model". In: *Memo Number: STI0805A*. 2008. URL: https://api.semanticscholar.org/CorpusID:54634385.

[134] A.K. Asraff et al. *Conference proceedings : Cyclic stress analysis of a rocket engine thrust chamber using Chaboche constitutive model*. en. 2015. DOI: 10.13140/RG.2.1.1936.0080.

[135] Jelena Srnec Novak. "Parameter estimation of cyclic plasticity models and strain-based fatigue curves in numerical analysis of mechanical components under thermal loads". PhD thesis. Apr. 2016. URL: http://hdl.handle.net/11390/1132791.

[136] Piotr Perzyna. "Fundamental Problems in Viscoplasticity". In: *Advances in Applied Mechanics* 9 (1966), pp. 243–377. URL: https://api.semanticscholar.org/CorpusID:115702246.

[137] Nicola Bonora, Domenico Gentile, and Alessandro Pirondi. "Identification of the parameters of a non-linear continuum damage mechanics model for ductile failure in metals". In: *The Journal of Strain Analysis for Engineering Design* 39.6 (Aug. 2004), pp. 639–651. DOI: 10.1243/0309324042379356.

[138] Michael Oschwald, Dmitry Suslov, and Alexander Woschnak. "Temperature Dependence of Material Properties and its Influence on the Thermal Distribution in Regenratively Cooled Combustion Chamber Walls". In: *1st EUCASS*. 2005. URL: https://elib.dlr.de/53352/.

[139] Victor J. Johnson. *A Compendium Of The Properties Of Materials At Low Temperature (PHASE 1) Part 2. Properties Of Solids*. Tech. rep. Oct. 1960. DOI: 10.21236/ad0249786.

[140] N J Simon, E S Drexler, and R P Reed. *Properties of copper and copper alloys at cryogenic temperatures*. Tech. rep. 1992. DOI: 10.6028/nist.mono.177.

[141] J G Hust and A B Lankford. *Thermal conductivity of aluminum, copper, iron, and tungsten for temperatures from 1 K to the melting point*. Tech. rep. 1984. DOI: 10.6028/nbs.ir.84-3007.

[142] Charles Kittel. *Introduction to solid state physics*. New York: Wiley, 1996.

[143] Neil Ashcroft. *Solid state physics*. New York: Holt, Rinehart and Winston, 1976.

[144] NETZSCH-Gerätebau GmbH. *Differential Scanning Calorimetry – DSC 404 F1/F3 Pegasus*.

[145] *DIN 51007:2019-04, Thermische Analyse_ (TA)_ - Differenz-Thermoanalyse_ (DTA)_ und Dynamische Differenzkalorimetrie_ (DSC)_ - Allgemeine Grundlagen*. DOI: 10.31030/3025544.

[146] Jr. Malcolm W. Chase. *Nist-Janaf Thermochemical Tables Set*. SPRINGER NATURE, Aug. 1998. 1952 pp. URL: https://www.ebook.de/de/product/8137419/jr_malcolm_w_chase_nist_janaf_thermochemical_tables_set.html.

[147] NETZSCH-Gerätebau GmbH. *TMA 402 F1/F3 Hyperion*.

[148] *DIN 51045-1:2005-08, Bestimmung der thermischen Längenänderung fester Körper_ - Teil_ 1: Grundlagen*. DOI: 10.31030/9636919.

[149] NETZSCH-Gerätebau GmbH. *Laser Flash Apparatus LFA 427*.

[150] *Test Method for Thermal Diffusivity by the Flash Method*. DOI: 10.1520/e1461-13.

[151] Pascal H. Kringe et al. "Dependency of Inner Liner Surface Temperature on Coolant Mass Flow Rate and Heat Flux in Rocket Combustion Chambers". In: *Space Propulsion 2020 + 1*. 2021. URL: https://elib.dlr.de/146265/.

[152] David C. Wilcox. "Multiscale model for turbulent flows". In: *AIAA Journal* 26.11 (Nov. 1988), pp. 1311–1320. DOI: 10.2514/3.10042.

[153] F. R. Menter. "Two-equation eddy-viscosity turbulence models for engineering applications". In: *AIAA Journal* 32.8 (Aug. 1994), pp. 1598–1605. DOI: 10.2514/3.12149.

[154] Thomas Adams, Christopher Grant, and Heather Watson. "A Simple Algorithm to Relate Measured Surface Roughness to Equivalent Sandgrain Roughness". In: *International Journal of Mechanical Engineering and Mechatronics* (2012). DOI: 10.11159/ijmem.2012.008.

[155] I. Mudawar. "Assessment of high-heat-flux thermal management schemes". In: *IEEE Transactions on Components and Packaging Technologies* 24.2 (June 2001), pp. 122–141. DOI: 10.1109/6144.926375.

[156] ANSYS. *Mechanical APDL Element Reference*. Release 2022 R2. Canonsburg, PA 15317, July 2022.

[157] ANSYS. *ANSYS Meshing Users Guide*. Release 2022 R2. Canonsburg, PA 15317, July 2022.

[158] ANSYS. *Mechanical Users Guide*. Release 2022 R2. Canonsburg, PA 15317, July 2022.

[159] Mateusz T. Gulczynski et al. "Numerical FatigueLife Analysis of Combustion Chamber Walls for FutureReusable Liquid Rocket Engines (LREs) Applications". In: ed. by Mateusz T. Gulczynski et al. Vol. SP2022. 143. 3AF – Association Aéronautique et Astronautique de France, Mai 2022. URL: https://elib.dlr.de/186612/.

[160] Pawel Ziolkowski and Eckhard Müller. "High throughput scanning metrology for thermoelectric transport properties–A prerequisite for combinatorial materials research". In: *DLR Materials Colloquium 2019*. kein referierter Beitrag. 2020. URL: https://elib.dlr.de/137249/.

[161] Jeffrey L. Braun et al. "A steady-state thermoreflectance method to measure thermal conductivity". In: *Review of Scientific Instruments* 90.2 (Feb. 2019). DOI: 10.1063/1.5056182.

[162] Md Shafkat Bin Hoque et al. "Thermal conductivity measurements of sub-surface buried substrates by steady-state thermoreflectance". In: *Review of Scientific Instruments* 92.6 (June 2021). DOI: 10.1063/5.0049531.

[163] Kiumars Aryana et al. "Observation of solid-state bidirectional thermal conductivity switching in antiferroelectric lead zirconate (PbZrO3)". In: *Nature Communications* 13.1 (Mar. 2022). DOI: 10.1038/s41467-022-29023-y.